A Stable Static Universe?¶

C. Barceló[1] and G. E. Volovik[2, 3]

[1] Instituto de Astrofisica de Andalucía, 18008 Granada, Spain
[2] Low Temperature Laboratory, Helsinki University of Technology, Box 2200, FIN-02015 HUT, Finland
[3] Landau Institute for Theoretical Physics, Moscow, 117334 Russia
e-mail: carlos@iaa.es, volovik@boojum.hut.fi
Received May 20, 2004; in final form, July 15, 2004

Starting from the assumption that general relativity might be an emergent phenomenon showing up at low energies from an underlying microscopic structure, we reanalyze the stability of a static closed universe filled with radiation. In this scenario, it is sensible to consider the effective general-relativistic configuration as in a thermal contact with an "environment" (the role of the environment can be played, for example, by a higher-dimensional bulk or by the trans-Planckian degrees of freedom). We calculate the free energy at a fixed temperature of this radiation-filled static configuration. Then, by looking at the free energy, we show that the static Einstein configuration is stable under the stated condition. © 2004 MAIK "Nauka/Interperiodica".

PACS numbers: 04.20.EX; 04.40.Nr; 04.50.+h

1. INTRODUCTION

The development of a geometrical description of the gravitational field led Einstein in 1917 to propose that the universe could be, overall, a three-dimensional sphere with no other evolution than that provided by local physics [1]. To make this sort of equilibrium state for the universe compatible with his geometrical field equations, he introduced the to-be-famous cosmological constant. The cosmological constant succeeds in counterbalancing the collapsing tendency of all matter in the universe. Later, in 1930, Eddington proved that Einstein's static universe was unstable under homogeneous departures from the equilibrium state [2]. At that time, Hubble had already observed the recession of galaxies. For this reason and in view of the instability, the Einstein model was considered as a possible initial state for the universe that, once destabilized, would start to expand. (This point of view has been revisited recently in [3, 4].)

Eddington did not clearly analyze what could trigger the development of the instability, but vaguely associated it with the formation of condensations. Thanks to a very interesting series of works [3–8] (we do not intend to be exhaustive), at present we know that the instability of models of the universe that are overall closed, homogeneous, isotropic, and static is a much more subtle issue. From here on, we will call all these models Einstein models, independently of their matter content, although the model proposed by Einstein himself corresponds to a universe filled with dust.

On the one hand, Harrison showed [7] that, if the equation of the state of matter is such that its associated

speed of sound c_s is greater than $1/\sqrt{5}$, all the physical inhomogeneous perturbations are neutrally stable. This has been recently emphasized and extended by Ellis and Maartens [3] and Barrow *et al.* [4]. This case includes a radiation-dominated universe. For $0 \neq c_s < 1/\sqrt{5}$, only a finite set of inhomogeneous modes becomes unstable. What happens is that, in a finite-size universe, as an Einstein model, the Jeans scale for the formation of condensations is a significant fraction of the maximum attainable scale. Therefore, for sufficiently high speeds of sound, only the universe as a whole can develop instability. For this same condition, $c_s > 1/\sqrt{5}$, Gibbons also showed that the Einstein point corresponds to a local maximum of entropy among the set of geometries conformally related to it that have a moment of time symmetry [8].

On the other hand, Bonnor showed [6] that, at least in the simplest case in which matter satisfies an equation of state, in order to really depart from the Einstein state, one would need a global decrease in pressure in the entire universe (this process had already been discussed by Lemaître in 1931 under the name of *stagnation* [5]). This suggests that a static universe describable in the cosmological scales as filled with dust for which $p = 0$ would not be able to change its static global state, but only develop instabilities on smaller scales. On the other extreme, a static universe filled with radiation could, in principle, exit from this state toward a Friedman expansion by decreasing its pressure. Here, we will concentrate on this later model and its instability.

In this paper, we will analyze the stability of a closed and static universe filled with radiation, but starting from notions somewhat different from those in stan-

---

¶ This article was submitted by the authors in English.

dard general relativity. General relativity is commonly considered to be a low-energy effective theory that emerges from a deeper underlying structure. A particular realization of this situation is suggested by gravitational features that show up in many condensed matter systems (such as liquid helium) in the low-energy corner [9]. These types of systems suggest that both matter particles and interaction fields could be different emergent features of the underlying system: they will correspond to quasiparticles and collective-field excitations of a multiparticle quantum system. For example, in the phase A of ^{3}He, the quasiparticles correspond to Weyl fermions and the collective fields to electromagnetic and gravitational (geometrical) fields.

Imagine now that a universe of the Einstein type was the effective result of describing the geometric and matterlike degrees of freedom emerging from the underlying structure. A photon-filled Einstein universe will have a specific temperature. In the standard general relativity, the stability of the system is analyzed under the assumption of adiabaticity: there is no heat transfer into or out of the universe because "there is nothing outside the universe." However, in the emergent picture described above, there is not any *a priori* reason to consider the system as effectively thermodynamically closed (let us remark that this is a nonstandard general relativistic behavior). Therefore, it is natural to ask what would happen with perturbance of the Einstein state if the temperature of the underlying structure stayed constant. We will not enter into what sets and controls this temperature, but let us only assume that it is independent from the behavior of the effective universe. Let us emphasize that we do not disturb general relativity, so that the solution for the equilibrium static universe is the same that follows from the Einstein equations. We only allow for heat exchange with the "environment."

Apart from the emergent gravity picture, there exist other situations in which the image of an externally fixed temperature might also make sense. These are situations in which the four-dimensional world of standard general relativity does not conform to a completely closed system. We can imagine, for example, scenarios with extra dimensions (playing the role of the environment), from which energy could flow into and out of the four-dimensional section.

In the following, we will compare Eddington's stability analysis with an analysis based on the fact that the temperature of the system is kept fixed. For that, we will calculate the free energy of radiation-dominated Einstein states. Let us now start by reviewing the standard Eddington instability argument.

2. EDDINGTON'S INSTABILITY ANALYSIS

Consider a generic positive-curvature FRW metric written in the form

$$ds^2 = -N^2(t)dt^2 + a^2(t)\Omega_{ij}dx^i dx^j. \tag{1}$$

Here, $N(t)$ is the lapse function, $a(t)$ is the scale factor, and Ω_{ij} is the metric on a unit-three sphere. Following Schutz [10], the Einstein equations for a universe filled with a perfect fluid can be obtained by varying the action

$$S = \frac{1}{16\pi G}\int d^4x\sqrt{-g}(R - 2\Lambda)$$
$$+ \int d^3x\sqrt{-g}K + \int d^4x\sqrt{-g}\,p. \tag{2}$$

This is the standard Einstein–Hilbert action supplemented with a boundary term and the volume integral of the fluid pressure p. To obtain the standard form of the Friedman and Raychaudhuri equations, we can substitute the previous FRW ansatz in the action and, after variation, set the lapse function equal to unity, $N = 1$. Specifically, the action can be written as

$$S = \frac{2\pi^2}{8\pi G}\int dt Na^3\left[3\left(-\frac{\dot{a}^2}{a^2}\frac{1}{N_a} + \frac{1}{a^2}\right) - \Lambda\right]$$
$$+ 2\pi^2\int dt Na^3 p(N). \tag{3}$$

Here, the explicit dependence of the pressure on its argument is determined by the condition

$$N\frac{\partial p(N)}{\partial N} = -(\rho + p). \tag{4}$$

For example, for a radiation equation of state $\rho = 3p$, one obtains from this condition that $p = CN^{-4}$, with C being a constant.

By looking at the previous action and having in mind that we are interested in the analysis of the static solutions of the system, we can define a different and simpler functional containing all the relevant information:

$$S_{st} = \int dt Na^3\left[\frac{3}{a^2} - \Lambda + \tilde{p}(N)\right]. \tag{5}$$

Here, we have rescaled the density and pressure as $\tilde{\rho} = 8\pi G\rho$, $\tilde{p} = 8\pi Gp$. We can easily see that, by varying with respect to N and a and setting $N = 1$, we obtain

$$(\Lambda + \tilde{\rho})a^2 = 3, \tag{6}$$

$$(\Lambda - \tilde{p})a^2 = 1. \tag{7}$$

In the case of a universe filled with radiation, $\tilde{\rho} = 3\tilde{p}$, these relations give us the radiation Einstein conditions $\tilde{\rho} = \Lambda$, $a_0^2 = (3/2)\Lambda^{-1}$.

By looking at the functional S_{st} (setting $N = 1$), one can also see that the Einstein point is not stable. Taking into account that the kinetic term for the scale factor enters gravitational action (3) with a negative sign, the local maxima of the functional S_{st} will correspond to unstable points. This is precisely the case for the Ein-

stein point (one can perform explicitly the second variation with respect to a to check this local behavior). This is the Eddington instability we described in the Introduction. We have obtained it here in this variational way because of later convenience in comparing it with the result obtained from the free energy function.

3. FREE ENERGY OF A STATIC GRAVITATIONAL CONFIGURATION

Let us now take a completely different point of view. Let us analyze what happens when the perturbation of the Einstein model is performed as immersed in a thermal reservoir at a fixed temperature. For that, let us consider the free energy of static gravitational configurations. We follow the treatment described in [11] and references therein. The free energy of the purely gravitational part of a static configuration is determined by the Euclidean action of the configuration (see, for example, [12]),

$$F_0 = T_0 I = -\frac{T_0}{16\pi G}\int d\tau d^3x \sqrt{g_e}(R_e - 2\Lambda). \quad (8)$$

Here, the temporal coordinate τ is periodic, with a period equal to the inverse of the temperature T_0. The symbols R_e and g_e stand, respectively, for the Euclidean curvature and Euclidean metric of the configuration. We can realize that these terms, coming from the purely gravitational sector, do not actually depend on the temperature, so they will be there even at a temperature of zero,

$$F_0 = -\frac{1}{16\pi G}\int d^3x \sqrt{g_e}(R_e - 2\Lambda). \quad (9)$$

We are assuming that a proper Einstein–Hilbert behavior is emerging in the low-energy corner. Let us remind you that this is not what normally happens in the standard condensed matter systems we know of. In these cases, the Einstein–Hilbert behavior is supplemented with noncovariant terms (see [9]).

Let us now consider the free energy of a gas of photons (radiation) inside a curved but static geometry. The leading term in the temperature on the free energy function is

$$F_1 = -\frac{\sigma}{3}\int d^3x \sqrt{g_e} T^4(x), \quad (10)$$

where $\sigma \equiv \pi^2 k_B^4/15\hbar^3 c^2$ is the Stefan–Boltzmann constant and

$$T(x) = \frac{T_0}{\sqrt{g_{00}(x)}} \quad (11)$$

is the Tolman temperature (we will see later that there are other contributions to the free energy in lower powers of the temperature). For the particular geometries we are interested in here, the total free energy can be written as

$$F(a, N, T) = F_0 + F_1 = \frac{2\pi^2 a^3}{8\pi G}\left[-\frac{3N}{a^2} + N\Lambda - \frac{\tilde{p}}{N^3}\right], (12)$$

with

$$\tilde{p} = \frac{1}{3}\tilde{\rho} = \frac{8\pi G}{3}\sigma T_0^4 : \text{const.} \quad (13)$$

From this free energy, which is associated with a static geometry filled with radiation at a temperature T_0, we can obtain the Einstein static condition. It corresponds to the one that extremizes the function F. Variation with respect to N with a later evaluation in $N = 1$ gives

$$(\Lambda + 3\tilde{p})a^2 = (\Lambda + \tilde{\rho})a^2 = 3. \quad (14)$$

Variation with respect to a yields

$$(\Lambda - \tilde{p})a^2 = 1. \quad (15)$$

Therefore, we have found the same expressions as before: the conditions for a static Einstein universe filled with radiation.

By inspection of the free energy function, we can see that the Einstein static point is now located at a local minimum. This is the main point we want to highlight in this paper. *If the perturbation of the radiation-filled Einstein universe is done under the influence of an externally fixed temperature (something outside the realm of standard general relativity), then the Einstein point will be stable.*

4. CORRECTIONS DUE TO THE TEMPERATURE

In the previous section, we analyzed the free energy of a system composed by static geometries of the Einstein type as the containers, plus photon gases as the contents. Free energy (12) is an approximation, as it does not contain additional contributions in smaller powers of the temperature. In the high-temperature limit $T^2 \gg \hbar^2 R_e$, the total free energy for a gas of photons in a static spacetime is [11, 13]

$$F = -\frac{1}{16\pi G}\int d^3x \sqrt{g_e}(R_e - 2\Lambda)$$
$$-\frac{\sigma}{3}\int d^3x \sqrt{g_e} T^4 + \bar{\sigma}\int d^3x \sqrt{g_e} T^2[R_e + 6\omega^2] \quad (16)$$

with

$$\omega_\mu = \frac{1}{2}\partial_\mu \ln|g_{00}(r)|. \quad (17)$$

Here, the prefactor $\bar{\sigma}$ in the T^2R_e term is $\bar{\sigma} = N_v/36\hbar$ and is obtained by integration over thermal photon fields (see [14]). If the integration had been made using minimally coupled scalar fields, the coefficient would have been $\bar{\sigma} = -N_s/144\hbar$, with N_s the number of minimally coupled scalar fields; equivalently, for N_d Dirac

fermions, one would have $\bar{\sigma} = N_d/144\hbar$ [11, 13]. In our particular case, this free energy yields

$$F(N, a, T_0)$$

$$= \frac{2\pi^2 a^3}{8\pi G}\left[-\frac{3N}{a^2} + N\Lambda - \frac{\tilde{p}}{N^3} + 8\pi G\bar{\sigma}\frac{6T_0^2}{Na^2}\right], \quad (18)$$

or, expressing everything in terms of $\tilde{\rho}$ and denoting the constant factor $(8\pi G/\sigma)^{1/2}6\bar{\sigma}$ by the letter b,

$$F(N, a, T_0)$$

$$= \frac{2\pi^2 a^3}{8\pi G}\left[-\frac{3N}{a^2} + N\Lambda - \frac{\tilde{\rho}}{3N^3} + b\frac{\tilde{\rho}^{1/2}}{Na^2}\right]. \quad (19)$$

Varying with respect to N and a, we now find

$$(\Lambda + \tilde{\rho})a^2 - b\tilde{\rho}^{1/2} = 3, \quad (20)$$

$$\left(\Lambda - \frac{1}{3}\tilde{\rho}\right)a^2 + \frac{1}{3}b\tilde{\rho}^{1/2} = 1. \quad (21)$$

Manipulating these two conditions, one obtains

$$\Lambda = \frac{3}{2a^2} = \frac{\tilde{\rho}}{1 + \frac{2}{3}b\tilde{\rho}^{1/2}}. \quad (22)$$

Note that, in emergent gravity, the external temperature and thus $\tilde{\rho}$ are fixed, while the cosmological constant Λ (i.e., the vacuum pressure) is adjusted to the thermodynamic equilibrium. This is the reason why, in the emergent gravity, the cosmological constant is always much smaller than its "natural" Planck value: in our case, $\Lambda \sim T_0^4/E_{\text{Planck}}^2 \ll E_{\text{Planck}}^2$.

In the particular case of photon gas with $\bar{\sigma} = 1/36\hbar$, one obtains the following modification of the Einstein point by thermal fluctuations (here, we use $\hbar = c = 1$):

$$\Lambda = \frac{3}{2a^2} = \frac{8}{15}\frac{\pi^3 GT_0^4}{1 + (8/9)\pi GT_0^2}. \quad (23)$$

This corresponds to the original Einstein point with the Newton constant renormalized by thermal fluctuations,

$$\Lambda = \frac{3}{2a^2} = \frac{8}{15}\pi^3\tilde{G}T_0^4, \quad \tilde{G}^{-1} = G^{-1} + \frac{8}{9}\pi T_0^2. \quad (24)$$

For $GT_0^2 \ll 1$, i.e., when $T_0^2 \ll E_{\text{Planck}}^2$, the result in Eq. (23) coincides with that obtained by Altaie and Dowker (see Eqs. (44) and (41) in [14]):

$$\frac{1}{a^2} = \frac{16}{45}\pi^3 GT_0^4\left(1 - \frac{8}{9}\pi GT_0^2\right). \quad (25)$$

This demonstrates that, in equilibrium and in the limit $T_0^2 \ll E_{\text{Planck}}^2$, the thermal correction to the Einstein

point that follows from minimization of the free energy coincides with the result following from the conventional general relativity approach, in which the Einstein equations are solved in a self-consistent manner taking into account thermal fluctuations [14].

Although our treatment here cannot consider the dynamics of the system, we can understand that the general equations for the evolution of an effective FRW universe in contact with a fixed temperature reservoir will be different from that of Einstein. This, in particular, must include the evolution of the "cosmological constant" to its equilibrium value.

5. HOMOGENEOUS BUT ANISOTROPIC PERTURBATIONS

In standard general relativity, the Einstein point for a Universe filled with radiation is also unstable against homogeneous but anisotropic perturbations of the metric of the Bianchi type IX (see, for example, [4]). For completeness, in this section, we want to see whether the Einstein isotropic point is, on the contrary, stable in our approach.

In order to analyze the stability of the Einstein state from our emergent gravity point of view, we need to calculate the free energy of static configurations of the Bianchi IX type, which include the Einstein isotropic configuration. The general metric for these models is [15]

$$ds^2 = -Ndt^2 + \sum_{n=1}^{3} a_n^2\sigma_n^2, \quad (26)$$

$$\sigma_1 = \sin\psi d\theta - \cos\psi\sin\theta d\varphi, \quad (27)$$

$$\sigma_2 = \cos\psi d\theta + \sin\psi\sin\theta d\varphi, \quad (28)$$

$$\sigma_3 = -(d\psi + \cos\theta d\varphi). \quad (29)$$

Now, the free energy for these configurations is

$$F(a_1, a_2, a_3, N, T) = \frac{2\pi^2 a_1 a_2 a_3}{8\pi G}\left[\frac{Na_1^2}{a_2^2 a_3^2} + \frac{Na_2^2}{a_1^2 a_3^2}\right.$$

$$\left. + \frac{Na_3^2}{a_1^2 a_2^2} - \frac{2N}{a_1^2} - \frac{2N}{a_2^2} - \frac{2N}{a_3^2} + N\Lambda - \frac{\tilde{p}}{N^3}\right]. \quad (30)$$

Again, it is not difficult to see that the Einstein point is an extremum of this free energy $a_1^2 = a_2^2 = a_3^2 = (3/2)\Lambda^{-1} = (3/2)\tilde{\rho}^{-1}$ and that it is a local minimum.

6. DISCUSSION

The Einstein static model was introduced as a state of equilibrium for the universe as a whole. A few years after its introduction, it was pointed out that it will be unstable under perturbations. At present, we know that

the issue of the stability of closed and static configurations is not as clear-cut as it was considered to be, although there are still several ways to create instability. For example, a radiation-dominated universe could be made globally unstable by a sudden decrease in pressure in the entire universe.

Here, we have analyzed this global instability of a static universe in the simple case of radiation dominance, but taken a different perspective on the essence of gravity. We have considered that general relativity might be an emergent feature of an underlying quantum theory of a similar nature to that describing a condensed matter system such as liquid helium. In this case (some other cases can also be imagined), it appears reasonable to consider the temperature of the universe as something independent (at least in a first approximation) of the specific characteristics of the emergent four-dimensional geometry. This characteristic put us outside the realm of standard general relativity.

Taking this perspective, we have calculated the free energy for static universes of the Einstein type filled with a gas of photons at a fixed temperature. We have seen that the free energy has an extremum at the Einstein point and that this extremum corresponds to a local minimum. Therefore, thermodynamically speaking, the Einstein state for the universe would be stable under the stated condition.

It is not difficult to understand why this is the case. The Eddington instability of the Einstein state is based on the following fact. The contractive tendency of matter operates more strongly on short scales. Instead, the expansive tendency of the cosmological constant operates more strongly on large scales. In the Einstein point, these two tendencies are exactly balanced. However, if the universe is suddenly made larger, the cosmological constant effect takes over and further expands the universe. Reciprocally, if the universe is made smaller, the matter dominates and causes the universe to further contract. However, in the case analyzed here, a sudden expansion of the universe will be accompanied by the introduction of more photons in the system in order to keep the temperature constant in the now larger volume. This increase in the amount of matter completely counterbalances the cosmological constant tendency making the universe contract back to its initial state.

We also know that the Einstein point is unstable in standard general relativity to homogeneous but anisotropic perturbations of the Bianchi type IX. Taking our point of view, we have calculated the behavior of the Einstein point inside the general class of static Bianchi model of type IX. We have also found that the Einstein point is stable in our approach.

In summary, in the standard general relativistic point of view, the radiation-dominated Einstein state is unstable under global perturbation of the scale factor and also from homogeneous but anisotropic perturbations. However, from the point of view of emergent gravity, these instabilities are not present.

ACKNOWLEDGMENTS

REFERENCES

1. A. Einstein, *Sitzungberichte der Preussischen Akademie der Wissenschaften* (1917), p. 142 [*The Principle of Relativity* (Dover, New York, 1952)].
2. A. S. Eddington, Mon. Not. R. Astron. Soc. **90**, 668 (1930).
3. G. F. R. Ellis and R. Maartens, Class. Quantum Grav. **21**, 223 (2004).
4. J. D. Barrow, G. F. R. Ellis, R. Maartens, and C. G. Tsagas, Class. Quantum Grav. **20**, L155 (2003).
5. G. Lemaître, Mon. Not. R. Astron. Soc. **91**, 490 (1931).
6. W. B. Bonnor, Mon. Not. R. Astron. Soc. **115**, 310 (1954).
7. E. R. Harrison, Rev. Mod. Phys. **39**, 862 (1967).
8. G. W. Gibbons, Nucl. Phys. B **292**, 784 (1987).
9. G. E. Volovik, *The Universe in a Helium Droplet* (Clarendon, Oxford, UK, 2003).
10. G. F. Schutz, Phys. Rev. D **2**, 2762 (1970).
11. G. E. Volovik and A. I. Zelnikov, Pis'ma Zh. Éksp. Teor. Fiz. **78**, 1271 (2003) [JETP Lett. **78**, 751 (2003)].
12. J. W. York, Phys. Rev. D **33**, 2092 (1986).
13. Y. V. Gusev and A. I. Zelnikov, Phys. Rev. D **59**, 024 002 (1999).
14. M. B. Altaie and J. S. Dowker, Phys. Rev. D **18**, 3557 (1978).
15. C. W. Misner, Phys. Rev. Lett. **22**, 1071 (1969).

Quasielastic Triton Knockout from ^{6}Li and ^{7}Li Nuclei by Intermediate-Energy Pions

**B. M. Abramov, Yu. A. Borodin, S. A. Bulychjov, I. A. Dukhovskoy, A. P. Krutenkova*,
V. V. Kulikov, M. A. Martem'yanov, M. A. Matsuk, V. E. Tarasov,
E. N. Turdakina, and A. I. Khanov**

Institute of Theoretical and Experimental Physics, Bol'shaya Cheremushkinskaya ul. 25, Moscow, 117218 Russia
** e-mail: anna.krutenkova@itep.ru*

Quasielastic triton knockout from ^{6}Li and ^{7}Li nuclei by negative pions with momenta $p_0 = 0.72$ and 0.88 GeV/c was studied in the region of backward pion–triton scattering. The experiment was performed at the Institute of Theoretical and Experimental Physics (ITEP, Moscow) on a 3-m magnetic spectrometer equipped with spark chambers. The momentum distributions of the intranuclear quasitriton motion and the excitation-energy spectra of residual nuclei were obtained. © *2004 MAIK "Nauka/Interperiodica".*

PACS numbers: 25.80.Hp

Clusters play an important role in studying the structure of nuclei (see, for example, reviews [1, 2]). Within the cluster approaches, the properties of nuclei are determined both by the properties inherent in the clusters themselves and by their relative motion. Interest in cluster approaches has grown considerably in recent years. This was associated both with the successes achieved by the alpha-particle nuclear models [1, 3] and with the development of methods of projecting [4] the shell wave functions onto the cluster configurations, allowing the difficulties of many-body problem to be surmounted in calculating nuclear reactions. In this work, we explore the quasielastic knockout of fragments (clusters) from nuclei, which is an efficient method for studying the cluster structure of light nuclei. If one measures the kinematic parameters of both the knock-on fragment and the scattered particle (this corresponds to the fully reconstructed kinematics of the experiment), the use of the impulse approximation makes it possible to determine, from the missing energy and momentum, not only the energy of the residual nucleus but also the momentum of the intranuclear motion of the knock-on cluster and the effective number of such clusters in the nucleus under study. This method was previously used by us in [5] to explore backward quasielastic pion–deuteron scattering. That experiment also provided statistics that served as a basis for deriving the results presented below for pion-induced quasielastic triton knockout in the forward direction from ^{6}Li and ^{7}Li nuclei in the reactions

$$\pi^- + {}^6\text{Li} \longrightarrow t + \pi^- + \text{X} \tag{1}$$

and

$$\pi^- + {}^7\text{Li} \longrightarrow t + \pi^- + \text{X}. \tag{2}$$
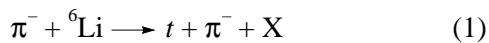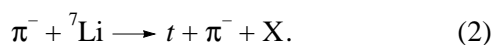
In particular, the excitation-energy spectra of residual nuclei X and the momentum distributions for the intranuclear motion of a quasitriton were constructed on this basis. Both target nuclei can be considered [6, 7] as the two-cluster systems, ^{6}Li $\longrightarrow t + {}^3$He and ^{7}Li $\longrightarrow t + {}^4$He, whose quasitriton cluster is involved in the aforementioned reactions.

Our experiment was performed using a negative pion beam with momenta $p_0 = 0.72$ and 0.88 GeV/c from the 10-GeV proton synchrotron of the Institute of Theoretical and Experimental Physics (ITEP, Moscow). Use was made of a 3-m magnetic spectrometer equipped with spark chambers placed in a magnetic field (see [8]). The magnetic field existed over a rather large volume ($3 \times 0.5 \times 1$ m^3), and this made it possible to perform, for a target positioned near the center of the magnet, a complete kinematic analysis of the reaction of interest—that is, to measure both the momentum of a triton knocked out in the forward direction ($\theta_{\text{lab}} \lesssim 10°$) and the momenta of the incident-beam and backscattered pion. Targets from ^{6}Li with isotopic composition 90.4% ^{6}Li and 9.6% ^{7}Li and from ^{7}Li of natural isotopic composition (7.52% ^{6}Li and 92.48% ^{7}Li) were prepared in the form of solid cylinders 9.5 cm long and 8 cm in diameter that were surrounded by 0.1-mm-thick walls from stainless steel. All targets were mounted on a disk, whose rotation allowed the required target to be exposed to the beam. An important point was that the quasielastic proton knockout [9] and quasielastic deuteron knockout [5] reactions, each characterized by a much larger cross section, were simultaneously measured in this experiment. This provided a reliable calibration in separating reaction events for (1) and (2). For a positively charged particle emitted
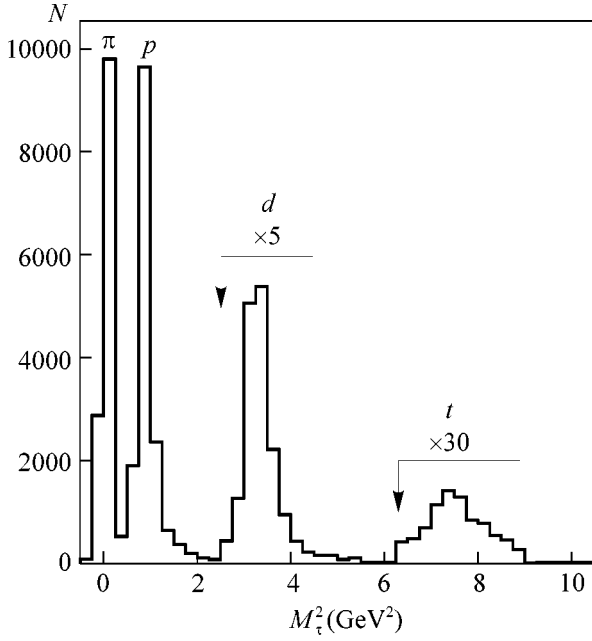
Fig. 1. Distribution in the squared mass M_τ^2 of a forward emitted particle in the $\pi^- + A \longrightarrow (\pi^+, p, d, t) + X$ reactions.

from a target in the forward direction, the time of flight was determined on a base of ~6 m by using a system of hodoscopic scintillation counters having an area of 0.7×2.1 m^2. The distribution of events with respect to the squared mass M_τ^2 of a particle emitted in the forward direction is shown in Fig. 1 according to a calculation based on its measured momentum and time of flight. The reactions involving triton knockout were separated using the criterion $6.3 \leq M_\tau^2 \leq 8.9$ GeV^2. For these events, we calculated the missing momentum

$$\mathbf{p}_F = \mathbf{p}_0 - \mathbf{p}_t - \mathbf{p}_{\pi^-} \qquad (3)$$

and the missing energy

$$E_{\mathrm{miss}} = T_0 - T_t - T_{\pi^-} - T_X, \qquad (4)$$

where T stands for kinetic energy; the indices 0, π^-, t, and X label the energies and momenta for, respectively, the incident and final pions, the triton, and the residual nucleus X; $T_X = (\mathbf{p}_F)^2/2M$; and M is the residual nucleus mass. The further analysis was performed in the plane-wave impulse approximation, and the corresponding pole diagram for reaction (1) is displayed in Fig. 2. In this approximation, one identifies the missing momentum $\mathbf{p}_F$ with the intranuclear momentum of a quasitriton cluster and the missing energy E_{miss} with the excitation energy of the residual nucleus. For ^{6}Li and ^{7}Li, Fig. 3 shows the E_{miss} distributions for the total statistics accu-

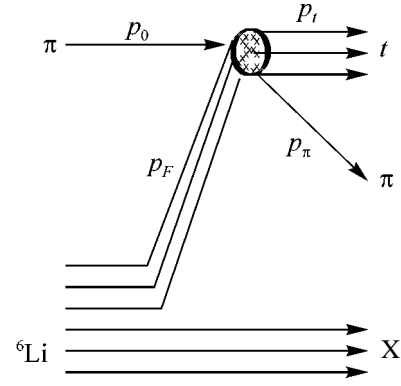**Fig. 2.** Diagram corresponding to the plane-wave impulse approximation.

mulated for $p_0 = 0.72$ and 0.88 GeV/c. At low values of E_{miss}, both distributions exhibit a distinct peak associated with the quasielastic pion–triton scattering in the backward direction. In the case of X = ^{3}He, the position of this peak for ^{6}Li is determined by the quasitriton binding energy ($E_b = 15.8$ MeV [6]) in the ^{6}Li nucleus; that is, $E_{\mathrm{miss}} = 15.8$ MeV. The reaction thresholds for X = $p + d$ and X = $p + p + n$ lie higher by 6 and 8 MeV, respectively. The experimental resolution $\sigma = 15$–18 MeV of our facility with respect to E_{miss} is insufficient for separating these reactions. The position of the peak associated with quasielastic pion–triton scattering on ^{7}Li for X = ^{4}He is determined by the quasitriton binding energy ($E_b = 2.5$ MeV [6]) in the ^{7}Li nucleus;
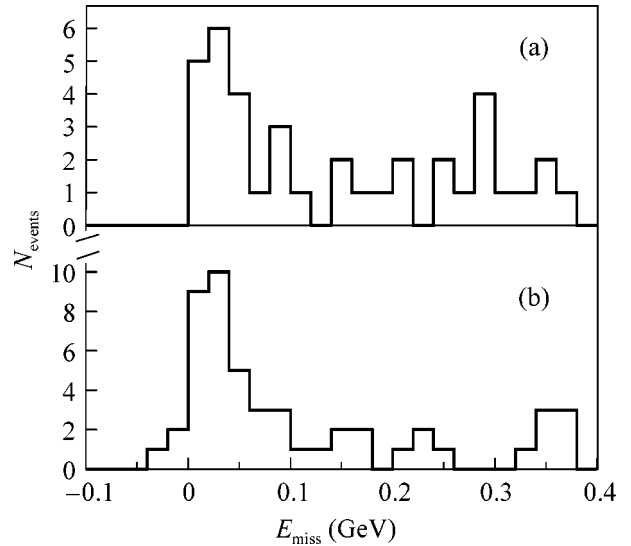

Fig. 3. Missing-energy (E_{miss}) distribution in the reactions $\pi^- + {}^{6,7}\mathrm{Li} \longrightarrow t + \pi^- + X$ for the total statistics accumulated at $p_0 = 0.72$ and 0.88 GeV/c for (a) ^{6}Li and (b) ^{7}Li.

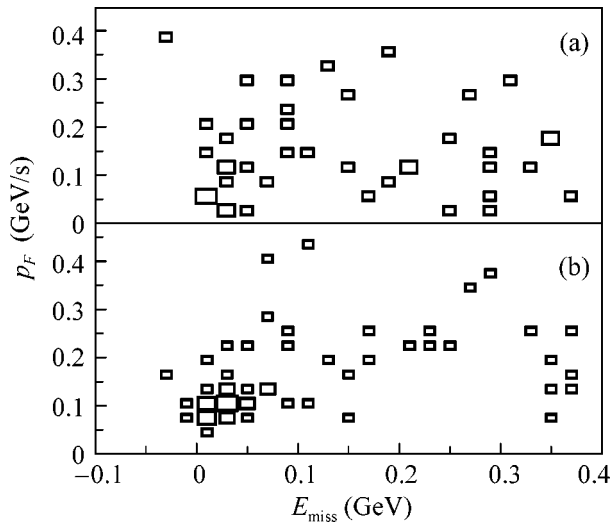**Fig. 4.** Momentum of the intranuclear motion of a quasitriton in the reactions $\pi^- + {}^{6,7}\mathrm{Li} \longrightarrow t + \pi^- + \mathrm{X}$ as a function of E_{miss}: (a) results for a ${}^6\mathrm{Li}$ target and (b) results for a ${}^7\mathrm{Li}$ target.
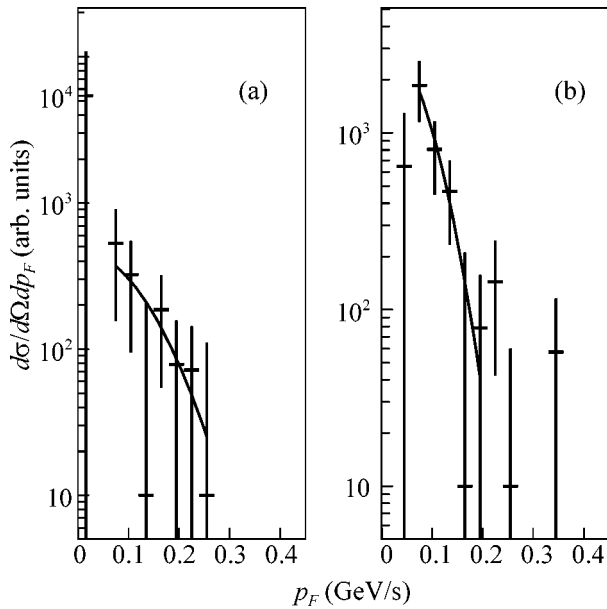

Fig. 5. Distributions of events in the momentum of the intranuclear motion of a quasitriton in the reactions $\pi^- + {}^{6,7}\mathrm{Li} \longrightarrow t + \pi^- + \mathrm{X}$ for the interval $-0.010 \leq E_{\mathrm{miss}} \leq 0.050$ GeV: (a) results for a ${}^6\mathrm{Li}$ target and (b) results for a ${}^7\mathrm{Li}$ target. The curves correspond to the Gaussian distribution $\exp(-p_F^2/\kappa^2)$, where $\kappa = 149 \pm 56$ and 93 ± 18 MeV/c for ${}^6\mathrm{Li}$ and ${}^7\mathrm{Li}$, respectively.

that is, $E_{\mathrm{miss}} = 2.5$ MeV. The reaction thresholds for $\mathrm{X} = d + d$, $\mathrm{X} = p + n + d$, and $\mathrm{X} = p + n + p + n$ lie higher by 25, 27, and 29 MeV, respectively. For ${}^7\mathrm{Li}$, the quasielas-

tic peak corresponding to quasitriton knockout is more distinct, which is seen most clearly in the two-dimensional p_F versus E_{miss} distribution (see Fig. 4). In contrast to what we have for ${}^6\mathrm{Li}$, there is a pronounced concentration of events at low p_F and E_{miss} in this distribution for ${}^7\mathrm{Li}$. This is indicative of a higher weight of the quasitriton component in the ${}^7\mathrm{Li}$ than in the ${}^6\mathrm{Li}$ nucleus.

The differential momentum distributions of the intranuclear motion of a quasitriton are shown in Fig. 5. They were approximated by the Gaussian functions $\exp(-p_F^2/\kappa^2)$. For the interval $-0.010 \leq E_{\mathrm{miss}} \leq 0.050$ GeV, the values of the parameter κ proved to be $\kappa = 149 \pm 56$ MeV/c for ${}^6\mathrm{Li}$ and $\kappa = 93 \pm 18$ MeV/c for ${}^7\mathrm{Li}$. They are greater than the values of $\kappa = 56 \pm 8$ MeV/c for ${}^6\mathrm{Li}$ and $\kappa = 82 \pm 11$ MeV/c for ${}^7\mathrm{Li}$ obtained for the momenta of intranuclear motion of quasideuterons from quasielastic pion–deuteron scattering in these nuclei for the incident momentum $p_0 = 0.72$ GeV/c [5, 10]. The parameter $\kappa = 100 \pm 20$ MeV/c, which was obtained for the intranuclear motion of tritons in the measurement of quasielastic triton knockout by 590-MeV protons from ${}^6\mathrm{Li}$ in a kinematically complete experiment [11], agrees with our experimental results, which, in turn, agrees with the results of the calculations performed in [12, 13]. Unfortunately, we are unaware of any similar calculations for the ${}^7\mathrm{Li}$ nucleus. Since there are no data on elastic pion–triton scattering (or on isotopically conjugate pion scattering on ${}^3\mathrm{He}$ nuclei) at the energies of our experiment and at high momentum transfers, we are unable to estimate the effective number of quasitritons in lithium nuclei.

REFERENCES

1. H. Horiuchi, Nucl. Phys. A **522**, 257 (1991).

2. E. T. Ibraeva, Fiz. Élem. Chastits At. Yadra **34**, 269 (2003).

3. A. Arima, nucl-th/0405078.

4. V. T. Voronchev, V. I. Kukulin, V. N. Pomerantsev, *et al.*, Yad. Fiz. **57**, 1964 (1994) [Phys. At. Nucl. **57**, 1890 (1994)]; Few-Body Syst. **18**, 191 (1995).

5. B. M. Abramov, Yu. A. Borodin, S. A. Bulychev, *et al.*, Pis'ma Zh. Éksp. Teor. Fiz. **74**, 504 (2001) [JETP Lett. **74**, 449 (2001)].

6. F. Ajzenberg-Selove, Nucl. Phys. A **490**, 1 (1988).

7. M. I. Adamovich, V. Bradnova, S. Vokal, *et al.*, Yad. Fiz. **67**, 533 (2004) [Phys. At. Nucl. **67**, 514 (2004)].

8. B. M. Abramov, Yu. A. Borodin, S. A. Bulychjov, *et al.*, Nucl. Phys. A **723**, 389 (2003).

9. B. M. Abramov, Yu. A. Borodin, S. A. Bulychev, *et al.*, Pis'ma Zh. Éksp. Teor. Fiz. **71**, 524 (2000) [JETP Lett. **71**, 359 (2000)].

10. B. M. Abramov, Yu. A. Borodin, S. A. Bulychev, *et al.*, Yad. Fiz. (in press).

11. W. Dollhopf, C. Lunke, C. F. Perdrisat, *et al.*, Phys. Rev. C **8**, 877 (1973).

12. Yu. A. Kudeyarov, I. V. Kurdyumov, V. G. Neudachin, and Yu. F. Smirnov, Nucl. Phys. A **163**, 316 (1971).

13. I. V. Kurdyumov, V. G. Neudachin, Yu. F. Smirnov, and V. P. Korennoy, Phys. Lett. B **40B**, 607 (1972).

Translated by A. Isaakyan

Expansion in Feynman Graphs as Simplicial String Theory[¶]

E. T. Akhmedov

Institute of Theoretical and Experimental Physics, Moscow, 117259 Russia

Institute for Advanced Study, Joint Institute for Nuclear Research, Dubna, Moscow region, 141980 Russia

e-mail: akhmedov@itep.ru

Received July 8, 2004

We show that the series expansion of quantum field theory in Feynman diagrams can be explicitly mapped on the partition function of simplicial string theory—the theory describing embeddings of two-dimensional (2D) simplicial complexes into the spacetime of the field theory. The summation over 2D geometries in this theory is obtained from the summation over the Feynman diagrams and the integration over the Schwinger parameters of the propagators. We discuss the meaning of the obtained relation and derive the one-dimensional analog of the simplicial theory using the example of a free relativistic particle. © *2004 MAIK "Nauka/Interperiodica".*

PACS numbers: 11.25.-w

1. There is hope that the large-N Yang–Mills theory is exactly equivalent to string theory [1]. Such a string theory, if it exists, can reveal the integrability of the large-N Yang–Mills theory. Hence, the theory will help in explaining the confinement phenomenon.

Despite the recent progress [2, 3] in the case of (super)conformal theories, we still do not understand the relation between gauge and string theories. We do not understand which features of the relation are generic (persist at least for nonconformal and/or nonsupersymmetric cases) and which are specific for the concrete relation of [2]. This is due to the fact that there is no explicit proof of AdS/CFT correspondence [2, 3].

In an attempt to understand the relation between field and string theories in general, we present, in this note, an explicit map from the functional integral of the matrix field theory (at finite N) onto the partition function of the simplicial string theory—the theory describing embeddings of the two-dimensional (2D) simplicial complexes into the spacetime of the field theory. Our considerations are quite generic and can be applied to the Yang–Mills theory. However, we consider the model example of the matrix Φ^3 theory whose interpretation on the string theory side we understand best of all.

The map in question is given by a duality transformation. To some extent, this duality is the lattice analog of the T-duality map, although we do not have any compact dimensions. Via this transformation, we map the summation over the Feynman diagrams and the integration over the Schwinger parameters onto the sum over triangulations of the 2D surfaces and integration over the invariant 2D distances between the vertices of the

simplicial complexes. This seems to be a summation over *all* 2D geometries and *all* embeddings of the simplicial complexes into spacetime. To understand this point, we consider the toy example of a free relativistic particle, for which we present a similar expression. There, the summation over *all* one-dimensional (1D) geometries is given by summation over 1D "triangulations" and integrations over the lengths between the vertices of the "triangulations." The integration over all positions of the vertices gives the sum over *all* possible embeddings. The resulting "triangulated" expression is *exactly equivalent* to the relativistic particle path integral. No continuum limit should be taken.

However, a complete understanding of the simplicial string theory—at least its possible continuum formulation, or maybe a continuum limit of it—is still lacking. In particular, it is possible that, in the continuum formulation, the theory describes strings in the curved AdS_5 space rather than in R^4 [4].

Anyway, as usual, the relation between two theories can be useful for both of them. In fact, the map in question at least can give an unambiguous way of formulating the simplicial string theory. Particularly, the measure of integration and the 2D gravity action unambiguously follow from the matrix field theory.

The structure of the paper is as follows. In Section 2, we present the map between the two theories. In Section 3, we present an interpretation of the resulting dual expression obtained in Section 2. In Section 4, we consider the example of the free relativistic particle and present a simplicial path that is integral for it. We conclude with he discussion in Section 5. In the Appendix, we present a simple proof of the well-known combinatoric formulas [5] for the Feynman integrals. These formulas acquire a new meaning after the relation of the

---

[¶] This article was submitted by the author in English.

field theory to the simplicial string theory is established.

2. Consider the matrix scalar field theory in the D-dimensional Euclidian space:

$$Z = \int D\hat{\Phi}(x)$$

$$\times \exp\left\{-\int d^D x N \mathrm{Tr}\left[\frac{1}{2}|\boldsymbol{\partial}\hat{\Phi}|^2 + \frac{1}{2}m^2|\hat{\Phi}|^2 + \frac{\lambda}{3}\hat{\Phi}^3\right]\right\},$$ (1)

where $\boldsymbol{\partial} = (\partial/\partial x_1, \ldots, \partial/\partial x_D)$ and $\hat{\Phi}$ is an $N \times N$ matrix field in the adjoint representation of $U(N)$ group: Φ^{ij}, i, $j = 1, \ldots, N$. Note that we have rescaled the fields, so that λ is the t'Hooft coupling constant, but we are *not* taking the large N limit in this note.

The problems of this field theory, due to the sign indefiniteness of the Φ^3 potential, are not relevant for most of our further considerations. We consider the functional integral Z as a formal series expansion in the powers of λ. To deal with connected graphs, we consider $\log Z$.

It is well known that $\log Z$ can be represented as (see, e.g., [6, 7])

$$\log Z = \sum_{g=0}^{\infty} N^{\chi(g)} \sum_{V=0}^{\infty} \lambda^V C(V, g)$$

$$\times \int_0^{+\infty} \prod_{n=1}^{L} d\alpha_n \int \prod_{i=1}^{V} d^D \mathbf{y}_i \int \prod_{m=1}^{L} d^D \mathbf{p}_m$$ (2)

$$\times \exp\left\{-\sum_{l=1}^{L}\left[\frac{\alpha_l(\mathbf{p}_l^2 + m^2)}{2} - i\mathbf{p}_l(\Delta_l\mathbf{y})\right]\right\},$$

where $\mathbf{p}_l$ is the momentum running along the propagator l; the propagators are written in the Schwinger α-representation; the first sum is taken over the genera g of the discretized closed 2D surfaces represented by the fat Feynman diagrams[1] [7]; the second sum is taken over the number V of the insertions of $\mathrm{Tr}\hat{\Phi}^3$ ($\mathbf{y}_i$) vertices; $\chi(g) = V - L + F$ is the Euler characteristic corresponding to the genus g diagram in the sum with V ver-

---

[1] Each member in the sum in Eq. (2) is represented by a fat three-valent (three links enter each of the V vertices) graph. Such a closed graph represents a vacuum amplitude of the theory in Eq. (1). The generalization of our considerations for the correlators (open graphs) is straightforward.

tices, L propagators, and F faces;[2] $\Delta_l\mathbf{y}$ is the difference of the target space positions of the ends of the lth propagator; and $C(V, g)$ are constants that can be found from the genus expansion of the matrix integrals (see, e.g., [8, 9]),

$$\int d\hat{\Phi}\exp\left\{-N\mathrm{Tr}\left[\frac{1}{2}\hat{\Phi}^2 + \frac{\lambda}{3}\hat{\Phi}^3\right]\right\}$$

$$= \sum_{g=0}^{\infty} N^{\chi(g)} \sum_{V=0}^{\infty} \lambda^V C(V, g).$$ (3)

For the general D, most of the integrals under the sum in Eq. (2) are divergent. One of the types of divergences is proportional to the volume of the spacetime and is just due to the translational invariance. To get rid of this divergence, we can skip one of the L integrations over the momenta. Another type of divergence is the standard ultraviolet (UV) divergences of quantum field theory. We discuss them below.

We will perform a transformation over Eq. (2). The same kind of transformation is performed in [10] and is referred to as duality on the lattice. As well, a somewhat similar transformation is made in [11] and relates some types of Feynman diagrams of the Φ^3 theory to the amplitudes in conformal quantum mechanics.

To do this transformation, let us perform integration over the y's. Then, each term under the sum and integration over α's is represented as the *finite* function,

$$I(L, V, \{\alpha\}) = \int \prod_{m=1}^{L} d^D \mathbf{p}_m \prod_{i=1}^{V} \delta\left(\sum_{l(\to i)} \mathbf{p}_l\right)$$

$$\times \exp\left\{-\sum_{l=1}^{L} \frac{\alpha_l(\mathbf{p}_l^2 + m^2)}{2}\right\},$$ (4)

where, in each of the V δ-functions, the sum goes over the three links terminating on each of the V vertices. There are momentum conservation conditions at each vertex. The UV divergences in the diagrams appear after the integrations over the α's. To perform the transformation in question, we consider integrand expressions, because we would like to show that this transformation gives a nontrivial relation between the two partition functions rather than a formal map from one infinite number onto another. At the same time, the divergences have a clear physical meaning on the both sides of the relation as is argued in the next section.

---

[2] Do not confuse this number with the number G of the momentum loops of the diagram; F is the number of closed index loops of the *fat* Feynman diagram.

The conditions that are imposed by the V δ-functions are usually solved via $G = L - V + 1$ independent momenta running along the loops of the diagram. However, we are going to solve them via the dual graph to the Feynman diagram under consideration. The dual graph consists of the vertices sitting in the centers of the faces of the Feynman diagram, and its links pass through the centers of the propagators of the Feynman diagram. Thus, the dual graph to a three-valent Feynman diagram represents the triangulation of a 2D surface. The faces of the dual graphs are triangles.

Then, each of the L momenta $\mathbf{p}_l$ obeying conditions $\sum_{l(\to i)}^{3} \mathbf{p}_l = 0$ can be represented as[3]

$$\mathbf{p}_l = \Delta_l \mathbf{x} + \sum_{s=1}^{2g} \boldsymbol{\mu}_s \omega_l^{(s)}, \tag{5}$$

where $\Delta_l \mathbf{x}$ is the difference of the target space positions of the ends of the link l of the dual graph (which is intersecting the lth propagator of the Feynman diagram), $\boldsymbol{\mu}_s$ are arbitrary parameters, and $\omega_l^{(s)}$ are $2g$ closed (but not exact) one-forms on the genus g simplicial complex defined by the dual graph. To explain these observations, let us point out that the condition $\sum_{l(\to i)}^{3} \mathbf{p}_l = 0$ is equivalent to the D 2D $d\mathbf{p} = 0$ conditions on the lattice [10]. The solutions of these conditions are $\mathbf{p} = d\mathbf{x} + \sum_{s=1}^{2g} \boldsymbol{\mu}_s \omega^{(s)}$, $d\omega^{(s)} = 0$ for all s whose lattice expression is Eq. (5).

Using this solution, we obtain

$$\log Z = \sum_{g=0}^{\infty} N^{\chi(g)} \sum_{V=0}^{\infty} \lambda^V C'(V, g)$$

$$\times \int \prod_{s=1}^{2g} d^D \boldsymbol{\mu}_s \left[\det\left(\sum_{n,m=1}^{L} \omega_n^{(s)} \omega_m^{(s')} \right) \right]^{D/2}$$

---

[3] Note that the momenta under the sums $\sum_{l(\to i)}^{3} \mathbf{p}_l = 0$ have alternating signs. Some momenta are entering the vertex, while the others are exiting from it. This obviously means that the links of the Feynman diagram have orientations. Hence, the links of the dual graph should have synchronized orientations (with the Feynman diagram) to be defined in Eq. (5) which, of the edge x's, enters with "+" and has a "−" sign in the corresponding p, so that all the momentum conservation conditions are fulfilled [12].

$$\times \int_0^{+\infty} \prod_{n=1}^{L} d\alpha_n \int \prod_{a=1}^{F} d^D \mathbf{x}_a \exp\left\{ -\sum_{l=1}^{L} \frac{\alpha_l}{2} \right.$$

$$\left. \times \left[(\Delta_l \mathbf{x})^2 + \left(\sum_{s=1}^{2g} \boldsymbol{\mu}_s \omega_l^{(s)} \right)^2 + m^2 \right] \right\} \tag{6}$$

$$= \sum_{g=0}^{\infty} N^{\chi(g)} \sum_{V=0}^{\infty} \lambda^V C'(V, g) \int_0^{+\infty} \prod_{n=1}^{L} \frac{d\alpha_n}{\alpha_n^{gD}} e^{-\frac{\alpha_n m^2}{2}}$$

$$\times \int \prod_{a=1}^{F} d^D \mathbf{x}_a \exp\left\{ -\sum_{l=1}^{L} \frac{\alpha_l}{2} (\Delta_l \mathbf{x})^2 \right\},$$

where $C'(V, g)$ is different from $C(V, g)$ by the $D/2$ power of the determinant of the matrix relating p's and x's in Eq. (5) and F is the number of the vertices (faces) of the dual (Feynman) graph. In Eq. (6), we have used the fact that ω's are closed.

In the next section, we interpret the expression in Eq. (6) as the simplicial string theory. In this context, the summations over the genera, triangulations, and integrations over the α's give the summation over internal 2D geometries. The integration over the x's—the positions of the vertices—gives the summation over the embeddings.

It is worth mentioning at this point that all our considerations so far can be easily generalized to higher valent fat graphs (i.e., to the matrix Φ^n, $n \geq 4$ theory or to non-Abelian gauge theories). However, the resulting dual graphs in these cases contain more complicated simplexes than just triangles [12].

3. The definition of the simplicial string theory is well known [13]. We present it here to make the interpretation of Eq. (6) obvious. First, the internal metric on a simplicial complex is given by

$$\|h_{\alpha\beta}\|_\nabla = \|\mathbf{e}_\alpha \mathbf{e}_\beta\|_\nabla = \begin{pmatrix} \mathbf{e}_1^2 & \mathbf{e}_1 \mathbf{e}_2 \\ \mathbf{e}_1 \mathbf{e}_2 & \mathbf{e}_2^2 \end{pmatrix}$$

$$= \begin{pmatrix} e_1^2 & \frac{1}{2}[e_1^2 + e_2^2 - e_3^2] \\ \frac{1}{2}[e_1^2 + e_2^2 - e_3^2] & e_2^2 \end{pmatrix}, \tag{7}$$

where $\mathbf{e}_\alpha$, $\alpha = 1, 2$ are 2D vectors that set the zweibein. They are along two edges of each triangle ∇ of the simplicial complex. As well, $e_{1,2,3}$ are lengths of the three edges of these triangles. Second, the external metric on a simplicial complex is given by

$$\|G_{\alpha\beta}\|_{\nabla} = \begin{pmatrix} (\Delta_1\mathbf{x})^2 & \Delta_1\mathbf{x}\Delta_2\mathbf{x} \\ \Delta_1\mathbf{x}\Delta_2\mathbf{x} & (\Delta_2\mathbf{x})^2 \end{pmatrix} = \begin{pmatrix} (\Delta_1\mathbf{x})^2 & \frac{1}{2}[(\Delta_1\mathbf{x})^2 + (\Delta_2\mathbf{x})^2 - (\Delta_3\mathbf{x})^2] \\ \frac{1}{2}[(\Delta_1\mathbf{x})^2 + (\Delta_2\mathbf{x})^2 - (\Delta_3\mathbf{x})^2] & (\Delta_2\mathbf{x})^2 \end{pmatrix}, \qquad (8)$$

where $\Delta_{1,2,3}\mathbf{x}$ are differences of the target space positions of the vertices of each triangle of the simplicial complex. Hence, the discretization of the string theory action is as follows:

$$S = \int d^2\sigma \sqrt{h} h^{ab}\partial_a\mathbf{x}\partial_b\mathbf{x} \Rightarrow \sum_{\nabla}\sqrt{h_{\nabla}}\mathrm{Tr}(\|h\|_{\nabla}^{-1}\|G\|_{\nabla})$$

$$= \sum_{\nabla}\frac{[(\Delta_1\mathbf{x})^2(e_2^2 + e_3^2 - e_1^2) + (\Delta_2\mathbf{x})^2(e_1^2 + e_3^2 - e_2^2) + (\Delta_3\mathbf{x})^2(e_1^2 + e_2^2 - e_3^2)]_{\nabla}}{2\sqrt{h_{\nabla}}}. \qquad (9)$$

Here, the sum is going over all triangles of a simplicial complex, and

$$h_{\nabla} = \frac{1}{4}[(e_2^2 + e_3^2 - e_1^2)(e_1^2 + e_3^2 - e_2^2)$$

$$+ (e_2^2 + e_3^2 - e_1^2)(e_1^2 + e_2^2 - e_3^2) \qquad (10)$$

$$+ (e_1^2 + e_2^2 - e_3^2)(e_1^2 + e_3^2 - e_2^2)]_{\nabla}$$

is the determinant of the internal metric. Thus, it is natural to define the partition function of the simplicial string theory as

$$Z_{sst} = \sum_{\text{Triangulations}} \int [de]_{\text{Triangulation}} e^{-S(e)}$$

$$\times \prod_{a=1}^{F} d^D\mathbf{x}_a \exp\left\{ -\sum_{l=1}^{L} \frac{\alpha_l(e)(\Delta_l\mathbf{x})^2}{2} \right\}, \qquad (11)$$

where F is the number of vertices of the triangulation under the sum and $\alpha_l(e)$, as follows from Eqs. (9) and (10), are the positive functions of the lengths of the edges of the two triangles glued together via the link l. What is left to be defined are the measure $[de]$ and the weight $S(e)$ of the summation over the 2D geometries. If we would like to integrate over the e's themselves, we have to impose the triangle inequalities into the measure to keep the metric positive defined.

Now, we can point out the equivalence between Eq. (6) and Eqs. (9)–(11) with the suitable choice of $[de]$ and $S(e)$. In fact, the measure and the weight for the summation over the 2D geometries in Eq. (6) unambiguously follow from the matrix field theory. This measure is very natural because the integration goes over the α's rather than e's, which demand triangle inequalities to be imposed [12]. However, the expressions for the discretized versions of the standard gravity actions in terms of the α's are not known. This explains the reason why, usually in the formulation of the simplicial string theory, one is trying to express everything through the e's rather than the α's [13].

It is worth mentioning at this point that the UV divergences of the quantum field theory in Eq. (1) acquire a clear interpretation in the simplicial string theory description. These divergences are just due to the boundaries in the space of all metrics, i.e., due to the degenerate metrics, which correspond to such situations as when some of the triangles degenerate into links. In this context, it is interesting to understand the meaning of the renormalization group within the simplicial string theory context (see [14] for the attempts of the explanation).

Note that Eqs. (11) and (6) are explicitly reparametrization-invariant, because there the integration goes over all reparametrization-invariant 2D lengths between the vertices of the simplicial complexes and over the target space position x's of the vertices rather than over the maps [12]. In the next section, we will present a similar situation for the relativistic particle. After that, we will be ready for the discussion of the 2D situation.

4. Consider the path integral for the relativistic particle,

$$G(\mathbf{x}, \mathbf{x}') = \int_{\mathbf{x}}^{\mathbf{x}'} D\mathbf{x}(\tau) \int \frac{De(\tau)}{VolDiff}$$

$$\times \exp\left\{ -\frac{1}{2}\int_0^1 d\tau \left[\frac{\dot{\mathbf{x}}^2}{e(\tau)} + m^2 e(\tau) \right] \right\} \qquad (12)$$

with measures following from the norms

$$\|\delta \mathbf{x}(\tau)\|^2 = \int_0^1 d\tau e(\tau)[\delta \mathbf{x}(\tau)]^2 = T\int_0^1 df[\delta \mathbf{x}(f)]^2,$$

$$\|\delta e(\tau)\|^2 = \int_0^1 d\tau e(\tau)\left[\frac{\delta e(\tau)}{e(\tau)}\right]^2. \tag{13}$$

The answer for this path integral is [1]

$$G(\mathbf{x}, \mathbf{x}') \propto \int_0^\infty \frac{dT}{\sqrt{T}} \, \det^{\frac{1-D}{2}}\left(-\frac{1}{T^2}\frac{d^2}{df^2}\right)$$

$$\times \exp\left\{-\frac{1}{2}\left[\frac{(\mathbf{x}-\mathbf{x}')^2}{T} + m^2 T\right]\right\}. \tag{14}$$

In the ζ-function regularization, we obtain

$$G(\mathbf{x}, \mathbf{x}') = \int_0^{+\infty} \frac{dT}{T^{D/2}} \exp\left\{-\frac{1}{2}\left[\frac{(\mathbf{x}-\mathbf{x}')^2}{T} + m^2 T\right]\right\}$$

$$= \int \frac{d^D\mathbf{p}}{(2\pi)^D} \frac{e^{i\mathbf{p}(\mathbf{x}-\mathbf{x}')}}{\mathbf{p}^2 + m^2}. \tag{15}$$

Thus, $G(\mathbf{x}, \mathbf{x}')$ is the Green's function of the Klein–Gordon equation.

At the same time, there is another reparametrization-invariant regularization for the path integral of the relativistic particle, the lattice regularization, where the lattice spacings are reparametrization-invariant one-lengths. In this regularization naively, one has ($T = \sum_{i=0}^{M} e_i$)

$$\det^{-\frac{1}{2}}\left(-\frac{1}{T^2}\frac{d^2}{df^2}\right) = \int D\lambda(\tau)\exp\left\{-\int_0^1 \frac{\dot{\lambda}^2(\tau)}{2e(\tau)}d\tau\right\}$$

$$\longrightarrow \int \sqrt{e_0}\prod_{i=1}^{M}\sqrt{e_i}d\lambda_i\exp\left\{-\sum_{j=0}^{M}\frac{(\lambda_{j+1}-\lambda_j)^2}{2e_j}\right\} \propto \frac{\prod_{i=0}^{M}e_i}{T^{\frac{1}{2}}}, \tag{16}$$

where

$$\|\delta\lambda\|^2 = \int_0^1 d\tau e(\tau)[\delta\lambda(\tau)]^2 \longrightarrow \sum_{0=1}^{M} e_i(\delta\lambda_i)^2,$$

$$e_i = \int_{i\Delta\tau}^{(i+1)\Delta\tau} e(\tau)d\tau,$$

and $\delta\lambda_0 = \delta\lambda_{M+1} = 0$. Note that e's are invariant 1D lengths. If this expression for the determinant is substituted into Eq. (14), we obtain

$$G_{\text{Latt}}(\mathbf{x}, \mathbf{x}') = C_M \int \frac{d^D\mathbf{p}}{(2\pi)^D}\frac{e^{i\mathbf{p}(\mathbf{x}-\mathbf{x}')}}{(\mathbf{p}^2+m^2)^{M-DM/2}}. \tag{17}$$

Here, C_M is some constant.

It seems that the naive lattice regularization does not work. However, for this case, we can present a multiple integral expression that solves the Klein–Gordon equation [12]. To obtain it, note that, in contrast, with respect to the evolution-type equations,[4] the Green's function of the Klein–Gordon equation has the following feature:

$$\int \prod_{i=1}^{M} d^D\mathbf{y}_i G(\mathbf{x}, \mathbf{y}_1)G(\mathbf{y}_1, \mathbf{y}_2)\ldots G(\mathbf{y}_M, \mathbf{x}')$$

$$= \int \frac{d^D\mathbf{p}}{(2\pi)^D}\frac{e^{i\mathbf{p}(\mathbf{x}-\mathbf{x}')}}{(\mathbf{p}^2+m^2)^{M+1}} \neq G(\mathbf{x}, \mathbf{x}'). \tag{18}$$

However, it is easy to correct this formula in such a way that the equality will hold. For example, we can put (for any M)

$$G(\mathbf{x}, \mathbf{x}') \propto \int \prod_{i=1}^{M} d^D\mathbf{y}_i\prod_{j=0}^{M}\frac{d^D\mathbf{p}_j}{(2\pi)^D}d\left(\sum_{k=0}^{M} e_k\right)$$

$$\times \exp\left\{\sum_{m=0}^{M}\left[i\mathbf{p}_m(\mathbf{y}_{m+1}-\mathbf{y}_m)-\frac{1}{2}(\mathbf{p}_m^2+m^2)e_m\right]\right\}$$

$$\propto \int \prod_{i=1}^{M} d^D\mathbf{y}_i\frac{d\left(\sum_{j=0}^{M} e_j\right)}{\prod_{n=0}^{M} e_n^{D/2}} \tag{19}$$

$$\times \exp\left\{-\frac{1}{2}\sum_{m=0}^{M}\left[\frac{(\mathbf{y}_{m+1}-\mathbf{y}_m)^2}{e_m}+m^2 e_m\right]\right\},$$

where $\mathbf{y}_0 = \mathbf{x}$ and $\mathbf{y}_{M+1} = \mathbf{x}'$. In this formula, we take the integral over the moduli $\sum_{i=0}^{M} e_i = T$ rather than over all e's, and the expression under this integral depends on T rather than all e's separately. The latter fact can be seen explicitly after the integration over y's.

The expression in Eq. (19) seems to be a good candidate for "proper discretization" of the relativistic particle path integral. However, due to the integration over T rather than each separate e, this integral does not

_____

[4] Which obey $K(\mathbf{x}, \mathbf{x}'|(M+1)\Delta\tau) = \int\prod_{i=1}^{M} d^D\mathbf{y}_i K(\mathbf{x}, \mathbf{y}_1|\Delta\tau)K(\mathbf{y}_1, \mathbf{y}_2|\Delta\tau)\ldots K(\mathbf{y}_M, \mathbf{x}'|\Delta\tau)$.

seem to have a good local field theory interpretation. Note that, obviously,

$$\int d\left(\sum_{i=0}^{M} e_i\right)\ldots \neq \int \frac{\prod_{i=0}^{M} de_i}{VolDiff}\ldots \qquad (20)$$

for any M. This is the main difference from the above case of the relativistic particle *path integral* when the limit $M = \infty$ is appropriately taken and the ζ-function regularization instead of the lattice one is applied.

To obtain the integration over all e's, let us perform the following trick. Consider the equality

$$\frac{1}{\mathbf{p}^2 + m^2} \propto \sum_{L=0}^{\infty} \frac{(-1)^L}{L!} \int_0^{+\infty} \prod_{l=1}^{L} \frac{de_l}{e_l}$$

$$\times \exp\left\{-\frac{(\mathbf{p}^2 + m^2)}{2}\sum_{n=0}^{L} e_n\right\}. \qquad (21)$$

Then, it is possible to write (in each term under the sum $\mathbf{y}_0 = \mathbf{x}$, $\mathbf{y}_{L+1} = \mathbf{x}'$)

$$G(\mathbf{x}, \mathbf{x}') = \sum_{L=0}^{\infty} \frac{(-1)^L C_L}{L!} \int_0^{+\infty} \prod_{n=1}^{L} \frac{de_n}{e_n^{D/2+1}}$$

$$\times \int \prod_{i=1}^{L} d^D \mathbf{y}_i \exp\left\{-\frac{1}{2}\sum_{l=0}^{L}\left[\frac{(\Delta_l \mathbf{y})^2}{e_l} + m^2 e_l\right]\right\}, \qquad (22)$$

where C_L are constants. The enumeration of the links in this 1D case coincides with the enumeration of the vertices: $\Delta_l \mathbf{y} = \mathbf{y}_{l+1} - \mathbf{y}_l$, $l = i$, and in the 1D (open path) case, $L + 1 = V$. If we take the integrals over y's instead of p's, then the conditions are $\Delta_i \mathbf{p} = \mathbf{p}_{i+1} - \mathbf{p}_i = 0$ (for all i) whose continuum limit analogs are $d\mathbf{p} = \partial_\tau \mathbf{p} d\tau = 0$. The solution of the latter on the 1D interval is $\mathbf{p}(t) = $ const. That is the reason why, unlike the 2D case in Eq. (6), in the 1D situation we do not have a nontrivial expression for the Green's function through the $\mathbf{x}_a$'s.

However, the formula in Eq. (22) is in many respects very similar to the 2D expression in Eq. (6). In fact, it contains the summation over all discretizations of the world-trajectory (which are 1D triangulations) and the integration over all 1D distances between the vertices y_i's (which is the integration over the α's). In the 1D case, $\alpha(e) = e$. The summation over the embeddings is given by the integration over all possible positions of the vertices (y's).

5. Thus, we find that the log of the functional integral for the matrix quantum field theory can be represented as the partition function of the first quantized simplicial string theory. In the latter, we sum over all possible embeddings of all possible simplicial complexes into the target space. Instead of the summation over the 2D metrics, we sum over all possible triangu-

lations and invariant 2D distances between the vertices of the simplicial complexes. Both of them seem to be summations over all 2D geometries. At the same time, the action describing embeddings of the simplicial complexes appears to be the discretization of the standard Polyakov action for the relativistic string theory in the flat space [1].

In an attempt to understand the resulting simplicial string theory, we consider the relativistic particle case. Here, we have two *equivalent* expressions: Eqs. (12) and (22). One of them includes integration over all smooth 1D metrics, while the other expression contains, in effect, integration over all singular 1D metrics. Both of them are containing summations over all 1D geometries with the fixed topology (open paths). Note that it is not necessary to take a continuum limit in Eq. (22) to obtain the correct solution to the Klein–Gordon equation. It is not even clear how to take a continuum limit in an expression like Eq. (22). In fact, taking $L = \infty$ does not mean the continuum limit.

Similarly to the 1D case, the 2D expression in Eq. (6) is explicitly reparametrization-invariant and seems to include the summation over all 2D geometries. Then, it is tempting to find a continuum expression exactly equivalent to it containing integration over all smooth metrics. This looks like a crazy idea. At least, there is no good reason why $\lambda^V C(g, V)$ are the appropriate constants for the equality to be true with a suitable measure for the smooth metrics. There is no freedom for the choice of C_L's in Eq. (22).

Frankly speaking, we do not know whether the aforementioned temptation is meaningful or if it is necessary to take a continuum limit, whatever that means. A possible reason for taking a continuum limit may be as follows [12]. In the 1D case, we have a singled out point as the boundary of the world trajectory rather than a curve—continuous sequence of points. Hence, the equation for the path integral following from the variation of the boundary point is just a differential equation. At the same time, the generalization of this differential equation to the 2D case is a loop equation on the boundary curve. Apart from that, there seems to be another risk: the gravitational action after the change from α's to e's can appear to be nonlocal. However, we do not think that this is the case. In fact, the nonlocality, if present, should be rather trivial because the change from α's to e's is local (depends on adjacent triangles) and the measure in Eq. (6) depends on α's locally (it is the product over the triangles). In any case, this question demands a separate investigation.

Anyway, we believe that the choice among the two possibilities can be made after the derivation/understanding of the meaning of the loop equation or its discretized version for the open string theory in Eq. (6).

APPENDIX

Calculations of the Graphs

In this Appendix, we sketch a proof of some combinatorial formulas for the Feynman diagrams, which have a clear meaning within the context of the simplicial string theory. These formulas were proved in [5] using the electric net analogy [15]. Our proof is purely combinatoric and less tedious.

Consider a Feynman diagram in any scalar quantum field theory (with standard interactions polynomial in fields) that has V_E external vertices, V_I internal vertices, and L propagators. The positions of the external vertices are z_a, $a = 1, \ldots,$ and V_E. All propagators are written in the Schwinger α-representation. The expression for this diagram, $I(\mathbf{z}_1, \ldots, \mathbf{z}_{V_E})$, gives a quantum field theory amplitude. We would like to represent the integrand expression under the integration over the α's explicitly in a combinatoric form [5].

To calculate this diagram, let us present the recurrent relation between the graphs [12]. Consider a complete graph (all vertices of which are connected by links to each other) with V vertices. Assign to this graph the following expression:

$$F_V(\{\mathbf{z}_a\}|\{\alpha_{(ab)}\}) = \prod_{a \neq b}^{V} \frac{1}{\alpha_{(ab)}^{D/2}} \exp\left\{-\frac{(\Delta_{(ab)}\mathbf{z})^2}{2\alpha_{(ab)}}\right\}. \quad (23)$$

Let us take the integral, say, over $\mathbf{z}_V$. The result is ($\beta = 1/\alpha$)

$$\int d^D \mathbf{z}_V F_V(\{\mathbf{z}_a\}|\{\beta_{(ab)}^{-1}\})$$

$$= \frac{\left(\prod_{a \neq b}^{V} \beta_{(ab)}\right)^{D/2}}{\left(\prod_{a' \neq b'}^{V-1} \tilde{\beta}_{(a'b')}\right)^{D/2} \left(\sum_{c'=1}^{V-1} \beta_{(c'V)}\right)^{D/2}} F_{V-1}(\{\mathbf{z}_{a'}\}|\{\tilde{\beta}_{(a'b')}^{-1}\}), \quad (24)$$

where

$$\tilde{\beta}_{(a'b')} = \beta_{(a'b')} + \frac{\beta_{(a'V)}\beta_{(Vb')}}{\sum_{c'=1}^{V-1} \beta_{(c'V)}}, \quad (25)$$

$$a', b' = 1, \ldots, V-1.$$

In this way, we can obtain an expression for any graph. In fact, by choosing a big enough V, taking $\beta \longrightarrow 0$ (or $\alpha \longrightarrow \infty$) for the missing links in the graph, and making the appropriate number of the integrations over z's, we can always do this. The resulting expression has a clear combinatoric representation [5]. This expression is easy to see by induction from the presented here formulas. In particular, the resulting expression for the aforementioned Feynman diagram is [5]

$$I(\mathbf{z}_1, \ldots, \mathbf{z}_{V_E}) \propto \int_0^{+\infty} \prod_{l=1}^{L} d\beta_l \beta_l^{D/2-2} \frac{1}{\Delta(\beta)^{D/2}}$$

$$\times \exp\left\{-\sum_{n=1}^{L} \frac{m^2}{2\beta_n} - \frac{P(\beta, \mathbf{z})}{4}\right\}. \quad (26)$$

Here,

$$\Delta(\beta) = \sum_{t_1} \prod^{V_I} \beta,$$

$$P(\beta, \mathbf{z}) = \frac{\sum_{t_2}\left(\prod^{V_I+1} \beta\right)(\Delta_{t_2}\mathbf{z})^2}{\Delta(\beta)}, \quad (27)$$

where, in the first expression, the sum goes over all so-called dual-trees t_1 of the diagram, while, in the second expression, the sum goes over all dual-2-trees t_2 of the diagram. In these expressions, we take products of β's along the corresponding dual-co-trees and dual-co-2-trees correspondingly; $\Delta_{t_2}\mathbf{z}$ is the difference of the positions of the two external vertices that come together in a dual-2-tree t_2.

The definition of all these "dual-(co)-(2)-trees" is as follows [5]. The tree graph (not necessary connected) obtained by shrinking V_I lines of the diagram such that all V_I internal vertices merge with the external vertices, but that no pair of external vertices becomes coincident, is called a dual-tree, and the set of V_I shrunk lines, a dual-co-tree. If we shrink $V_I + 1$ lines, so that not only all the internal vertices merge with the external ones, but also exactly two external vertices come together, then the resulting graph is a dual-2-tree and the set of $V_I + 1$ shrunk lines, a dual-co-2-tree.

The reason why we present these formulas here is the following. The same kind of formulas can be written for the dual graph to a Feynman diagram. For the

dual graph, such an amplitude has the meaning of either a scattering amplitude of closed strings or an open string amplitude. Hence, for this dual graph, $\Delta(\beta)$ and $P(\beta, \mathbf{z})$ are related to the determinant of the discretized 2D Laplacian (in curved metric) and 2D classical action (with the boundary conditions given by z's) correspondingly [12]. But this is a theme for a separate scientific investigation.

REFERENCES

1. A. M. Polyakov, *Gauge Fields and Strings* (Harwood Academic, Chur, Switzerland, 1987).

2. J. M. Maldacena, Adv. Theor. Math. Phys. **2**, 231 (1998) [Int. J. Theor. Phys. **38**, 1113 (1999)]; hep-th/9711200; S. S. Gubser, I. R. Klebanov, and A. M. Polyakov, Phys. Lett. B **428**, 105 (1998); hep-th/9802109; E. Witten, Adv. Theor. Math. Phys. **2**, 253 (1998).

3. E. T. Akhmedov, Usp. Fiz. Nauk **171**, 1005 (2001) [Phys. Usp. **44**, 955 (2001)]; hep-th/9911095.

4. R. Gopakumar, hep-th/0308184; hep-th/0402063.

5. C. S. Lam and J. P. Lebrun, Nuovo Cimento A **4**, 397 (1969); See as well N. N. Bogolyubov and D. V. Shirkov, *Introduction to the Theory of Quantized Fields*, 3rd ed. (Nauka, Moscow, 1973; Wiley, New York, 1980).

6. J. D. Bjorken and S. D. Drell, *Relativistic Quantum Fields* (McGraw-Hill, New York, 1965; Nauka, Moscow, 1978).

7. J. t'Hooft, Nucl. Phys. B **72**, 461 (1974).

8. A. Alexandrov, A. Mironov, and A. Morozov, hep-th/0310113.

9. C. Kristjansen, J. Plefka, G. W. Semenoff, and M. Staudacher, Nucl. Phys. B **643**, 3 (2002); hep-th/0205033.

10. T. L. Ivanenko and M. I. Polikarpov, Nucl. Phys. (Proc. Suppl.) **26**, 536 (1992); M. N. Chernodub and M. I. Polikarpov, hep-th/9710205.

11. A. P. Isaev, Nucl. Phys. B **662**, 461 (2003); hep-th/0303056.

12. E. T. Akhmedov and V. V. Dolotin (in press).

13. F. David, hep-th/9303127; J. Ambjorn, M. Carfora, and A. Marzuoli, hep-th/9612069; H. W. Hamber and R. M. Wiliams, hep-th/9607153.

14. E. T. Akhmedov, Phys. Lett. B **442**, 152 (1998); hep-th/9806217; hep-th/0202055.

15. J. D. Bjorken, Doctoral Thesis (Stanford, 1958).

Vector Meson Electroproduction at Next-to-Leading Order[¶]

D. Yu. Ivanov[1], L. Szymanowski[2, 3], and G. Krasnikov[4]

[1] *Sobolev Institute of Mathematics, Russian Academy of Sciences, Novosibirsk, 630090 Russia*
e-mail: d-ivanov@math.nsc.ru
[2] *Soltan Institute for Nuclear Studies, 00-681 Warsaw, Poland*
[3] *LPT, Université Paris-Sud, 91405 Orsay, France**
[4] *Department of Theoretical Physics, St. Petersburg State University, St. Petersburg, 198904 Russia*
Received May 20, 2004; in final form, July 8, 2004

The process of light neutral vector meson electroproduction is studied in the framework of QCD factorization in which the amplitude factorizes in a convolution of the nonperturbative meson distribution amplitude and generalized parton densities with perturbatively calculable hard-scattering amplitudes. We derive a complete set of hard-scattering amplitudes at next-to-leading order (NLO) for the production of vector mesons, $V = \rho^0$, ω, ϕ. © 2004 MAIK "Nauka/Interperiodica".

PACS numbers: 12.38.Bx; 13.60.Le

1. The process of elastic neutral vector meson electroproduction on a nucleon,

$$\gamma^*(q)N(p) \longrightarrow V(q')N(p'), \quad V = \rho^0, \omega, \phi, \quad (1)$$

was studied in fix target and in HERA collider experiments. The primary motivation for the strong interest in this process (and in the similar process of heavy quarkonium production) is that it can potentially serve to constrain gluon density in a nucleon [1, 2]. On the theoretical side, the large negative virtuality of the photon, $q^2 = -Q^2$, provides a hard scale for the process that justifies the application of QCD factorization methods that allow separation of the contributions to the amplitude coming from different scales. The factorization theorem [3] states that, in a scaling limit, with $Q^2 \longrightarrow \infty$ and $x_{Bj} = Q^2/2(pq)$ fixed, a vector meson is produced in a longitudinally polarized state by the longitudinally polarized photon and that the amplitude of process (1) is given by a convolution of the nonperturbative meson distribution amplitude (DA) and the generalized parton densities (GPDs) with the perturbatively calculable hard-scattering amplitudes. In this contribution, we present the results of our calculation of the hard-scattering amplitudes at NLO.

2. $p^2 = p'^2 = m_N^2$ and $q'^2 = m_M^2$, where m_N and m_M are a proton mass and a meson mass, respectively. The invariant c.m. energy $s_{\gamma^*p} = (q + p)^2 = W^2$. We define

$$\Delta = p' - p, \quad P = \frac{p + p'}{2}, \quad t = \Delta^2,$$

$$(q - \Delta)^2 = m_M^2, \quad x_{Bj} = \frac{Q^2}{W^2 + Q^2}. \quad (2)$$

We introduce two light-cone vectors,

$$n_+^2 = n_-^2 = 0, \quad n_+ n_- = 1. \quad (3)$$

Any vector a is decomposed as

$$a^\mu = a^+ n_+^\mu + a^- n_-^\mu + a_\perp, \quad a^2 = 2a^+ a^- - \mathbf{a}^2. \quad (4)$$

We choose the light-cone vectors in such a way that

$$p = (1 + \xi)W n_+ + \frac{m_N^2}{2(1 + \xi)W} n_-,$$

$$p' = (1 - \xi)W n_+ + \frac{(m_N^2 + \mathbf{\Delta}^2)}{2(1 - \xi)W} n_- + \Delta_\perp. \quad (5)$$

We are interested in a kinematic region where the invariant transferred momentum, t, is small, much smaller than Q^2. In the scaling limit, variable ξ, which parametrizes the plus component of the momentum transfer, equals $\xi = x_{Bj}/(2 - x_{Bj})$.

GPDs are defined as the matrix element of the light-cone quark and gluon operators [4]:

$$F^q(x, \xi, t)$$

$$= \frac{1}{2} \int \frac{d\lambda}{2\pi} e^{ix(Pz)} \langle p'|\bar{q}\left(-\frac{z}{2}\right)\not{n}_- q\left(\frac{z}{2}\right)|p\rangle|_{z = \lambda n_-}$$

$$= \frac{1}{2(Pn_-)}[\mathcal{H}^q(x, \xi, t)\bar{u}(p')\not{n}_- u(p) \quad (6)$$

$$+ \mathcal{E}^q(x, \xi, t)\bar{u}(p')\frac{i\sigma^{\alpha\beta}n_{-\alpha}\Delta_\beta}{2m_N}u(p)\Bigg],$$

$$F^g(x, \xi, t) = \frac{1}{(Pn_-)}\int\frac{d\lambda}{2\pi}e^{ix(Pz)}n_{-\alpha}n_{-\beta}$$

$$\times\langle p'|G^{\alpha\mu}\left(-\frac{z}{2}\right)G_\mu^\beta\left(\frac{z}{2}\right)|p\rangle|_{z=\lambda n_-}$$

$$= \frac{1}{2(Pn_-)}[\mathcal{H}^g(x, \xi, t)\bar{u}(p')\not{n}_-u(p)$$ (7)

$$+ \mathcal{E}^g(x, \xi, t)\bar{u}(p')\frac{i\sigma^{\alpha\beta}n_{-\alpha}\Delta_\beta}{2m_N}u(p)\Bigg].$$

In both cases, the insertion of the path-ordered gauge factor between the field operators is implied. Momentum fraction x, $-1 \leq x \leq 1$, parametrizes parton momenta with respect to the symmetric momentum $P = (p + p')/2$. In the forward limit, $p' = p$, the contributions proportional to the functions $\mathcal{E}^q(x, \xi, t)$ and $\mathcal{E}^g(x, \xi, t)$ vanish, and the distributions $\mathcal{H}^q(x, \xi, t)$ and $\mathcal{H}^g(x, \xi, t)$ reduce to ordinary quark and gluon densities:

$$\mathcal{H}^q(x, 0, 0) = q(x) \text{ for } x > 0,$$

$$\mathcal{H}^q(x, 0, 0) = -\bar{q}(-x) \text{ for } x < 0,$$ (8)

$$\mathcal{H}^g(x, 0, 0) = xg(x) \text{ for } x > 0.$$

Note that gluon GPD is a function of x, $\mathcal{H}^g(x, \xi, t) = \mathcal{H}^g(-x, \xi, t)$.

The meson DA $\phi_V(z)$ is defined by the following relation:

$$\langle 0|\bar{q}(y)\gamma_\mu q(-y)|V_L(p)\rangle_{y^2 \to 0}$$

$$= p_\mu f_V\int_0^1 dz e^{i(2z-1)(py)}\phi_V(z).$$ (9)

It is normalized to unity $\int_0^1 \phi_V(z)dz = 1$. Here, z is a light-cone fraction of a quark, f_V is a meson dimensional coupling constant known from $V \longrightarrow e^+e^-$ decay, in particular, $f_\rho = 198 \pm 7$ MeV:

$$\mathcal{M}_{\gamma_L^* N \to V_L N} = \frac{2\pi\sqrt{4\pi\alpha}f_V}{N_c Q\xi}\int_0^1 dz\phi_V(z)\int_{-1}^1 dx$$

$$\times\Bigg[Q_V(T_g(z, x)F^g(x, \xi, t) + T_{(+)}(z, x)F^{(+)}(x, \xi, t))$$ (10)

$$+ \sum_q e_q^V T_q(z, x)F^{q(+)}(x, \xi, t)\Bigg].$$

Here, the dependence of the GPDs, DA, and the hard-scattering amplitudes on factorization scale μ_F is suppressed for shortness. Since we are considering the leading helicity nonflip amplitude, in Eq. (10), the hard-scattering amplitudes do not depend on t. The account of this dependence would lead to the power suppressed, $\sim t/Q$, contribution.[1] α is a fine structure constant, and $N_c = 3$ is the number of QCD colors. Q_V depends on the meson flavor content. If one assumes that it is $\frac{1}{\sqrt{2}}(|u\bar{u}\rangle - |d\bar{d}\rangle)$, $\frac{1}{\sqrt{2}}(|u\bar{u}\rangle + |d\bar{d}\rangle)$, and $|s\bar{s}\rangle$ for ρ, ω, and ϕ, respectively, than $Q_\rho = 1/\sqrt{2}$, $Q_\omega = 1/3\sqrt{2}$, and $Q_\phi = -1/3$, the sum in the last term of (10) runs over $q = u, d$ for $V = \rho, \omega$ and $q = s$ for $V = \phi$ and

$$e_u^\rho = e_u^\omega = \frac{2}{3\sqrt{2}}, \quad e_d^\rho = -e_d^\omega = \frac{1}{3\sqrt{2}}, \quad e_s^\phi = \frac{-1}{3};$$

$F^{q(+)}(x, \xi, t) = F^q(x, \xi, t) - F^q(-x, \xi, t)$ denotes a singlet quark GPD, $F^{(+)}(x, \xi, t) = \sum_{q=u,d,s}F^{q(+)}(x, \xi, t)$ stands for the sum of all light flavors.

Due to odd C-parity of a vector meson, $\phi_V(z) = \phi_V(1 - z)$. Moreover, since V and γ^* have the same C-parities, the $\gamma^* \longrightarrow V$ transition selects the C-even gluon and singlet quark contributions, whereas the C-odd quark combination $F^{q(-)}(x, \xi, t) = F^q(x, \xi, t) + F^q(-x, \xi, t)$ decouples in (10).

3. Below, we present the results of our calculation of the hard-scattering amplitudes in the $\overline{\text{MS}}$ scheme.

$T_q(z, x)$ may be obtained by the following substitution from the known results for a pion EM formfactor (see also [8]):

$$T_q(z, x)$$

$$= \left\{T\left(z, \frac{x+\xi}{2\xi} - i\epsilon\right) - T\left(\bar{z}, \frac{\xi-x}{2\xi} - i\epsilon\right)\right\} + \{z \longrightarrow \bar{z}\},$$ (11)

$$T(v, u) = \frac{\alpha_S(\mu_R^2)C_F}{4vu}\left(1 + \frac{\alpha_S(\mu_R^2)}{4\pi}\right.$$

$$\times\left[c_1\left(2[3 + \ln(vu)]\ln\left(\frac{Q^2}{\mu_F^2}\right) + \ln^2(vu)\right.\right.$$

$$+ 6\ln(vu) - \frac{\ln(v)}{\bar{v}} - \frac{\ln(u)}{\bar{u}} - \frac{28}{3}\right)$$

$$\left.\left.+ \beta_0\left(\frac{5}{3} - \ln(vu) - \ln\left(\frac{Q^2}{\mu_R^2}\right)\right)\right)\right)$$

---

[1] For the analysis of other helicity amplitudes, see [5–7].

$$+ c_2 \left(2 \frac{(\bar{v} v^2 + \bar{u} u^2)}{(v - u)^3} [Li_2(\bar{u}) - Li_2(\bar{v}) + Li_2(v) \quad (12)$$

$$- Li_2(u) + \ln(\bar{v}) \ln(u) - \ln(\bar{u}) \ln(v)]$$

$$+ 2 \frac{(v + u - 2vu) \ln \bar{v} \bar{u}}{(v - u)^2} + 2[Li_2(\bar{u}) + Li_2(\bar{v})$$

$$- Li_2(u) - Li_2(v) + \ln(\bar{v}) \ln(u) + \ln(\bar{u}) \ln(v)]$$

$$+ 4 \frac{vu \ln(vu)}{(v - u)^2} - 4 \ln(\bar{v}) \ln(\bar{u}) - \frac{20}{3} \Big) \Big] \Big).$$

Here and below, we use the shorthand notation $\bar{u} = 1 - u$ for any light-cone fraction. μ_R is a renormalization scale for a strong coupling, $\beta_0 = 11 N_c/3 - 2 n_f/3$, n_f is the effective number of quark flavors, and

$$C_F = \frac{N_c^2 - 1}{2 N_c}, \quad Li_2(z) = - \int_0^z \frac{dt}{t} \ln(1 - t).$$

Also, we denote

$$c_1 = C_F, \quad c_2 = C_F - \frac{C_A}{2} = - \frac{1}{2 N_c}; \quad (13)$$

$T_{(+)}(z, x)$ starts from NLO

$$T_{(+)}(z, x) = \frac{\alpha_S^2(\mu_R^2) C_F}{(8\pi) z \bar{z}} \mathcal{I}_q \left(z, \frac{x - \xi}{2\xi} + i\epsilon \right). \quad (14)$$

Here,

$$\mathcal{I}_q(z, y) = \left\{ \frac{2y + 1}{y(y + 1)} \left[\frac{y}{2} \ln^2(-y) - \frac{y + 1}{2} \ln^2(y + 1) \right. \right.$$

$$+ \left(\ln \left(\frac{Q^2 z}{\mu_F^2} \right) - 1 \right) (y \ln(-y) - (y + 1) \ln(y + 1)) \Big]$$

$$+ \frac{y \ln(-y) + (y + 1) \ln(y + 1)}{y(y + 1)} - \frac{R(z, y)}{y + z}$$

$$+ \frac{y(y + 1) + (y + z)^2}{(y + z)^2} H(z, y) \Big\} + \{ z \longrightarrow \bar{z} \},$$

(15)

where we introduced two auxiliary functions,

$$R(z, y) = z \ln(-y) + \bar{z} \ln(y + 1) + z \ln(z) + \bar{z} \ln(\bar{z}), (16)$$

$$H(z, y) = Li_2(y + 1) - Li_2(-y) + Li_2(z) - Li_2(\bar{z})$$
$$+ \ln(-y) \ln(\bar{z}) - \ln(y + 1) \ln(z). \quad (17)$$

For the gluonic contribution, we obtain

$$T_g(z, x) = \frac{\alpha_S(\mu_R^2) \xi}{z \bar{z} (x + \xi - i\epsilon)(x - \xi + i\epsilon)}$$

$$\times \left[1 + \frac{\alpha_S(\mu_R^2)}{4\pi} \mathcal{I}_g \left(z, \frac{x - \xi}{2\xi} + i\epsilon \right) \right],$$

(18)

where

$$\mathcal{I}_g(z, y) = \left\{ \left(\ln \left(\frac{Q^2}{\mu_F^2} \right) - 1 \right) \left[c_1 \left(\frac{3}{2} + 2 z \ln(\bar{z}) \right) \right. \right.$$

$$+ \frac{\beta_0}{2} - \frac{2(c_1 - c_2)(y^2 + (y + 1)^2)}{y(y + 1)} ((y + 1) \ln(y + 1)$$

$$- y \ln(-y)) + \frac{c_1}{2} \left(\frac{y \ln(-y)}{y + 1} + \frac{(y + 1) \ln(y + 1)}{y} \right) \Big]$$

$$- \frac{\beta_0}{2} \left(\ln \left(\frac{Q^2}{\mu_R^2} \right) - 1 \right) - \frac{c_1 (2y + 1) R(z, y)}{2(y + z)} - 2 c_1$$

$$- \frac{(3 c_1 - 4 c_2)}{4} \left(\frac{y \ln^2(-y)}{y + 1} + \frac{(y + 1) \ln^2(y + 1)}{y} \right)$$

$$+ (\ln(-y) + \ln(y + 1)) \left[c_1 \left(\bar{z} \ln(z) - \frac{1}{4} \right) + 2 c_2 \right]$$

(19)

$$+ c_1 (1 + 3z) \ln(\bar{z}) - (c_1 - c_2)(\ln(z \bar{z}) - 2) \left[\frac{y \ln(-y)}{y + 1} \right.$$

$$\left. + \frac{(y + 1) \ln(y + 1)}{y} \right] + (c_1 - c_2)(2y + 1) \ln \left(\frac{-y}{y + 1} \right)$$

$$\times \left[\frac{3}{2} + \ln(z \bar{z}) + \ln(-y) + \ln(y + 1) \right] + c_1 z \ln^2(\bar{z})$$

$$+ (c_1 (y(y + 1) + (y + z)^2) - c_2 (2y + 1)(y + z))$$

$$\times \left[- \frac{R(z, y)}{(y + z)^2} + \frac{\ln(-y) - \ln(y + 1) + \ln(z) - \ln(\bar{z})}{2(y + z)} \right.$$

$$\left. + \frac{y(y + 1) + (y + z)^2}{(y + z)^3} H(z, y) \right] \Big\} + \{ z \longrightarrow \bar{z} \}.$$

4. The above formulas and the known NLO evolution equations describing μ_F dependence of the GPDs and meson DA give a complete basis for description of a neutral vector meson electroproduction with NLO accuracy. At the leading order, we reproduce the known result [9]; our results for the NLO hard-scattering amplitudes are new.

At high energies, $W^2 \gg Q^2$ and the imaginary part of the amplitude dominates. The leading contribution to the NLO correction comes from the integration region $\xi \ll |x| \ll 1$. By simplifying the gluon hard-scattering amplitude in this limit, we obtain the estimate

$$\mathcal{M}_{\gamma_L^* N \to V_L N} \approx \frac{-2i\pi^2 \sqrt{4\pi\alpha}\, \alpha_S f_V Q_V}{N_c Q \xi} \int_0^1 \frac{dz \phi_V(z)}{z\bar{z}}$$

$$\times \left[F^g(\xi, \xi, t) + \frac{\alpha_S N_c}{\pi} \ln\left(\frac{Q^2 z\bar{z}}{\mu_F^2}\right) \int_\xi^1 \frac{dx}{x} F^g(x, \xi, t) \right]. \tag{20}$$

Given the behavior of the gluon GPD at small x, $F^g(x, \xi, t) \sim$ const, we see that NLO correction is parametrically large, $\sim \ln(1/\xi)$, and negative unless one chooses a value of the factorization scale sufficiently lower than the kinematic scale. For the asymptotic form of meson DA, $\phi_V^{as}(z) = 6z\bar{z}$, the last term in (20) changes its sign at $\mu_F = Q/e$; for the DA with a broader shape, this happens at even lower values of μ_F.

It is interesting to note that the value $\mu_F^2 = Q^2/e^2$ is rather close to an estimate in the dipole approach [10] of a typical inverse dipole size [11, 12], $1/r^2 \sim \mu_F^2 = 0.15Q^2$, for vector meson electroproduction in the HERA kinematic region. We believe that a study of relationship between the collinear factorization and the dipole approach at the NLO level would be very important. But this question, as well as the resummation of contributions that are large at high energies, $\sim(\alpha_S \ln(1/\xi))^n$, both to the hard-scattering amplitudes and to the evolution of GPDs goes beyond the scope of the present work.

5. As an example of our results, we compare one point for the longitudinal cross section reported by the ZEUS Collaboration [13], e.g., $d\sigma_L/dt|_{t=0} = 17 \pm 4$ nb/GeV^2 at $Q^2 = 27$ GeV^2, $W = 110$ GeV, with our predictions. In Fig. 1, we plot the dependence of the predicted $d\sigma_L/dt|_{t=0}(\mu_F, \mu_R)$ on factorization scale μ_F for two choices of the renormalization scale: $\mu_R = \mu_F$ (the solid curves) and $\mu_R = Q/\sqrt{e}$, i.e., the BLM (Brodsky–Lepage–McKenzie) prescription (the dashed curves). The data point is described in this plot by the black horizontal line. In this numerical analysis, we use two models of the NLO generalized parton distributions of [14], the first one based on MRST2001 forward distribution (curves a, c) and the second one on CTEQ6M (curves b, d). Moreover, we take the NLO strong coupling constant α_s and the asymptotic meson DA.[2] Figure 1 shows that the BLM prescription leads to

---

[2] QCD sum rules studies [15] show that, at a low scale, the shape of vector meson DA is close to asymptotic. At $\mu_F \longrightarrow \infty$, any DA approaches its limit—asymptotic DA. Due to this, we use an asymptotic DA and postpone the study of dependence on DA shape for future analysis.
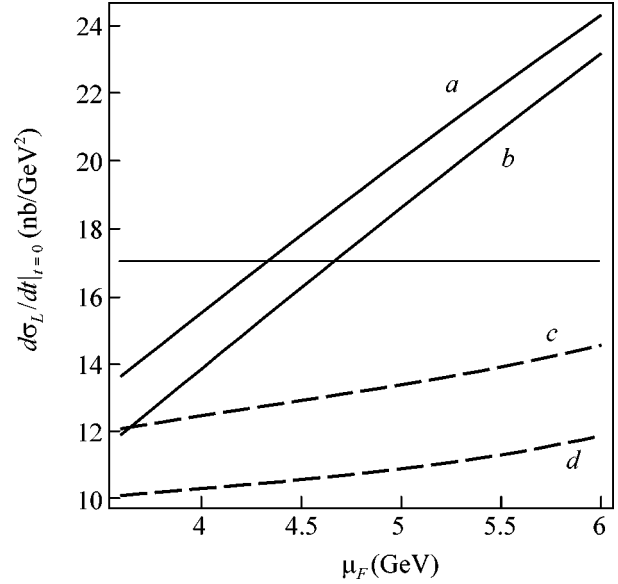
Fig. 1. Factorization scale dependence of predicted $d\sigma_L/dt|_{t=0}$ at $Q^2 = 27$ GeV^2, $W = 110$ GeV. The horizontal black line describes the data point. Solid curves assume $\mu_R = \mu_F$; dashed curves, the BLM prescription. The curves a and c (b and d) are obtained with the use of MRST2001 (CTEQ6M).

a smaller cross section and much flatter behavior of the cross section on μ_F than for the choice $\mu_R = \mu_F$. We also observe a substantial uncertainty of our predictions that is due to the input parton GPDs.

Since, as mentioned above, the NLO corrections are large, it is instructive to study the relative magnitudes of different contributions to amplitude (10). This is done by assuming $\mu_R = \mu_F$ and for CTEQ6M GPD. In Fig. 2, we show plots of Im$\mathcal{M}$ and Re$\mathcal{M}$ as functions of μ_F corresponding to gluonic and quark Born parts of amplitude (10) (denoted as gB and qB, respectively), to the NLO part of the gluonic contribution T_g (gN), to the NLO part of the quark contribution T_q (qN), to the quark contribution $T_{(+)}$ (q^+), and to the full amplitude (10) (denoted as full). All these separate contributions are normalized by $|\mathcal{M}|$ of (10) with all terms taken into account. Let us note that, as expected for a small x process, the imaginary part of amplitude (10) dominates over its real part. We observe that the NLO corrections are mostly of opposite signs than in the corresponding Born terms are large; consequently, the final values of amplitude (10) are the result of strong cancellations between Born parts and NLO terms. Without account being taken of NLO terms, the predictions would be substantially above the data. These results are similar to ones obtained recently for Υ photoproduction [16].

In this paper, we restrict our analysis to the leading twist and neglect completely the power suppressed, $\sim 1/Q$, and the contributions. This is definitely legitimate for sufficiently large Q. Most probably, at the
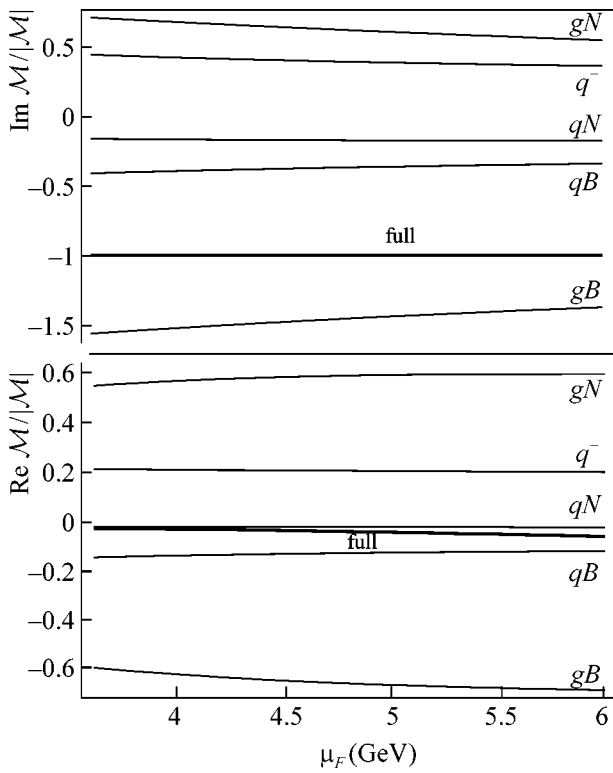
Fig. 2. Different contributions to Im $\mathcal{M}/|\mathcal{M}|$ and Re $\mathcal{M}/|\mathcal{M}|$ in dependence on μ_F (for $\mu_R = \mu_F$ and CTEQ6M): gB, Born term of T_g; qB, Born term of T_q; gN, NLO terms of T_g; qN, NLO terms of T_q; q^+, $T_{(+)}$; full, all terms of (10) included.

HERA energies and $Q^2 \sim 20\,\mathrm{GeV}^2$, the higher-twist corrections are still large (see, e.g., [11, 12] based on [17]). Nevertheless, we want to stress that our leading-twist results obtained with NLO hard-scattering amplitudes and NLO GPDs [14] (which were adjusted to describe HERA deeply virtual Compton scattering data) are in qualitative agreement with the ρ meson electroproduction cross section measured at HERA.

REFERENCES

1. M. G. Ryskin, Z. Phys. C **57**, 89 (1993).
2. S. J. Brodsky *et al.*, Phys. Rev. D **50**, 3134 (1994).
3. J. C. Collins, L. Frankfurt, and M. Strikman, Phys. Rev. D **56**, 2982 (1997).
4. M. Diehl, Phys. Rep. **388**, 41 (2003).
5. A. D. Martin, M. G. Ryskin, and T. Teubner, Phys. Rev. D **55**, 4329 (1997).
6. D. Yu. Ivanov and R. Kirschner, Phys. Rev. D **58**, 114026 (1998).
7. E. V. Kuraev, N. N. Nikolaev, and B. G. Zakharov, Pis'ma Zh. Éksp. Teor. Fiz. **68**, 667 (1998) [JETP Lett. **68**, 696 (1998)].
8. A. V. Belitsky and D. Muller, Phys. Lett. B **513**, 349 (2001).
9. L. Mankiewicz, G. Piller, and T. Weigl, Eur. Phys. J. C **5**, 119 (1998).
10. N. N. Nikolaev and B. G. Zakharov, Z. Phys. C **49**, 607 (1991).
11. J. Nemchik, N. N. Nikolaev, and B. G. Zakharov, Phys. Lett. B **341**, 228 (1994).
12. J. Nemchik, N. N. Nikolaev, E. Predazzi, and B. G. Zakharov, Z. Phys. C **75**, 71 (1997).
13. J. Breitweg *et al.* (ZEUS Collab.), Eur. Phys. J. C **6**, 603 (1999).
14. A. Freund, M. McDermott, and M. Strikman, Phys. Rev. D **67**, 036001 (2003).
15. P. Ball, V. M. Braun, Y. Koike, and K. Tanaka, Nucl. Phys. B **529**, 323 (1998).
16. D. Yu. Ivanov, A. Schäfer, L. Szymanowski, and G. Krasnikov, Eur. Phys. J. C **34**, 297 (2004).
17. E. V. Shuryak, Rev. Mod. Phys. **65**, 1 (1993).

Synchronization and Bifurcations of Internal and External Degrees of Freedom of an Atom in a Standing Light Wave

V. Yu. Argonov and S. V. Prants*

Il'ichev Pacific Oceanological Institute, Far East Division, Russian Academy of Sciences, Vladivostok, 690041 Russia
* e-mail: prants@poi.dvo.ru

The nonlinear dynamical effects of synchronization and bifurcations of Rabi oscillations and oscillations of the center of mass of an atom moving in the field of a standing light wave are theoretically and numerically examined. After completion of a transient process, synchronized oscillations, stable with respect to small noise, are established both upon ballistic motion of the atom and upon its oscillations in the optical potential well. The bifurcations of limit cycle generation with different periods (tripling of the period is most pronounced) and the passage to a chaotic strange attractor through an intermittency are obtained. © 2004 MAIK "Nauka/Interperiodica".

PACS numbers: 42.50.Ct; 05.45.-a; 42.50.Vk

1. Equations of motion. Advances in manipulating quantum systems for the purposes of their use in quantum calculations, data processing, and examination of the basic principles of quantum physics are difficult to overestimate. Intensive work in this field is carried out with atoms in high-Q cavities (see review [1]). Consider a two-level atom interacting with a selected mode in the form of a standing wave of a Fabry–Perot cavity. The standard Hamiltonian of cavity quantum electrodynamics [2]

$$\hat{H}_0 = \frac{\hat{p}^2}{2m_a} + \frac{1}{2}\hbar\omega_a\hat{\sigma}_z + \hbar\omega_f\left(\hat{a}^\dagger\hat{a} + \frac{1}{2}\right)$$
$$- \hbar\Omega_0\cos(k_f\hat{x})(\hat{a}^\dagger\hat{\sigma}_- + \hat{a}\hat{\sigma}_+) \tag{1}$$

describes, respectively, the atomic kinetic and internal energies, the mode energy, and the energy of the atom–field interaction, which depends on the atomic position in the cavity. The interaction between the intraatomic, translational, and field degrees of freedom gives rise to a complex dynamics of the atom–field system. Apart from the well-known and experimentally observed effects of the collapse and revival of Rabi oscillations, squeezed-light generation, atom cooling and trapping, etc. (see [1, 3–6]), dynamical chaos [7], Lévi flights [8, 9], and atomic fractals [9, 10] have recently been found theoretically and numerically in strongly coupled atom–field system (1). These manifestations of local instability were found and investigated within the framework of Hamiltonian dynamics, where the spontaneous relaxation and photon leakage from the cavity can be neglected on the characteristic time scale of Rabi oscillations.

In this work, we study the dissipative dynamics of an atom in the field of a standing light wave of a Fabry–Perot cavity with laser pumping and report the detection of new nonlinear dynamical effects: synchronization of internal and external atomic degrees of freedom, limit cycles of different periods, bifurcations of limit cycles, and chaotic strange attractors. The action of the external laser field is described by the Hamiltonian $\hat{H}_1 = \hbar E_0\hat{a}\exp i(\omega_l t - \phi) + $ h.c. In the semiclassical approximation (valid for strong fields and atomic momenta exceeding photon momentum $\hbar k_f$), it is easy to obtain a closed system of equations for the average values of atomic and field operators. In a rotating frame and with addition of the phenomenological dissipative terms, this system takes the form

$$\dot{\xi} = \alpha p, \quad \dot{p} = (1/2)(gy - ex)\sin\xi,$$
$$\dot{e} = y\cos\xi - 2\gamma_f e + 2E\sin(\Delta\tau + \phi),$$
$$\dot{g} = x\cos\xi - 2\gamma_f g - 2E\cos(\Delta\tau + \phi),$$
$$\dot{x} = \delta y + zg\cos\xi - (1/2)\gamma_a x,$$
$$\dot{y} = -\delta x + ze\cos\xi - (1/2)\gamma_a y,$$
$$\dot{z} = -(gx + ey)\cos\xi - \gamma_a(z + 1). \tag{2}$$

Here, $\xi \equiv k_f\langle\hat{x}\rangle$ and $p \equiv \langle\hat{p}\rangle/\hbar k_f$ are, respectively, the normalized atomic coordinate and momentum; $e \equiv \langle\hat{a}^\dagger\exp(-i\omega_f t) + \hat{a}\exp(i\omega_f t)\rangle$ and $g \equiv i\langle\hat{a}^\dagger\exp(-i\omega_f t) - \hat{a}\exp(i\omega_f t)\rangle$ are the field variables; and $x \equiv \langle\hat{\sigma}_+\exp(-i\omega_f t) + \hat{\sigma}_-\exp(i\omega_f t)\rangle$, $y \equiv i\langle\hat{\sigma}_-\exp(i\omega_f t) - \hat{\sigma}_+\exp(-i\omega_f t)\rangle$, and $z \equiv \langle\hat{\sigma}_z\rangle$ are the Bloch atomic variables. The time τ and the spontaneous relaxation rates of the atom γ_a and the field mode γ_f are normalized to the vacuum Rabi frequency Ω_0; $\Delta \equiv (\omega_f - \omega_l)/\Omega_0$ is the
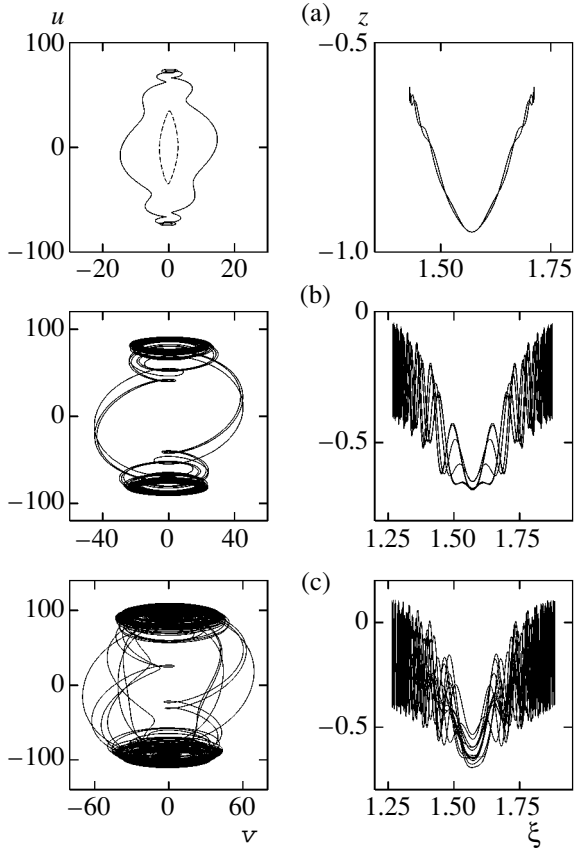
Fig. 1. Attractors in a dynamical system: (a) the limit cycles of period 1 (the dashed line corresponds to $n = 3000$ and the solid line is for $n = 10000$); (b) the limit cycle of period 3 ($n = 14846$); and (c) the chaotic strange attractor ($n = 24000$). $\delta = 24$ everywhere.

external detuning. The detuning $\delta \equiv (\omega_f - \omega_a)/\Omega_0$ of the atom–field resonance, the pump amplitude $E \equiv E_0/\Omega_0$, and the atomic recoil frequency $\alpha \equiv \hbar k_f^2/m_a\Omega_0$ upon photon emission are the essential controlling parameters of the system. The analysis of nonautonomous nonlinear dynamical system (2) with four degrees of freedom presents great difficulties. Here, we restrict ourselves to the case of zero external detuning $\Delta = 0$, $\phi = \pi/4$, and a strong field. If the mean number of photons in the mode $n = (e^2 + g^2)/4 \simeq (E/2\gamma_f)^2$ is large enough, the field variables e and g are virtually constant. Then, it is convenient to rewrite reduced system (2) in a form that ensures the possibility of comparing with the Hamiltonian version [2, 9]:

$$\dot{\xi} = \alpha p, \quad \dot{p} = -u\sin\xi,$$

$$\dot{u} = \delta v - (1/2)\gamma_a u,$$

$$\dot{v} = -\delta u + 2nz\cos\xi - (1/2)\gamma_a v, \qquad (3)$$

$$\dot{z} = -2v\cos\xi - \gamma_a(z + 1),$$

where $u \equiv (ex - gy)/2 = \sqrt{n/2}\,(x + y)$ and $v \equiv (gx + ey)/2 = \sqrt{n/2}\,(y - x)$ have the simple meaning of variables proportional to the quadrature components of the atomic dipole moment.

2. Synchronization. By synchronization is meant the stationary multiple ratio between the frequencies of Rabi oscillations and atomic momentum. Note that the oscillation frequency $\sqrt{\delta^2 + 4n}$ of a quiescent atom in a strong field and the frequency $\alpha^{1/2}n^{1/4}$ of small-amplitude oscillations of the atomic center of mass in a well can differ by several orders of magnitude. The mechanical oscillator imposes its own rhythm on the Rabi oscillator both in the case of ballistic motion of the atom and upon atomic oscillations in the field of the optical potential $\Pi(\xi, \tau) = \int u \sin\xi d\xi$. The synchronization manifests itself in establishing a limit cycle in the phase space. The cycle of a period k means that motion periodicity is observed for $2k$ intersections of the same (oscillations in the well) or different (atomic flight) nodes of the standing wave. For an atom in a well, the projections of the limit cycles of periods 1 and 3 on the planes (u, v) and (z, ξ) for $\delta = 24$ are shown in Figs. 1a and 1b. Hereafter, we set $\alpha = 0.01$, $\gamma_a = 0.3$, and the initial momentum $p_0 = 60$ in all numerical calculations. The cycle size and shape are determined by the oscillation amplitude and oscillation spectrum, respectively. The greater the nonlinearity parameter n, the more the cycle shape differs from a harmonic shape. At the left of Fig. 1a, two phase trajectories corresponding to $n = 3000$ (dashed line) and $n = 10000$ (solid line) are shown. It is obvious that the second limit cycle strongly differs from the harmonic cycle.

The time τ_c of establishing limit cycles is mainly determined by the action of the friction force $-\bar{p}$, which decelerates (or accelerates) an atom during the time τ_c until its momentum achieves some quasi-stationary value $\bar{p}$ (in the literature on the mechanical action of light on atoms, this process is referred to as velocity grouping effect, and the corresponding momentum is referred to as grouping momentum [3]). For atoms whose momenta are initially close to $\bar{p}$, this time can be estimated, except for a constant, as $\tau_c \propto (\partial\dot{p}/\partial\alpha p)^{-1} \propto \delta/n$. Depending on the parameters and initial momentum, the average momentum $\bar{p}$ established with time can be both zero ($\delta > 0$; the atom is trapped and oscillates in the optical potential well) and nonzero ($\delta < 0$; ballistic motion through the cavity with velocity modulation). In the synchronization regime, a limit cycle is established in the atom dynamics; the cycle frequency is determined by the oscillation frequency of an instantaneous momentum p about the steady-state mean value $\bar{p}$. At $\delta > 0$ and a sufficiently large p_0, there also exists a regime in which the atom
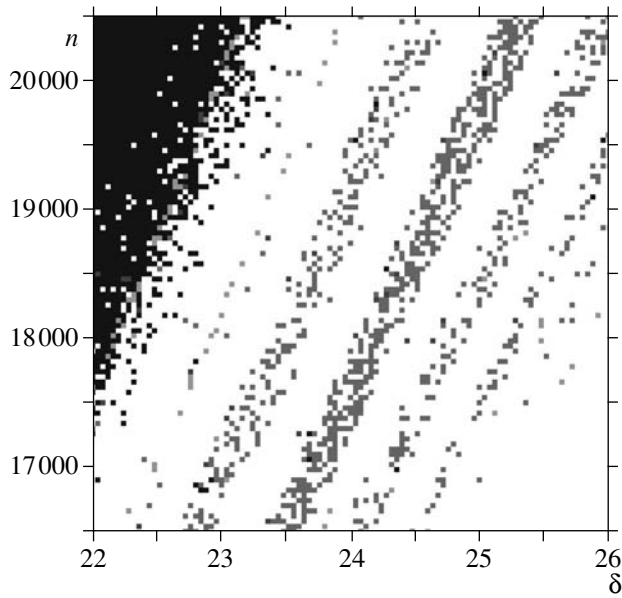
Fig. 2. Map of synchronization periods in relation to the mean number n of saturation photons and dimensionless resonance detuning δ. The cycle of period 1 is denoted by white; the cycle of period 2 is marked by light gray; the cycles of periods 3–12 are designated by dark gray; and the area of chaos is shown by black.

moves with an acceleration, whose value asymptotically tends to zero. In this case, no limit cycle is established in a reasonable time.

In order to obtain the simplest approximate analytic solutions for the limit cycles in the case of ballistic

motion, we represent the atomic polarization, the population inversion, and the momentum in the form of Fourier series in terms of harmonics $\alpha \bar{p}$, assuming $\xi \simeq \alpha \bar{p} \tau$. In the approximation of small amplitudes of higher harmonics, the limit cycle of period 1 is described by the dominant terms of the Fourier series. The approximate solution

$$p \approx \bar{p} - (\delta A/2\alpha\bar{p})\cos 2\alpha\bar{p}\tau,$$

$$u \approx -2\delta A \cos\alpha\bar{p}\tau,$$

$$v \approx -\gamma_a A \cos\alpha\bar{p}\tau + 2\alpha\bar{p}A\sin\alpha\bar{p}\tau, \qquad (4)$$

$$z \approx -1 + A + A\cos 2\alpha\bar{p}\tau,$$

$$A \equiv n/(\delta^2 - \alpha^2\bar{p}^2 + n + \gamma_a^2/4)$$

is valid for a sufficiently severe constraint $n \ll \delta^2 - \alpha^2\bar{p}^2 + \gamma_a^2/4$, which, for the parameters chosen in our numerical calculations, means that $n \ll \delta^2$.

The numerical calculations confirm that, in the case of ballistic motion and synchronization with period 1, the second harmonic prevails in the oscillations of momentum and population inversion, whereas the first harmonic dominates the oscillations of atomic polarization. Similar expressions are obtained for the synchronization of atomic oscillations in the optical potential well. In this case, however, the first harmonic prevails in the momentum oscillations, the steady component is (obviously) absent and the conditions for the validity of the solutions are less stringent.

3. Bifurcations and chaos. At the exact resonance $\delta = 0$, the optical potential vanishes, the atom flies with
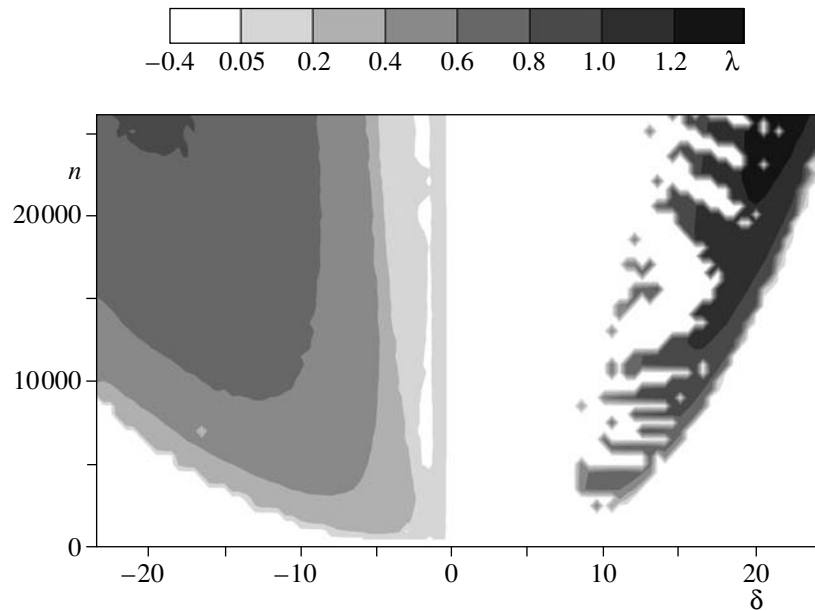

Fig. 3. Map of the maximum Lyapunov exponent λ. The coordinates are the same as in Fig. 2.
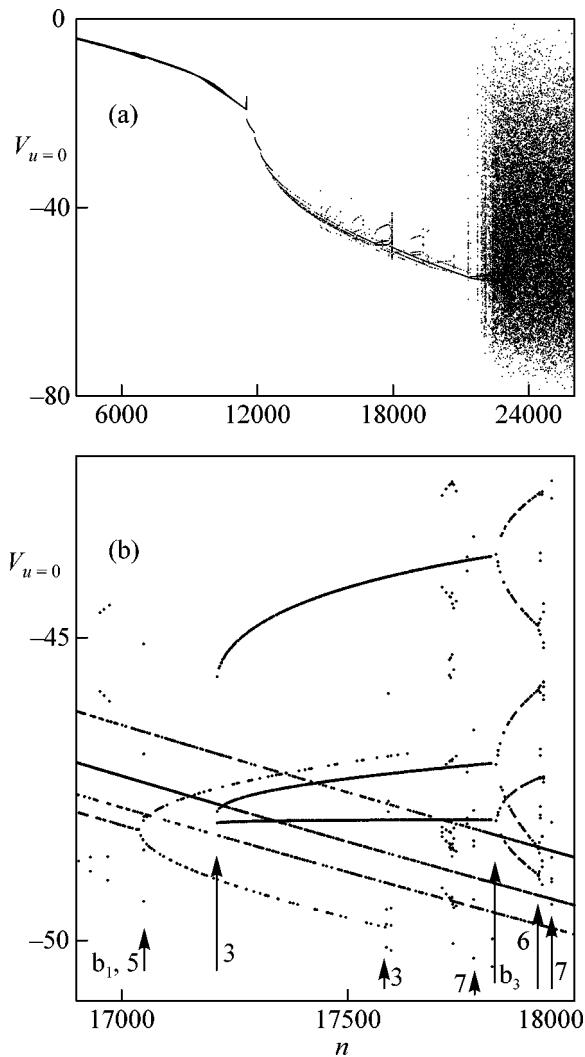
Fig. 4. Bifurcation diagram for different ranges of the number n of photons ($\delta = 24$). The arrows b_1 and b_3 show the doubling of the cycles of periods 1 and 3; arrows 3, 5, and 7 show the cycles of periods 3, 5, and 7; and arrow 6 shows the period-doubling bifurcation $3 \longrightarrow 6$.

a constant initial velocity, and its internal energy oscillates with a modulated Rabi frequency that is determined, in particular, by the spatial period of the standing wave. Synchronization takes place over a wide range of controlling parameters—the mean number n of saturation photons and the detuning δ. As the number of photons increases, bifurcations occur and cycles with periods 2, 3, etc. appear, up to a numerically found cycle with period 12. On the further increase in n, chaotic oscillations arise, which we diagnose by a positive value of the maximum Lyapunov exponent λ. Figure 2 shows the map of synchronization periods for a comparatively narrow range of n and δ. Chaos arises at a sufficiently large number of photons; furthermore, the greater the n, the shorter the synchronization establishing time. The cycle of period 1 is shown by white; the cycles of other periods are denoted by different tints of

gray; and the chaos area is shown by black. Figure 3 presents the topographic map of the Lyapunov exponent λ for wide ranges of n and δ values, which helps in distinguishing between the areas of possible synchronization and chaos. As the number n of photons increases, the approximate solutions for the cycle of period 1 lose their validity and higher harmonics become more and more pronounced in the oscillation spectrum. It follows from the map of synchronization periods that cycles of period 3 and greater appear for virtually random values of the parameters but within the clearly seen bands, between which only cycles of period 1 occur. The border of chaos is also strongly indented: there are isolated islands near the border, a small deviation from which for any controlling parameter again leads to a limit cycle.

At fixed values of all controlling parameters, different initial conditions can lead to different attractors. We revealed the coexistence of different limit cycles with riddled attraction basins [11]; that is, each point of the basin of one attractor contains, in its arbitrarily small vicinity, a point of the attraction basin of some other attractor. Such limit cycles can have both different and identical periods, but their shapes are different for close initial conditions.

Figure 4a shows the bifurcation diagram of an atom for the fixed initial conditions and detuning $\delta = 24$ and different numbers of photons n. The values of the v component of atomic polarization in time moments when the other u component turns to zero are laid off on the ordinate, with only the negative values of v being fixed. At $n \lesssim 12000$, a stable cycle of period 1 is observed and, at $12000 \lesssim n \lesssim 14000$, the cycles of period 1 begin to multiply. On further increase in n, cycles of other periods appear along with the cycles of period 1. It is seen from Fig. 4b that, at $n \lesssim 17050$, almost all points of the diagram fall on four parallel lines. In this case, for every value of n, there is only one value of v; however, upon a small change in n, the value of v randomly jumps from one line to another. The construction of an analogous diagram with varied initial conditions shows that, for these values of the parameters, four different limit cycles of period 1 coexist in the phase space of the system, each having its own attraction basin. The "fork" b_1 in Fig. 4b implies that two new cycles of period 1 arise from one initial cycle rather than the period-doubling bifurcation takes place. On further increase in n, bifurcations of the appearance of cycles with periods other than 1 are observed. In Fig. 4b, they are denoted by the corresponding numerals. Among the bifurcations in the range $14000 \lesssim n \lesssim 21000$, the period-tripling bifurcations are most typical. In addition, there are period-doubling bifurcations (for example, the vanishing of the cycle of period 3 at $n \approx 17900$ and the appearance of the cycle of period 6) and other bifurcations (for example, the appearance or vanishing of the cycle of period 3 that is not accompanied by the simultaneous vanishing or appearance of

the cycles of other periods). At least, three cycles of period 1 coexist in this entire range of n.

Beginning at $n \lesssim 21\,000$, an intermittency and, finally, chaos in the form of a chaotic strange attractor sets in. The projections of this attractor on the planes (u, v) and (z, ξ) are shown in Fig. 1c. Its chaotic nature is confirmed by the positive value of the maximum Lyapunov exponent, and its strangeness is confirmed by the calculated value of the fractal Hausdorff–Bezikovich dimension $d_f \simeq 2.7$ for $n = 24\,000$ and $\delta = 24$. To simulate the decoherence caused by the uncontrolled environment, we introduced a stochastic force into the right-hand side of the second equation in (3) and calculated the bifurcation diagram for different noise levels. At a low noise level, a small smearing of the lines of limit cycles of periods 1 and 3 is observed with retention of their characteristic properties. As the noise level increases, the fine structure of the bifurcation diagram in Fig. 4 is destroyed.

The synchronization of the atomic internal and external degrees of freedom can be detected from the atomic fluorescence spectrum. For example, the synchronized ballistic motion of an atom with a cycle of period 1 and an arbitrary shape leads to the appearance of side bands in the spectrum at the frequencies $\omega_f \pm jk_f \bar{v}_a$ $(j = 1, 2, \ldots)$, where $\bar{v}_a$ is the average velocity of the atomic steady-state motion. The synchronization with the cycle of period 3 gives rise to a denser spectrum with the frequencies $\omega_f \pm jk_f \bar{v}_a/3$, whereas chaos leads to a continuous spectrum. This can be directly verified by the calculation of the atomic mean dipole moment $d = (\mu/\sqrt{2}\,n)[(u - v)\cos\omega_f t - (u + v)\sin\omega_f t]$, where μ is the dipole-moment transition matrix element, which, for simplicity, is assumed to be real.

Some interesting issues of synchronization of chaotic oscillations and effects of random walk of an atom with fractal properties are left beyond the scope of this study. Actually, our results are valid for an atom in the field of a standing wave formed not only in a cavity but also produced by two counterpropagating laser beams in free space (see Eq. (3)). The synchronization and bifurcation effects offer additional possibilities for controlling the internal and external degrees of freedom of an atom by varying the parameters of a laser field.

REFERENCES

1. J. M. Raimond, M. Brune, and S. Haroche, Rev. Mod. Phys. **73**, 565 (2001).

2. S. V. Prants, Pis'ma Zh. Éksp. Teor. Fiz. **75**, 71 (2002) [JETP Lett. **75**, 63 (2002)].

3. A. P. Kazantsev, G. I. Surdutovich, and V. P. Yakovlev, *Mechanical Action of Light on Atoms* (Nauka, Moscow, 1991; World Sci., Singapore, 1990).

4. V. G. Minogin and V. S. Letokhov, *Laser Light Pressure on Atoms* (Nauka, Moscow, 1986; Gordon and Breach, New York, 1987).

5. C. J. Hood, T. W. Lynn, A. C. Doherty, *et al.*, Science **287**, 1447 (2000).

6. P. Münstermann, T. Fischer, P. Maunz, *et al.*, Phys. Rev. Lett. **82**, 3791 (1999).

7. S. V. Prants and V. Yu. Sirotkin, Phys. Rev. A **64**, 033412 (2001).

8. S. V. Prants, M. Edelman, and G. M. Zaslavsky, Phys. Rev. E **66**, 046222 (2002).

9. V. Yu. Argonov and S. V. Prants, Zh. Éksp. Teor. Fiz. **123**, 946 (2003) [JETP **96**, 832 (2003)].

10. S. V. Prants and M. Yu. Uleysky, Phys. Lett. A **309**, 357 (2003).

11. J. C. Sommerer and E. Ott, Nature **365**, 138 (1993).

Translated by V. Rogovoĭ

High-Contrast Dark Resonances on the D₁ Line of Alkali Metals in the Field of Counterpropagating Waves

A. V. Taĭchenachev[1], V. I. Yudin[1], V. L. Velichansky[2], S. V. Kargapoltsev[2], R. Wynands[3], J. Kitching[4], and L. Hollberg[4]

[1] *Institute of Laser Physics, Siberian Division, Russian Academy of Sciences, Novosibirsk, 630090 Russia*
e-mail: llf@laser.nsc.ru
[2] *Lebedev Institute of Physics, Russian Academy of Sciences, Moscow, 117924 Russia*
[3] *Physikalisch-Technische Bundesanstalt, 38116 Braunschweig, Germany*
[4] *National Institute of Standards and Technology, Boulder, Colorado 80305, USA*
Received July 5, 2004

A new method providing a significant increase in the amplitude and contrast of dark resonances is proposed. The method is based on the use of the σ_+–σ_- configuration of polarized counterpropagating waves, D₁-line excitation in alkali metal atoms, and small-sized cells. Qualitative considerations of the scheme are confirmed by the results of numerical calculations. A variant of a standing wave with homogeneous circular polarization is also discussed. © 2004 MAIK "Nauka/Interperiodica".

PACS numbers: 42.50.Gy; 42.62.-b

1. The coherent population trapping (CPT) effect of atoms interacting with a resonant electromagnetic field is well known (see review [1] and references therein) and widely used in various fields of atomic and laser physics. The frequency and time standards (atomic clocks) [2, 3] and magnetometers [4] are the most promising applications in metrology. The main advantage of atomic clocks based on the CPT effect in a two-frequency field is that the corresponding RF resonance (so-called dark resonance) is excited by optical methods. This approach opens wide possibilities for reducing the size of such devices while retaining a sufficiently high precision of frequency determination [5].

However, use of the CPT phenomenon encounters some basic physical problems associated with the optimization of the two-photon resonance parameters (width, amplitude, position, and shape of the resonance line). In particular, a decrease in the resonance line width can be achieved by using cells with a buffer gas [6]. Another problem, related to an increase in the signal amplitude, can be solved by selecting a proper scheme for the excitation of atomic levels. For example, we have recently demonstrated [7] that excitation of the D₁ line rather than D₂ provides a significant increase in the amplitude and contrast of the nonlinear resonance for alkali metal atoms. Unfortunately, this method has an intrinsic limitation caused by the lack of cyclicity in the interaction of atoms with circularly polarized light at the D₁ line.

This paper proposes a new method ensuring the cyclicity of such interaction and, hence, providing a further significant increase in the amplitude and contrast of the dark resonance on the D₁ line, as compared to the level achieved previously in [7]. The method is based on the use of an atomic cell of small size (much smaller than the RF-transition wavelength) and a field formed by counterpropagating waves with orthogonal circular polarizations (the so-called σ_+–σ_- field configuration). In this approach, the use of a constructive interference of two-photon transitions excited by the unidirectional waves is quite important. Calculations show the possibility of a manifold increase in the amplitude of resonance signal and amplitude-to-width ratio, as compared to those achieved by other methods.

2. In CPT-based clocks, the Zeeman sublevels with the angular momentum projection $m = 0$ of two ground-state hyperfine components of an alkali metal atom are the working energy levels. The quantum coherence between these sublevels is provided by two-photon Raman transitions induced by a circularly polarized two-frequency radiation field,

$$\mathbf{E}(t) = (A_1 e^{-i\omega_1 t} + A_2 e^{-i\omega_2 t})\mathbf{e}_{\pm 1} + \text{c.c.,} \qquad (1)$$

in the presence of a level-splitting static magnetic field directed perpendicularly to the polarization plane. Here, $\mathbf{e}_{\pm 1} = \mp(\mathbf{e}_x \pm i\mathbf{e}_y)/\sqrt{2}$ is the unit vector of the clockwise (+) or anticlockwise (–) circular polarization and $A_{1,2}$ are the scalar amplitudes of the corresponding frequency components. The spectroscopic signal usually represents the total absorption depending on the frequency difference $\omega_1 - \omega_2$ between the unidirectional propagating waves. When this difference is detuned in the vicinity of the ground-state Δ_{hfs} fre-
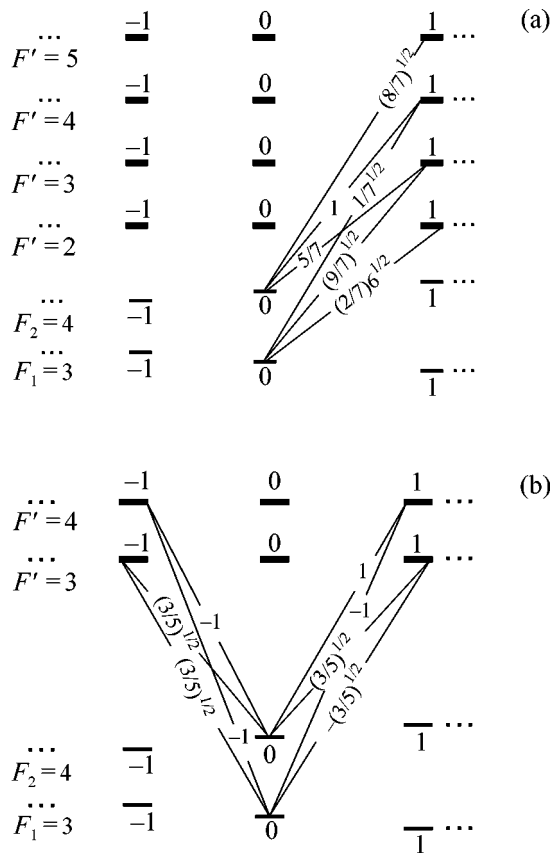
Fig. 1. Schematic diagram of the light-induced transitions from the $|F_1, m_1 = 0\rangle$ and $|F_2, m_2 = 0\rangle$ states in a two-frequency field. Numbers at the levels indicate the relative matrix elements of the circular components of the dipole moment operator for ^{133}Cs: (a) σ_+ polarized field for the D$_2$ line; (b) σ_+–σ_- field configuration for the D$_1$ line.
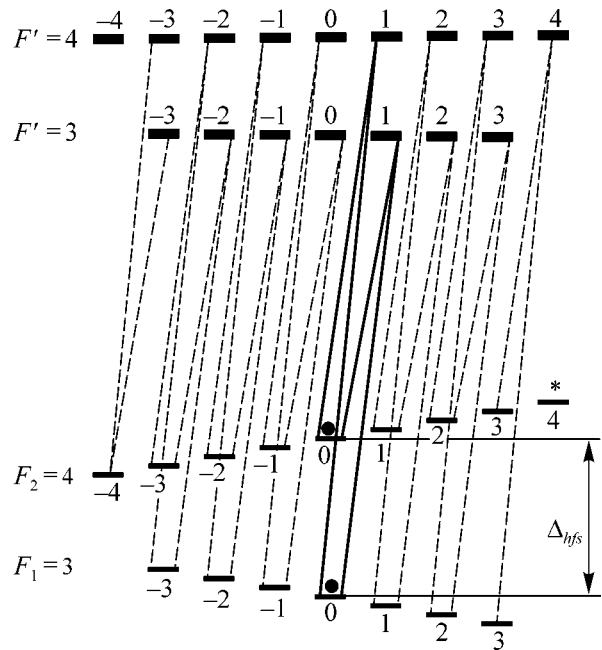

Fig. 2. Schematic diagram of the light-induced transitions in a two-frequency σ_+ polarized field for the D$_1$ line of ^{133}Cs. Thick solid lines indicate transitions from the $|F_1, m_1 = 0\rangle$ and $|F_2, m_2 = 0\rangle$ states (denoted by black circles). The coherence between these states is generated due to two-photon Raman transitions at the Δ_{hfs} frequency. The asterisk indicates the trapping state: $|\text{pump}\rangle = |F_2, m_2 = F_2\rangle$.

quency, the absorption signal exhibits a more or less pronounced dip (so-called dark resonance), whose width is determined by the relaxation rate (translational, diffusional, and collisional) in the ground state and by the field parameters (intensity and one-photon detuning).

The use of dark resonances for the design of atomic clocks encounters the need to increase the signal amplitude, contrast, and amplitude-to-width ratio. One possible way to solve these problems consists in selecting the optimum excitation scheme. It is well known [8] that the resonance contrast for the D$_2$ line cannot exceed a few percent of the linear absorption. This is caused by a small efficiency of coherence generation between the working levels under conditions of strong broadening of optical transition in the collisions with buffer gas. Indeed, in the case of strong collisional broadening, the spectral resolution of hyperfine components in the excited state is absent. Figure 1a shows the scheme of light-induced transitions between the working levels of the ground state ($m_{1,2} = 0$) for the ^{133}Cs D$_2$ line. As can be seen, the two-photon transitions excited

via different upper sublevels $|F' = 4, m = 1\rangle$ and $|F' = 3, m = 1\rangle$ interfere destructively. In addition, the isolated one-photon transitions with $|F' = 5, m = 1\rangle$ and $|F' = 2, m = 1\rangle$ also destroy the two-photon coherence between the lower sublevels. On the whole, it can be ascertained that, under the conditions of strong collisional broadening of optical transitions at the D$_2$ line of alkali metal atoms, the dark (i.e., nonabsorbing light) state is, strictly speaking, absent.

However, as was shown in our work [7], this problem can be solved by using the D$_1$ line, which provides an appreciable increase in the amplitude and contrast of the dark resonance. Physically, this is caused by the fact that the D$_1$ line, in contrast to D$_2$, exhibits the $|\text{dark}\rangle$ state even in the case of a strong collisional broadening of the optical transition (i.e., in the absence of spectral resolution of hyperfine components in the excited state), provided that the two-photon resonance condition $(\omega_1 - \omega_2) = \Delta_{hfs}$ is fulfilled. This state is a coherent superposition of the Zeeman sublevels $|F_1, m_1 = 0\rangle$ and $|F_2, m_2 = 0\rangle$ (see Fig. 2) and satisfies the condition

$$(\hat{\mathbf{d}}\mathbf{E})|\text{dark}\rangle = 0. \qquad (2)$$

For the clockwise circular polarization, $\mathbf{e}_{+1}$, dark state (2) has the form

$$|\text{dark}\rangle = \mathcal{N}(|F_1, m_1 = 0\rangle + (A_1/A_2)|F_2, m_2 = 0\rangle), \quad (3)$$
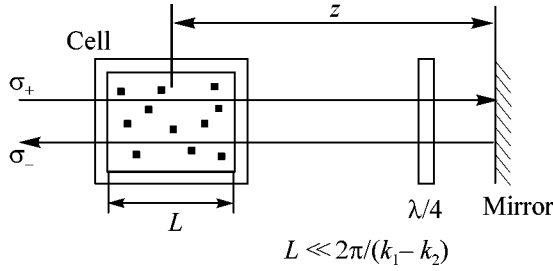
Fig. 3. Schematic diagram illustrating the formation of a σ_+–σ_- field configuration ($\lambda/4$ is a quarter-wave plate).

where $\mathcal{N} = (1 + |A_1/A_2|^2)^{-1/2}$ is the normalization factor. This expression follows from the values of the dipole-moment operator matrix elements (see Fig. 1b). However, the D_1 transition in a circularly polarized field always involves a trapping state $|\text{pump}\rangle = |F_2, m = F_2\rangle$ (Fig. 2), which is insensitive to the two-photon detuning $\delta_R = (\omega_1 - \omega_2) - \Delta_{\text{hfs}}$. Atoms accumulated in this state are excluded from the process of coherence generation between the working sublevels with $m_{1,2} = 0$, leading to certain constraints on the amplitude and contrast of the dark resonance.

This obstacle can be bypassed by using small-sized cells and the σ_+–σ_- configuration of the two-frequency field formed by counterpropagating waves (along the z axis) with the opposite circular polarizations:

$$\begin{aligned}
\mathbf{E}(z, t) &= (E_1^{(+)} e^{ik_1 z} \mathbf{e}_{+1} + E_1^{(-)} e^{-ik_1 z} \mathbf{e}_{-1}) e^{-i\omega_1 t} \\
&+ (E_2^{(+)} e^{ik_2 z} \mathbf{e}_{+1} + E_2^{(-)} e^{-ik_2 z} \mathbf{e}_{-1}) e^{-i\omega_2 t} + \text{c.c.}
\end{aligned} \tag{4}$$

In this case, the aforementioned $|\text{pump}\rangle$ state is absent. Dark resonances in the signal of local fluorescence arising in such a field have recently been studied in large cells [9]. In this system, the resonance amplitude exhibited a periodic spatial variation caused by the spatial incursion of the relative phase difference $2(k_1 - k_2)z$, where $k_j = 2\pi/\lambda_j$ is the wave vector of the field with the frequency ω_j and z is the coordinate of the observation point. Thus, the phenomenon of spatial modulation of the signal amplitude with a period of $\pi/(k_1 - k_2)$ is caused by the difference in the wavelengths λ_1 and λ_2 of the two frequency components. For example, for ^{133}Cs atoms, this period is $\pi/(k_1 - k_2) \approx 1.6$ cm.

For the exact two-photon resonance $\delta_R = 0$, the dark state for a wave propagating in the positive direction ($\mathbf{e}_{+1}$ polarization) has the form

$$\begin{aligned}
&|\text{dark}^{(+)}\rangle \\
&= \mathcal{N}_\beta(|F_1, m_1 = 0\rangle + \beta e^{i(k_1 - k_2)z}|F_2, m_2 = 0\rangle),
\end{aligned} \tag{5}$$

while the dark state for the wave propagating in the opposite direction ($\mathbf{e}_{-1}$ polarization) is

$$\begin{aligned}
&|\text{dark}^{(-)}\rangle \\
&= \mathcal{N}_\beta(|F_1, m_1 = 0\rangle - \beta e^{-i(k_1 - k_2)z}|F_2, m_2 = 0\rangle),
\end{aligned} \tag{6}$$

where $\beta = E_1^{(+)}/E_2^{(+)} = E_1^{(-)}/E_2^{(-)}$ and $\mathcal{N}_\beta = (1 + |\beta|^2)^{-1/2}$ is the normalization factor. These expressions follow from the values of the dipole-moment operator matrix elements (see Fig. 1b). As can be seen from these formulas, the dark states $|\text{dark}^{(+)}\rangle$ and $|\text{dark}^{(-)}\rangle$ coincide at the points z_{max} satisfying the condition

$$2(k_1 - k_2)z_{\text{max}} = (2n+1)\pi \quad (n = 0, \pm 1, \ldots), \tag{7}$$

which implies a constructive interference of the Raman transitions. Therefore, the dark state at these points exists also for the total field (4) and the resonance amplitude is maximal. At all other points of the space, the dark states of the counterpropagating waves do not coincide, $|\text{dark}^{(+)}\rangle \neq |\text{dark}^{(-)}\rangle$, and the exact dark state does not exist for field (4) (destructive interference), resulting in a decrease in the amplitude of dark resonance. Its amplitude is minimal at the points $2(k_1 - k_2)z_{\text{min}} = 2n\pi$.

In the case of a large cell, $L \geq \pi/(k_1 - k_2)$, the resonance amplitude of the total absorption in the σ_+–σ_- field shows no significant increase because of spatial averaging. However, for small cells with the characteristic longitudinal size $L \ll 2\pi/(k_1 - k_2)$, phase relations between the field components are approximately the same over the entire volume. For this reason, placing such a cell at a point with the coordinate obeying condition (7), one can expect a significant increase in the dark-field amplitude on the D_1 line, since two-frequency field (4) has a dark state, while the trapping state $|\text{pump}\rangle$ is absent.

It should be noted that the required σ_+–σ_- configuration (4) of counterpropagating waves can be obtained using the standard system shown in Fig. 3. If the incident wave has the σ_+ polarization, the reflected wave at the output of quarter-wave plate will possess the opposite σ_- polarization. According to formula (7), the minimal distance from the mirror to the cell is $\pi/2(k_1 - k_2)$. For ^{133}Cs atoms, this distance is about 0.8 cm; however, with allowance made for the dielectric constant $\varepsilon > 1$ of the cell window and materials of the quarter-wave plate, the actual distance will be somewhat smaller.

3. The above qualitative considerations can be illustrated by the results of numerical calculations of the total absorption signal for the σ_+–σ_- field configuration in a small cell with the center placed at a point with the coordinate z_{max} according to formula (7). The calculation performed for the D_1 line of alkali metal atoms was based on the application of the methods developed in [9, 10] to the case under consideration. This approach completely takes into account the real hyperfine and

Zeeman structures of the energy levels, as well as the effects of optical pumping caused by the radiation relaxation.

It was demonstrated in [10, 11] that the narrow non-linear resonance as a function of two-photon detuning δ_R is well described by the generalized Lorentzian

$$f(\delta_R) = B + \frac{C_0 \gamma_R^2 / 4}{\gamma_R^2/4 + (\delta_R - \delta_0)^2} + \frac{C_1(\delta_R - \delta_0)\gamma_R}{\gamma_R^2/4 + (\delta_R - \delta_0)^2}, \quad (8)$$

where γ_R is a parameter describing the two-photon resonance width; δ_0 is the position of this resonance relative to the ground-state hyperfine splitting Δ_{hfs}; C_0 and C_1 are the amplitudes of the symmetric and antisymmetric contributions, respectively; and B is the resonance background level. Note that expression (8) describes the resonance circuit both for the running/standing circularly polarized wave and for the $\sigma_+ - \sigma_-$ field configuration. All quantities γ_R, δ_0, B, C_0, and C_1 depend on the following parameters: the one-photon detuning, the total field intensity, the frequency-component intensity ratio $\beta^2 = |E_1^{(+)}/E_2^{(+)}|^2 = |E_1^{(-)}/E_2^{(-)}|^2$, the ground-state relaxation rate Γ, and the one-photon optical transition width γ_{opt}. The presence of a buffer gas influences the values of Γ and γ_{opt}, which are phenomenological parameters of the model and should be determined from experiment. Indeed, the value of γ_{opt} can be estimated from the absorption of the running monochromatic wave, while the value of Γ can be determined from the two-photon resonance width (equal to 2Γ) in a weak field (where the field-induced broadening is absent). In the case where the collisional broadening of the optical resonance exceeds the Doppler width ($\gamma_{opt} > k\overline{v}$, which frequently occurs in practice), the atomic motion (for one-photon resonances) can be ignored in calculations of the spectroscopic signal.

From the practical point of view, equal intensities of two frequency components ($|\beta| = 1$) is the most typical and important situation. In this case, $C_1 = 0$ (the antisymmetric contribution in (8) for the D_1 line is absent) and the dark resonance has the form of a symmetric (relative to δ_0) contour with the amplitude C_0. This result follows from the analysis performed in [10] and is caused by a special relation between the matrix elements of the dipole moment operator (Fig. 1b). Clearly, the symmetry of the resonance circuit (independent of the one-photon detuning and the field intensity) is an important advantage of using the D_1 line rather than D_2 for the design of CPT-based atomic clocks.

Figure 4 shows the results of calculations for the ^{133}Cs D_1 line. These data clearly demonstrate the advantage of using the $\sigma_+ - \sigma_-$ field configuration instead of the usual case of running circularly polarized waves. The spectroscopic signal was the total field absorption in the approximation of optically thin medium. The
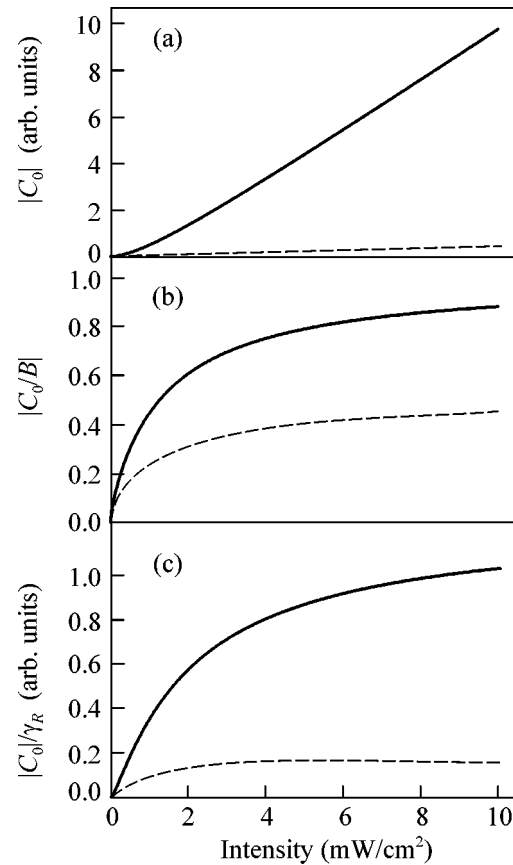

Fig. 4. Plots of the parameters of dark resonance (8) versus the field intensity (for unidirectional waves) in the $\sigma_+ - \sigma_-$ configuration (solid curves) and the running circularly polarized wave (dashed curves): (a) dark resonance amplitude $|C_0|$; (b) resonance contrast $|C_0/B|$; (c) line amplitude-to-width ratio $|C_0|/\gamma_R$. All calculations were performed for $\Gamma = 100$ Hz, $\gamma_{opt} = 1$ GHz, and $\beta = 1$; intensities of the counterpropagating waves in the $\sigma_+ - \sigma_-$ field were taken equal, and both frequencies $\omega_{1,2}$ occurred near the one-photon resonance with the upper level $|F' = 4\rangle$.

atomic parameters (Γ and γ_{opt}) were taken to be equal to the values typical of the experiments with a buffer gas.

As can be seen from Fig. 4a, the dark-resonance amplitude $|C_0|$ can be increased by more than an order of magnitude even at moderate intensities. The contrast of the resonance (defined as the $|C_0/B|$ ratio) tends to unity with increasing intensity (Fig. 4b), while the maximum value for the running waves is 0.5 (which is a direct consequence of the existence of the trapping state $|pump\rangle$). From the viewpoint of the frequency measurement and stabilization, the amplitude-to-width ratio $|C_0|/\gamma_R$ is an important parameter. As can be seen from Fig. 4c, the use of the $\sigma_+ - \sigma_-$ field configuration allows this parameter to be significantly increased. For the running wave, this ratio even begins to decrease at large field intensities.

For comparison, we performed analysis and numerical calculations for a configuration of counterpropagating waves with the same circular polarization (e.g., the standing σ_+ wave), whereby the quarter-wave plate in the scheme of Fig. 3 is absent. In this case, the condition for the constructive interference between the two two-photon transitions due to unidirectional waves is satisfied if the cell is placed at a point with the coordinate $z = n\pi/(k_1 - k_2)$. However, in this configuration (in contrast to the σ_+–σ_- field), the trapping state $|\text{pump}\rangle$ does not disappear and, hence, there are no grounds to expect a significant increase in the parameters of the dark resonance in comparison to those observed in the case of a usual running circularly polarized wave. Indeed, the results of our calculations showed that spectroscopic signal (8) for a standing circularly polarized wave is generally similar (provided that $\gamma_{opt} > k\bar{v}$) to the signal for a running wave with a somewhat higher intensity. Thus, the use of a standing wave offers a way to increase (up to two times) the effective intensity relative to the scheme with a running wave, which can also be useful in practice.

4. In summary, we have proposed a new method providing a significant increase in the amplitude and contrast of dark resonances. The method is based on the use of a σ_+–σ_- configuration of polarized counterpropagating waves, D_1 line excitation in alkali metal atoms, and small-sized cells. Qualitative considerations of this scheme are confirmed by the results of numerical calculations. The obtained high-contrast resonances can be used for the design of small-sized atomic clocks.

For the verification of these conclusions, we have performed experiments with a small-sized cell containing ^{133}Cs vapor [12]. The obtained results are in good agreement with the theoretical calculations. Unfortunately, the insufficient power of the available laser on the ^{133}Cs D_1 line provided only a moderate (1.5-fold) increase in amplitude of the resonance absorption per

wave (we also observed a significant improvement in comparison to the case of a standing circularly polarized wave). However, the theoretical results of this study allow us to expect a much more pronounced increase in parameters of the dark resonance with increasing laser intensity, due to a significant effect of the optical pumping on ground-state Zeeman sublevels.

REFERENCES

1. E. Arimondo, in *Progress in Optics*, Ed. by E. Wolf (North-Holland, Amsterdam, 1996), Vol. 35, p. 257.
2. P. R. Hemmer, S. Ezekiel, and C. C. Leiby, Jr., Opt. Lett. **8**, 440 (1983).
3. J. Kitching, S. Knappe, N. Vukicevic, *et al.*, IEEE Trans. Instrum. Meas. **49**, 1313 (2000).
4. M. Stähler, S. Knappe, C. Affolderbach, *et al.*, Europhys. Lett. **54**, 323 (2001).
5. L.-A. Liew, S. Knappe, H. Robinson, *et al.*, Appl. Phys. Lett. **84**, 2694 (2004).
6. S. Brandt, A. Nagel, R. Wynands, and D. Meschede, Phys. Rev. A **56**, R1063 (1997).
7. M. Stähler, R. Wynands, S. Knappe, *et al.*, Opt. Lett. **27**, 1472 (2002).
8. R. Wynands and A. Nagel, Appl. Phys. B **68**, 1 (1999).
9. C. Affolderbach, S. Knappe, R. Wynands, *et al.*, Phys. Rev. A **65**, 043810 (2002).
10. A. V. Taĭchenachev, V. I. Yudin, R. Wynands, *et al.*, Phys. Rev. A **67**, 033810 (2003).
11. S. Knappe, M. Stahler, C. Affolderbach, *et al.*, Appl. Phys. B **76**, 57 (2003).
12. S. V. Kargapoltsev, J. Kitching, V. L. Velichansky, *et al.*, Laser Phys. Lett. **1**, 495 (2004).

Translated by P. Pozdeev

Stable Dust Structures in Non-Self-Sustained Gas Discharge under Atmospheric Pressure

V. N. Babichev[1], A. F. Pal'[1], A. N. Starostin[1], A. V. Filippov[1, *], and V. E. Fortov[2]

[1] *Troitsk Institute for Innovation and Fusion Research, Troitsk, Moscow region, 142190 Russia*

*e-mail: fav@triniti.ru

[2] *Institute for High Energy Densities, Russian Academy of Sciences, ul. Izhorskaya 13/19, Moscow, 125412 Russia*

Received July 8, 2004

The formation of stable dust structures in electron-beam-controlled non-self-sustained discharge plasma was predicted and experimentally observed. To determine the conditions for dust-particle levitation, the self-consisted one-dimensional simulation of a non-self-sustained gas discharge was carried out using a nonlocal model of charged plasma-particle transport with allowance for electron diffusion. It is shown that, in the cathode layer of a non-self-sustained gas discharge, a strong electric field arises in the Thomson regime, which, in conjunction with the gravity force, forms a potential well where the dust particles undergo levitation. © *2004 MAIK "Nauka/Interperiodica"*.

PACS numbers: 52.27.Lw

INTRODUCTION

The investigation of plasmas containing micron-sized dust particles has attracted increased interest from both fundamental and practical points of view [1]. In particular, this interest is generated by the problem of designing an autonomous photovoltaic electrical energy source with the use of radioactive fuel in the form of micron-sized dust particles [1, 2]. The formation of a homogeneous gas–dust mixture with suppressed sedimentation and hampered deposition of dust particles on the walls is one of the key problems in designing such an energy source. The solution of this problem requires the formation of an ordered structure of dust particles, which is also necessary for reducing the loss of ultraviolet quanta formed under the action of high-energy radioactive-decay particles in an inert-gas medium upon their transport to the photovoltaic converters. This work is devoted to the study of the dynamics of dust plasma formed upon the injection of dust particles into an atmospheric-pressure gas ionized by an electron beam that models the radioactive-decay β particles.

EXPERIMENTAL

An electron beam with an energy varying from 85 to 115 kV was formed in a vacuum accelerator with a filamentary cathode and led through a 14-μm-thick aluminum foil into a cylinder-shaped working chamber 7 cm in diameter and 3 cm in height. The radius of electron-beam core was about 0.6 cm. The accelerator exit window was at a distance of 7.2 cm from the lower electrode. To suppress convection, a 1.6-cm-edge glass

cube opened at the top (on the electron-beam side) and bottom (on the side of the lower electrode) was inserted into the central part of the chamber. A dc negative voltage with an amplitude of 200–4000 V was applied to the massive lower copper electrode. A grounded grid of diameter 2.4 cm covering the glass cube at a distance of 1.9 cm from the cathode served as an anode. The beam current at the exit window of the electron accelerator varied in the experiments within 50–1000 μA (the current density at the lower electrode varied in the range 0.05–1.0 μA/cm^2). The electron accelerator operated in the stationary mode. The injection of dust particles from the storage ring was accomplished by the working-gas flow. The behavior of dust particles illuminated by a laser "knife" was observed using a digital video camera.

The video frames of the polydispersed CeO_2 dust particles with a mean size of 1 μm recorded in nitrogen at an electron gun accelerating voltage of 115 kV, a beam current at the exit window of about 100 μA, and a gas pressure of 1 bar are shown in Fig. 1. Near the lower electrode, the nitrogen ionization rate caused by this beam in the cubic insertion was on the order of 10^{14} cm^{-3} s^{-1}. In the first frame in Fig. 1, one can see the persistent formation of the disk-shaped dust particles. The evolution of this disk upon the jumplike change in the voltage on the discharge gap is shown in the subsequent frames. The voltage on the lower electrode (-500 V at $t = 0$) was abruptly increased to -1000 V, as a result of which the dust cloud exploded to form, approximately within 14 s, a disk with clear-cut side boundaries at a different height. Above the disk, stable vortices were formed near the side cube walls, where
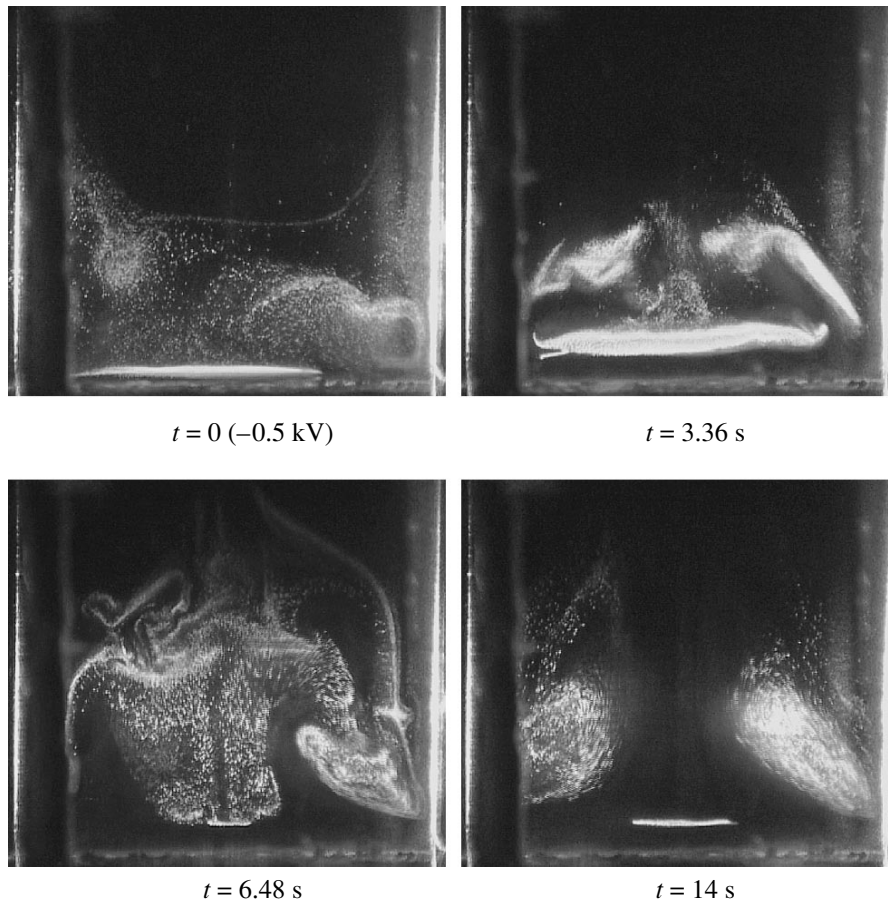
$t = 0$ (–0.5 kV) $t = 3.36$ s

$t = 6.48$ s $t = 14$ s

Fig. 1. Video frames of dust-structure evolution in a non-self-sustained gas discharge in nitrogen after an abrupt increase from –500 to –1000 V in voltage at the lower electrode ($p = 1$ bar; beam current 100 μA).

the dust particles moved up at the center and descended along the side walls of the cubic insertion. Interestingly, the lower boundary of the vortices virtually coincides with the disk position.

Upon grounding the lower electrode in a time on the order of 0.1 s, all dust particles deposited on the lower electrode; upon removing the ground and restoring the initial voltage, they were rejected upward. In this case, the disk was not restored, but the vortices appeared at their previous places. After leaking-in a new portion of dust particles, a more developed disk was formed with the vortices situated at the previous places. It is also worthy of note that the dust particles did not penetrate into the cube region below the disk level neither after leaking nor in the course of the subsequent motion, while, in the discharge chamber outside the cube, where the vortex motion of dust particles is faster because of the convective flows, the particles appeared also near the lower electrode. The pattern of particle movement described above in the cube also did not change for the unchanged discharge-gap parameters.

Upon a smooth change in the voltage on the discharge gap or in the beam current density, the disklike structure smoothly moves up or down. The same behavior was observed in argon, where the disk of carbon-glass dust particles with an average diameter of about 6 μm was considerably thicker and more stable, while the vortices near the side walls did not form. It is likely that this was due to a considerably weaker argon heating, as compared to nitrogen, in which the energy at low reduced fields E/N mainly goes to the excitation of the rotational energy levels effectively coupled to the translational degrees of freedom. For this reason, in the central near-cathode region in nitrogen, where the current is still determined by the electronic component, while the field already increases, a region of stronger gas-heating arises, resulting in a weak convective upward flow. This flow picks up the dust particles in the central region.

A disk with a diameter of 6 μm was also formed in nitrogen in the experiments with carbon-glass dust particles, but it was destroyed rather fast, while the formation of a disk composed of even greater dust particles of radius 12 ± 3 μm was observed in argon. However, in contrast to the disk formed from dust particles with a diameter of 6 μm, which existed in argon for several minutes almost stationary without changing its shape, the disk formed from a coarse dust was rapidly destroyed. Note that the dust particles in nitrogen of a medium carbon glass in laser knife had a regular,

though unstable, structure, while the structure in argon has not been resolved so far.

NUMERICAL SIMULATION OF THE NON-SELF-SUSTAINED GAS-DISCHARGE STRUCTURE

In [3], it was predicted that the formation of ordered plasma dust structures in nitrogen is possible only at low gas-ionization rates no higher than $10^{14}\,\mathrm{cm}^{-3}\,\mathrm{s}^{-1}$. To determine the conditions for dust-particle levitation in a non-self-sustained discharge (ND) in nitrogen, numerical simulation of the cathode layer was performed in this work. The simulation was carried out using the nonlocal model of transport processes developed by us in [4] for studying the dust-particle charging process. In a number of works devoted to ND simulation [5–8], a simple model of transport processes with constant kinetic coefficients, recombination coefficient, and ionization rate was used, while the electron diffusion was ignored. This model allows analytic solution with some additional simplifications [9, 10]. In our model, all kinetic coefficients and transport coefficients are functions of electron temperature, which is itself a function of coordinates and is determined from the electron-energy balance equation. The inclusion of electron diffusion is important for the correct description of the anode layer in the Thomson weak-current ND glow regime.

We take the origin of the z axis at a cathode and direct it from the cathode to an anode perpendicular to the electrode surfaces. In our experiments, the characteristic transverse size of the discharge-glow region was several times greater than the size of cathode layer, while the gas ionization, according to estimates, was rather homogeneous along the radius. For this reason, the simulation was carried out in a one-dimensional plane geometry. The system of equations of the nonlocal transport model has the form

$$\frac{\partial n_e}{\partial t} - \frac{\partial^2 (D_T n_e)}{\partial z^2} - \frac{\partial (k_e n_e E)}{\partial z} = R_e, \qquad (1)$$

$$\frac{\partial n_i}{\partial t} - D_i \frac{\partial^2 n_i}{\partial z^2} + k_i \frac{\partial (n_i E)}{\partial z} = R_i, \qquad (2)$$

$$\frac{3}{2}\frac{\partial p_e}{\partial t} - \frac{\partial^2 (g_e p_e)}{\partial z^2} - \frac{\partial (b_e p_e E)}{\partial z} = R_h, \qquad (3)$$

$$\frac{\partial^2 \phi}{\partial z^2} = -4\pi e (n_i - n_e), \quad E = -\frac{\partial \phi}{\partial z}, \qquad (4)$$

where $R_e = R_i = Q_{\mathrm{ion}} + \nu_{\mathrm{ion}} n_e - \beta_{ei} n_e n_i$ are the electron and ion production and loss sources; $R_h = (\partial (D_T n_e)/\partial z + k_e n_e E)eE + Q_{\mathrm{ion}}\varepsilon_h - p_e \omega_S - \beta_{ei} p_e n_i (2 - x/2)$ are the heat sources; n_e, n_i, k_e, k_i, D_T, and D_i are the electron and ion concentrations, mobilities, and diffusion coefficients, respectively; $p_e = n_e T_e$ is the electron-gas pressure; Q_{ion}

is the z-dependent gas-ionization rate under the action of an external source; ν_{ion} is the gas-ionization frequency by the intrinsic plasma electrons; β_{ei} is the electron–ion recombination coefficient, which can be represented for many ions in the form $\beta_{ei} = \beta_{ei0} T_e (1 - x)/2$, where x is the exponent in the dependence of the recombination cross section on the electron velocity: $\sigma_{ei} = \sigma_{ei0}/v_e^x$; ε_e is the mean electron energy related to the electron temperature by the expression $T_e = 2\varepsilon_e/3$; ε_h is the fast-electron energy going into gas heating per one event of electron–ion pair production; g_e is the electron-energy diffusion coefficient related to the heat conductivity coefficient by the relationship (for the Maxwellian distribution, these quantities coincide if the electron free path is independent of energy)

$$k_{e,T} = \left(g_e + T_e \left[\frac{\partial g_e}{\partial T_e} - \frac{b_e}{k_e}\frac{\partial D_T}{\partial T_e} \right] \right), \qquad (5)$$

where b_e is the thermoelectric coefficient; w_S is the energy-loss rate in elastic and inelastic collisions (including ionization collisions); ϕ and E are the electric-field potential and strength, respectively; and e is the absolute value of electron charge. The recombination term in the electron-energy balance equation has not been considered in the literature so far, although it is important in the Thomson's weak-current non-self-sustained discharge-glow regime, for which the field in the positive column is exceedingly low (see below). For the Maxwellian electron-energy distribution function, the transport coefficients are related to each other by the formulas

$$\frac{D_T}{k_e} = \frac{T_e}{e}, \quad \frac{g_e}{b_e} = \frac{T_e}{e}. \qquad (6)$$

At the cathode ($z = 0$), the effective boundary conditions for the balance equations were specified with allowance made for the secondary ion–electron emission with the coefficient γ, and the potential was taken equal to the potential applied to the cathode (for the Maxwellian distribution function, the factors 1/4 and 1/2, according to the kinetic theory of gases, enter the expressions for the unidirectional particle and energy fluxes, respectively):

$$\frac{1}{4} v_{T,e}\left(n_e - \gamma_e l_e \frac{\partial n_e}{\partial z} \right) = (k_e n_e + \gamma k_i n_i) E,$$

$$\frac{1}{2} v_{T,e}\left(p_e - \gamma_\varepsilon l_e \frac{\partial p_e}{\partial z} \right) = (b_e p_e + 2\gamma k_i n_i T_c) E,$$

$$\left(n_i - \gamma_i l_i \frac{\partial n_i}{\partial z} \right) = 0, \quad \phi|_{z=0} = U_d,$$

where l_e, l_i, $v_{T,e}$, and $v_{T,i}$ are the electron and ion mean free paths and thermal velocities, respectively; T_c is the temperature of secondary electrons, taken equal to the
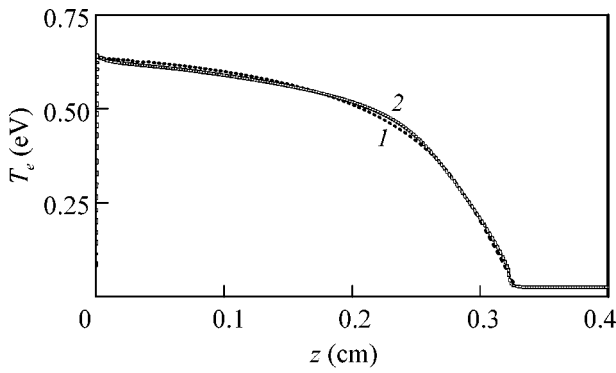
Fig. 2. Electron temperature distribution in a non-self-sustained gas discharge in nitrogen at $U_d = 500$ V, $p = 1$ bar, $L = 1.0$ cm, $Q_{ion} = 10^{14}$ cm^{-3} s^{-1}: (*1*) calculation with local model and (*2*) nonlocal model.

Fig. 3. Electric-field distribution in the non-self-sustained gas discharge in N$_2$ at $p = 1$ bar, $L = 1.0$ cm, $Q_{ion} = 10^{14}$ cm^{-3} s^{-1}: $U_d = $ (*1*) 500, (*2*) 1000, (*3*) 2000, and (*4*) 4000 V (the *y*-ordinate for the dashed curves is given at the right).

cathode temperature; and γ_e, γ_i, and γ_ε are the constants defined by the relationships

$$\gamma_e = 2D_T/l_e v_{T,e}, \quad \gamma_i = 2D_i/l_i v_{T,i}, \quad \gamma_\varepsilon = g_e/l_e v_{T,e}$$

(for the hard-sphere model, $\gamma_e = \gamma_i = \gamma_\varepsilon = 2/3$). The following boundary conditions were specified at the anode ($z = L$):

$$\left[n_e - \gamma_e l_e \frac{\partial n_e}{\partial z}\right] = 0, \quad \left[n_i - \gamma_i l_i \frac{\partial n_i}{\partial z}\right] = 0,$$

$$\left[p_e - \gamma_\varepsilon l_e \frac{\partial p_e}{\partial z}\right] = 0, \quad \phi|_{z = L} = 0.$$

Since the calculations showed that the ion diffusion could be ignored over the entire discharge region, we solved the first-order differential balance equation for ions with zero boundary condition at the anode. In this case, the directional differences were used to approximate the derivative with respect to coordinate. In Fig. 2, the electron temperatures obtained for the ND in the completely nonlocal and local models are compared with each other. In the local model, the reduced system of Eqs. (1), (2), and (4) was solved without electron-energy balance equation (3), and the electron transport coefficients were determined from the local value of the reduced field. One can see that the distinction is observed only near the cathode, where the influence of cold cathode on the electron temperature is significant in the nonlocal model. For this reason, the main calculations were carried out using the local transport model.

The electric-field distributions in the ND in nitrogen are shown in Fig. 3. These patterns are in good agreement with the analytic results [9, 10]. One can see that the field in the positive column is low and increases drastically in the cathode region. Calculations with the discharge-voltage switching from 500 to 1000 V were also carried out. It proved that the field in the cathode layer is rearranged within microseconds upon an increase in voltage and, due to the larger inertia of the
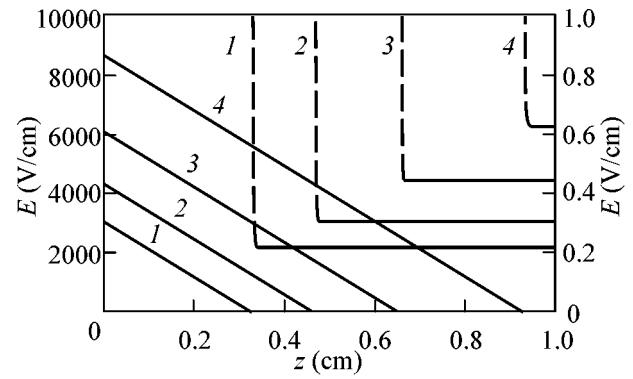
dust particles in the disklike structure, they occur in the region of strong electric fields that force them upward.

Let us estimate the electric force acting on the dust particles in the cathode layer, where the plasma quasineutrality is strongly violated. As was shown in [3], the electron distribution in the vicinity of a dust particle at low nitrogen ionization rates is well described by the Boltzmann distribution, while the ion flux on the dust particle obeys the Langevin expression. In this case, the following transcendental equation is obtained for determining the dust-particle charge with allowance made for the difference in the electron and ion concentrations in the cathode layer:

$$\pi r_0^2 n_{e0} v_{T,e} \exp\left(\frac{e\phi}{T_e}\right) = -4\pi e k_i q n_{i0}, \tag{7}$$

where r_0 is the dust-particle radius and n_{e0} and n_{i0} are, respectively, the electron and ion concentrations at a given point of cathode layer apart from the dust particle. On the assumption of a vacuum-type relation between the charge and potential, Eq. (7) can easily be solved by numerical methods.

The calculated dependences of dust-particle charges on their position are shown in Fig. 4a, which demonstrates the influence of the violation of plasma quasilinearity on the dust-particle charge. Near the cathode, which is almost free of electrons, the dust-particle charge becomes positive. In Fig. 4b, the electric forces acting on a dust particle with a radius of 1 μm in the cathode layer are shown as functions of height (gravity force is on the order of 10^{-8} dyne). It is seen that the force expelling the dust particles upward increases drastically in the cathode layer.

Figure 4b demonstrates how the potential well is formed for the dust particles in the cathode layer under the combined action of an electric field and gravity force in our experiments. Indeed, the electron-beam-induced gas ionization in the discharge gap is inhomogeneous, with the ionization rate being maximal at the
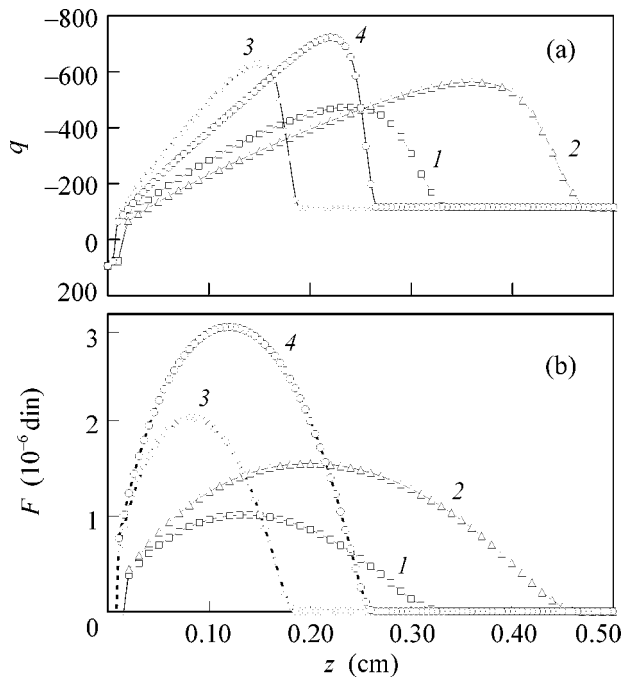
Fig. 4. The (a) charge and (b) electric force expelling the dust particles from the cathode as functions of the height at various voltages on the discharge gap and ionization rates in N_2 for $p = 1$ bar: (*1*) $U_d = 500$ V, $Q_{ion} = 10^{14}$ cm^{-3} s^{-1}, (*2*) $U_d = 1000$ V, $Q_{ion} = 10^{14}$ cm^{-3} s^{-1}; (*3*) $U_d = 500$ V, $Q_{ion} = 10^{15}$ cm^{-3} s^{-1}; and (*4*) $U_d = 1000$ V, $Q_{ion} = 10^{15}$ cm^{-3} s^{-1}.

center and decreasing toward the edges. One can see from Fig 4b that the equilibrium position rises with a decrease in the ionization rate, so that the potential energy of a dust particle in the gravitational field will increase upon its moving from the center to the periphery, resulting in the restoring force.

For now, we have not met with success in achieving quantitative agreement between the computational and experimental equilibrium positions of the dust-particle disklike structure that is determined by the balance of the electric and gravitational forces. In our experiments, gas was heated only slightly, so that the thermophoretic force acting on the dust particles was negligible. The radiometric force was also weak because of the smallness of the energy flux to the dust particles. The ion-drag force, which is directed against the ion flux at high pressures in the ion-transport collision regime because of taking away momentum from the dust particles and transfer it to the neutral-gas particles in collisions, is also small. The calculations with the addition of up to 1% oxygen to nitrogen did not change the current–voltage characteristics and the equilibrium position. The addition of oxygen gave rise to negative ions in the three-particle- and dissociative-attachment processes, which were taken into account by introducing

the third balance equation in the model for the negative ions. We believe that quantitative agreement between the calculation and experiment can be achieved only after correctly taking into account the influence of the dust component on the field distribution and electron-beam ionization loss, as well as after taking into account the gas ionization inhomogeneity in both height and horizontal. This requires, at least, two-dimensional calculations.

CONCLUSIONS

The study carried out in this work has demonstrated the possibility of formation of controlled dust structures at atmospheric pressure in fast-particle-controlled plasmas. Numerical simulation of a non-self-sustained gas discharge has shown that high electric fields arise due to the charge separation in the cathode layer. The combined action of electric and gravity fields forms potential well acting as a trap for the dust particles. This qualitatively explains the observed phenomenon.

REFERENCES

1. V. E. Fortov, A. G. Khrapak, S. A. Khrapak, *et al.*, Usp. Fiz. Nauk **174**, 495 (2004) [Phys. Usp. **47**, 447 (2004)].

2. V. Yu. Baranov, I. A. Belov, A. V. Dem'yanov, *et al.*, in *Isotopes*, Ed. by V. Yu. Baranov (IzdAT, Moscow, 2000) [in Russian].

3. A. F. Pal', D. V. Sivokhin, A. N. Starostin, *et al.*, Fiz. Plazmy **28**, 32 (2002) [Plasma Phys. Rep. **28**, 28 (2002)].

4. A. V. Filippov, N. A. Dyatko, A. F. Pal', and A. N. Starostin, Fiz. Plazmy **29**, 214 (2003) [Plasma Phys. Rep. **29**, 190 (2003)].

5. E. P. Velikhov, S. A. Golubev, Yu. K. Zemtsov, *et al.*, Zh. Éksp. Teor. Fiz. **65**, 543 (1973) [Sov. Phys. JETP **38**, 267 (1973)].

6. V. V. Zakharov, A. A. Karpikov, and B. V. Chekhunov, Zh. Tekh. Fiz. **46**, 1846 (1976) [Sov. Phys. Tech. Phys. **21**, 1074 (1976)].

7. S. A. Golubev, A. S. Kovalev, N. A. Loginov, *et al.*, Fiz. Plazmy **3**, 1011 (1977) [Sov. J. Plasma Phys. **3**, 558 (1977)].

8. V. V. Aleksandrov, V. P. Koterov, and A. M. Soroka, Zh. Vychisl. Mat. Mat. Fiz. **18**, 1214 (1978).

9. E. P. Velikhov, A. S. Kovalev, and A. T. Rakhimov, *Physical Phenomena in Gas Discharge Plasma* (Nauka, Moscow, 1987) [in Russian].

10. V. V. Aleksandrov, E. I. Glotov, V. A. Danilychev, *et al.*, Tr. Fiz. Inst. im. P. N. Lebedeva, Akad. Nauk SSSR **142**, 46 (1983).

Translated by V. Sakun

Unified Model of Pseudogap Features of Conductivity in HTSCs

K. D. Tséndin[1, *], D. V. Denisov[1], and B. P. Popov[2]

[1] *Ioffe Physicotechnical Institute, Russian Academy of Sciences, Politekhnicheskaya ul. 26, St. Petersburg, 194021 Russia*
* *e-mail: tsendin@mail.ioffe.ru*
[2] *St. Petersburg State Technical University, Politekhnicheskaya ul. 29, St. Petersburg, 195251 Russia*
Received April 6, 2004; in final form, June 15, 2004

The pseudogap phenomenon in underdoped and optimally oxygen-doped high-temperature superconductors (HTSCs) of the $Y_1Ba_2Cu_3O_x$ system is explained from a unified point of view within the model of negative U centers. It is shown that the pseudogap features of conductivity are not related directly to the superconductivity but arise due to the existence of statistical interaction of negative U centers with valence-band holes. Specifically due to this interaction, the hole density in the valence band does not remain constant. It differently changes with temperature for different mutual positions of the Fermi level and the valence band top. These differences lead to different temperature dependences of conductivity for underdoped and optimally doped samples. © 2004 MAIK "Nauka/Interperiodica".

PACS numbers: 71.30.+h; 74.20.-z

INTRODUCTION

The problem of pseudogap features in high-temperature superconductors (HTSCs) has been discussed for a long time [1]. These features can be observed experimentally in a number of quantities. Concerning the conductivity of oxygen-underdoped HTSCs, these features manifest themselves in the following way: in the temperature range immediately before the transition to the superconducting state, the temperature behavior of the conductivity has a semiconductor rather than metal character.

Some researches believe that such a temperature dependence of the conductivity in underdoped HTSC samples is related to the mechanisms of carrier scattering from the spin- or charge-density fluctuations. In this case, it is assumed that the Fermi level lies in the valence band; i.e., according to this interpretation, underdoped HTSCs are metals (although with low conductivity due to the strong scattering) rather than semiconductors.

In optimally oxygen-doped HTSCs, the pseudogap features of conductivity also manifest themselves in a deviation of the temperature dependence of resistivity from the linear dependence typical of metals. However, the deviation is of the other sign in comparison with underdoped HTSCs. With a decrease in temperature, the resistivity decreases faster than at high temperatures; i.e., an additional conductivity arises at low temperatures.

It is believed that this additional conductivity at temperatures above T_c indicates the presence of pairs that may contribute to the conductivity at temperatures close to T_c. This contribution is associated with the fluctuative coherence of pairs described by the Aslamazov–Larkin theory [2]. Thus, the pseudogap features of conductivity in underdoped and optimally doped HTSC samples are related to different mechanisms.

In this study, it will be shown that the pseudogap features of conductivity in underdoped and optimally doped HTSC samples can be naturally explained from a unified point of view within the model of negative U centers.

MODEL OF NEGATIVE U CENTERS

The model of negative U centers is based on the results obtained by Kulik and Pedan [3] and uses the Hubbard Hamiltonian with negative effective correlation energy:

$$H = -U\sum n_{i\uparrow}n_{i\downarrow} + \sum t_{ij}a_{i\sigma}^{+}\alpha_{j\sigma}, \qquad (1)$$

where $n_{i\sigma} = a_{i\sigma}^{+}a_{i\sigma}$ are the occupation numbers; $a_{i\sigma}^{+}$ and $a_{i\sigma}$ are, respectively, the operators of creation and annihilation of an electron with spin σ at site i; and t_{ij} is the transition matrix element between the neighboring localization centers (negative U centers); $U > 0$; and it is believed that $t_{ij} \ll -U$. Negative values of U lead to the attraction of electrons with opposite spins at the same site. It is assumed that their binding energy exceeds the ordinary Hubbard correlation energy of Coulomb interaction; i.e., the resulting $-U$ interaction in (1) is negative. At low temperatures, Hamiltonian (1) gives rise to a superconducting correlation between pairs.

In terms of delocalized electrons, the second term in Hamiltonian (1) corresponds to the kinetic energy of band motion, while the first term describes the attraction between electrons with the energy $-U$. In the BCS model, the band width is large, and, therefore, the inter-

action between electrons is regarded as a perturbation. In the model of negative U centers, the energy U is so high in comparison with t_{ij} that the second term in (1) is assumed to be small with respect to the first one. This is the main difference of the model under consideration from the BCS theory. Due to the inequality $U \gg t_{ij}$, the approximation used in [3] was referred to as approximation of localized pairs. However, it is clear that taking into account the second term in (1) is of basic importance for the manifestation of the transport properties of the system.

At $t_{ij} = 0$, the state of the system is a set of sites of three types: an empty site, a site occupied by one electron, and a site occupied by two electrons (D^+, D^0, and D^- states of negative U centers, respectively). The ionization energies of the D^- and D^0 states are denoted in Fig. 1 as E_1 and E_2, respectively. The perturbation associated with the second term in (1) (i.e., the $t_{ij} \neq 0$ situation) leads to the formation of delocalized band states of pairs and the D^+ and D^- states are split into two-particle (bosonic) transport bands (bands of negative U centers). In this case, the charge transfer from one negative U center to another occurs via two virtual one-electron transitions, so that the energy of the band motion of pairs is equal to t_{ij}^2/U [3].

The main difference of the model under consideration from the BCS theory is that the BCS theory assumes simultaneous formation of pairs and their transition to a condensed state at the temperature of superconducting transition. In the model of negative U centers, coupled pairs of electrons exist at temperatures far above room temperature and, at T_c, only their condensation occurs, leading to superconductivity.

APPLICABILITY OF THE MODEL

The model of negative U centers was developed initially to explain the superconductivity of chalcogenide glasses, since the presence of negative U centers with high concentrations in these systems was confirmed experimentally. After successful application of this model to chalcogenide glasses [4], it was used to describe the properties of HTSCs belonging to the YBaCuO system. Within this model, the high temperatures of the superconducting transition (T_c) were explained using real physical quantities. The value of T_c was estimated by formula (2) from [3]:

$$T_c = W(1 - 2\nu)/\ln(\nu^{-1} - 1), \qquad (2)$$

where W is the width of the two-particle transport band, which is equal to $2zt_{ij}^2/U$ for a simple cubic lattice composed of negative U centers (z is the number of nearest neighbors of one negative U center), and ν is a relative concentration of pairs equal to $n/2D$ (n is the electron density in the system of negative U centers and D is the concentration of negative U centers).
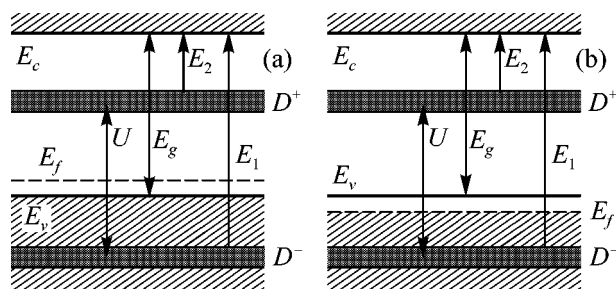
Fig. 1. Energy-band diagram of $Y_1Ba_2Cu_3O_x$. The D^+ and D^- bands of the states of negative U centers are shaded. (a) Underdoped samples, the Fermi level is above the valence band; (b) optimally doped and overdoped samples, the Fermi level lies in the valence band.
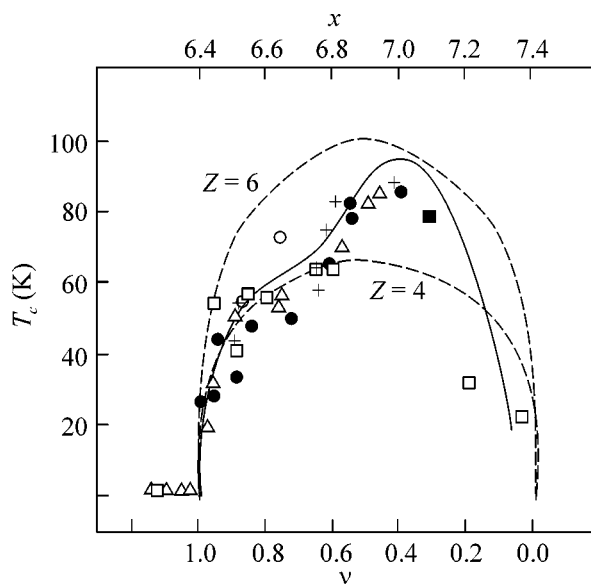

Fig. 2. Dependence of T_c on the oxygen content for $Y_1Ba_2Cu_3O_x$. The parameter ν is related to the oxygen content x by the formula $\nu = 7.4 - x$ [5]. References to the experimental studies are given also in [5].

According to (2), the dependence of T_c on ν is dome-shaped with a maximum at $\nu = 1/2$. When ν exceeds $1/2$, superconductivity occurs in the D^+ band, and when ν is smaller than $1/2$, superconductivity occurs in the D^- band. Therefore, as was shown in [5], formula (2) quite naturally explains the dome-shaped dependence of the superconducting-transition temperature on the doping level, as is observed experimentally for a number of HTSC systems. For example, the dome-shaped dependence of T_c on the oxygen content x for the YBaCuO system is shown in Fig. 2.

The following suggestions were made in [5]. First, negative U centers are complexes of copper atoms with their oxygen environment. Second, at a structural phase

transition in the YBaCuO system, a transition from $z = 4$ to $z = 6$ occurs in the system of negative U centers with an increase in the oxygen doping level. The theoretical dependences of T_c on x are shown by dashed lines for $z = 4$ and 6 and the total theoretical dependence of T_c on x corresponding to the transition from one dashed line to the other is shown by a solid line. The relation between the oxygen content x and the parameter ν from formula (2) was determined in [5] by the formula $\nu = 7.4 - x$.

In our opinion, the difference between the cuprate-based superconductors and classical BCS superconductors lies in the following: in the BCS theory, the conduction- (or valence-) band electrons located near the Fermi level form pairs at a superconducting transition, which serve afterward as superconducting charge carriers. In the model of negative U centers, the coupled pairs responsible for the superconductivity exist at temperatures much higher than the transition temperature. However, the effective mass of a coupled pair is so large that the mobility (and, therefore, the conductivity) of such particles in the normal state is negligible. Hence, the conductivity in the normal state is due to single holes or electrons. In YBaCuO, negative U centers capture some fraction of valence-band electrons that depends on the temperature and the doping level. The valence-band holes formed as a result of this process serve as charge carriers at temperatures above the transition point. Therefore, in contrast to the BCS theory, two types of carriers exist in the model of negative U centers: holes (or electrons) for a normal current and strongly coupled pairs for a superconducting current.

Let us consider now in more detail the situation with the pseudogap features of conductivity. In the late 1990s, an anomalous behavior of the energy spectrum above the superconducting transition temperature was revealed for some oxide-based HTSCs. It is well known that, when superconductivity occurs, a gap arises in the spectrum due to the formation of pairs and their condensation. However, in some (mainly underdoped) samples of oxide HTSCs, the gap in the spectrum remains at temperatures higher than the transition point. It has not been cleared up whether such a gap indicates the presence of residual superconductivity or not. Therefore, it is referred to as a pseudogap. There are several points of view on this problem.

Some researchers [1] believe that the pseudogap in HTSCs is similar to the mobility pseudogap in disordered semiconductors (in particular, in chalcogenide glasses). It is known that the band gap in chalcogenide glasses contains "tails" of the density of states from the valence and conduction bands. Due to these tails, the band gap may become very narrow and, in some cases, when the tails overlap, disappear. Since the mobility of charge carriers in these tails is zero at zero temperature and the density of states is finite, the corresponding energy interval is referred to as a pseudogap [6].

According to the other point of view, some fraction of pairs in the HTSCs under study exists in a coherent state at temperatures exceeding the superconducting temperature by tens and hundreds of K. It is believed that, due to these remaining pairs in a material, a superconducting gap arises in the spectrum. In addition, the superconductivity due to these pairs contributes to the conductivity of the material and, thus, efficiently decreases its resistivity (the additional conductivity effect) [7].

As can be seen, both these approaches in the explanation of the pseudogap origin are opposite in their physical nature and, when taken alone, can explain only the semiconductor behavior or the additional conductivity.

The approach to solving this problem in terms of the model of negative U centers made it possible to give a unified explanation of the pseudogap features of HTSCs.

Let us take into account the particular property of negative U centers that was revealed in chalcogenide glasses [8, 9]—their ability to pin the Fermi level. The pinning effect consists in the following: until the concentration of impurities in chalcogenide glasses does not exceed the concentration of negative U centers, the Fermi level always remains between the D^+ and D^- bands. This effect can also occur in HTSCs if the latter contain negative U centers.

It was assumed in [10] that the middle between the bands of negative U centers in underdoped samples lies slightly above the valence band top (Fig. 1a). As a result, the activation of one electron from the completely occupied valence band in the HTSCs under consideration requires an energy of several meV (i.e., the width of the gap between the valence band top and the middle between the bands of negative U centers) rather than an energy comparable with the band gap. In view of its smallness, this gap should manifest itself only at temperatures below 100–150 K, i.e., at temperatures on the order of T_c. Calculations performed by the effective-mass method [10] showed a good agreement between experiment and theory (Fig. 3), allowing us to conclude that the narrow gap between the valence band top and the middle between the bands of negative U centers is a pseudogap. Hence, it is clear that, in the model under consideration, the pseudogap in the underdoped $Y_1Ba_2Cu_3O_x$ has no superconducting character but is a real gap and is completely due to the property of negative U centers to pin the Fermi level in the middle between the D^+ and D^- bands (Fig. 1a).

PSEUDOGAP IN OPTIMALLY DOPED SAMPLES

Precise measurements of the temperature dependence of the resistivity showed that, for samples with oxygen content close to optimum, a deviation from the metal behavior of the conductivity occurs [7].

In the underdoped samples, the deviation of the temperature dependence of the resistivity is similar to that typical of semiconductors: the curve bends upward with a decrease in temperature (Fig. 3). In the optimally doped samples, in contrast, the curve bends downward at low temperatures (the so-called additional conductivity arises). Such an anomaly is also often associated with the manifestation of the pseudogap.

Let us show that the upward and downward bends of the curves have the same physical nature in the model of negative U centers and are due to the fact that the Fermi level (E_f) lies above the valence band top in the first case and lies in the valence band in the second case (Fig. 1). Taking into account the valence band, Hamiltonian (1) takes the form

$$H = E_2 \sum_{i\sigma} n_{i\sigma} - U \sum_i n_{i\uparrow} n_{i\downarrow} + \sum_k \varepsilon_k a_{k\uparrow}^+ a_{k\downarrow}. \quad (3)$$

where the last term accounts for the valence band.

In Hamiltonian (3), we ignore the term $\sum t_{ij} \alpha_{i\sigma}^+ a_{j\sigma}$, which describes the site-to-site electron transition, since this term is not important for the level-occupation statistics. We assume that valence-band electrons and negative U centers do not interact directly. Hence, Hamiltonian (3) describes two independent subsystems. In this case, the thermodynamic potential of the system can be considered a sum of two independent potentials: for the states of negative U centers and the valence-band states:

$$\Omega = \Omega_U + \Omega_v. \quad (4)$$

In the following expression, summation is over the states of negative U centers, which are described by the set of n_1 and n_2. Here, n_1 and n_2 correspond to the occupation of the negative U center by one electron and a pair of coupled electrons, respectively. The following situations with the occupation of negative U centers are possible: the absence of an electron at a center ($g = 1$, $n_1 = 0$, $n_2 = 0$), one electron at a center (energy level E_2 is doubly degenerate, $g = 2$, $n_1 = 1$, $n_2 = 0$), and a coupled pair at a center ($g = 1$, $n_1 = 2$, $n_2 = 1$). Since the energies are the same for all negative U centers and the total number of centers is D, we have

$$\Omega_U = -T \ln \left(\sum_{n_1, n_2} g(n_1, n_2) \right.$$

$$\left. \times \exp \left(\frac{\mu n_1 - n_1 E_2 - n_2 U}{T} \right) \right)^D$$

$$= -TD \ln \left(1 + 2 \exp \left(-\frac{E_2 - \mu}{T} \right) \right.$$

$$\left. + \exp \left(-\frac{2E_2 - U - 2\mu}{T} \right) \right). \quad (5)$$
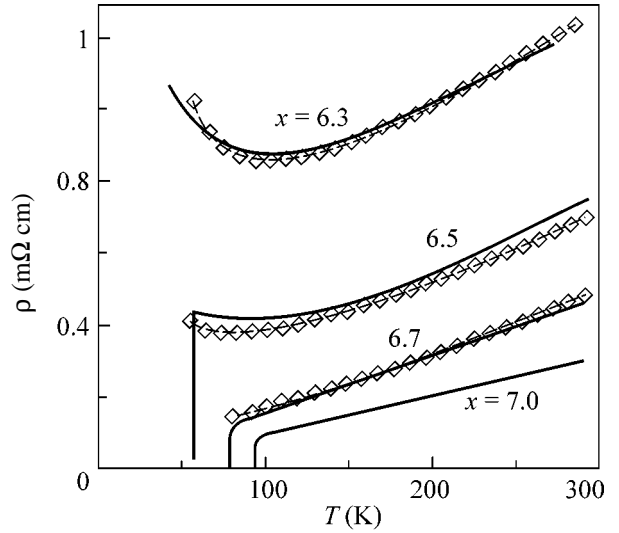
Fig. 3. Temperature dependences of resistivity. The experimental data for different oxygen contents are shown by solid lines [11]. The calculated dependences for underdoped samples are shown by diamonds [10].

The second term in Eq. (4) (Ω_v) corresponds to the valence band. Summation in this term is performed classically over two states (0 and 1). Summation over the valence-band states corresponding to different wave vectors $\mathbf{k}$ can be replaced by integration:

$$\Omega_v = \sum_k \Omega_k = \sum_k -T \ln \left(\sum_{n_k = 0, 1} \exp \left(\frac{\mu n_k - \varepsilon_k n_k}{T} \right) \right)$$

$$= -T \sum_k \ln \left(1 + \exp \left(-\frac{\varepsilon_k - \mu}{T} \right) \right) \quad (6)$$

$$= -T \int \ln \left(1 + \exp \left(-\frac{\varepsilon_k - \mu}{T} \right) \right) d\mathbf{k}.$$

Thus, the final expression for thermodynamic potential (4) can be written as

$$\Omega = -TD \ln (1 + 2e^{(E_2 - \mu)/T} + e^{(2E_2 - U - 2\mu)/T})$$

$$- T \int \ln (1 + e^{(\varepsilon_k - \mu)/T}) d\mathbf{k}. \quad (7)$$

Let us calculate the total electron density N in the system. The second term in Eq. (8) gives the electron Fermi distribution in the valence band. The first term in Eq. (8) corresponds to the number of electrons in the system of negative U centers:

$$N = -\frac{\partial \Omega}{\partial \mu} = D \frac{2e^{(E_2 - \mu)/T} + 2e^{(2E_2 - U - 2\mu)/T}}{1 + 2e^{(E_2 - \mu)/T} + e^{(2E_2 - U - 2\mu)/T}}$$

$$+ \int \frac{A\sqrt{E}}{1 + e^{(\mu - E)/T}} dE. \quad (8)$$

Expression (8) describes the particle distribution for the noninteracting systems of the valence band and negative U centers.

As was mentioned above, the energy U is so high that we can disregard the term $\exp(-(E_2 - \mu)/T)$, which is related to the single-electron density. Let us also pass to the relative concentration through dividing expression (8) by the doubled concentration $2D$ of negative U centers and take into account that the system under consideration is closed, i.e., the total electron density N is constant.

Since we disregarded single electrons in the system of negative U centers, the relative concentration ν of coupled pairs can change only due to a change in the relative electron density in the valence band. We can say that every two electrons that leave the valence band form a coupled pair at a center. In other words, the number of generated holes that are involved in the conduction is equal to the doubled number of pairs formed at negative U centers:

$$\Delta\nu \times 2D = \Delta p. \tag{9}$$

Let us consider in more detail the quantity $\Delta\nu$. The total pair density ν is determined by formula (10). A change in the pair density $\Delta\nu$ will be measured from the parameter ν_0, which determines the pair density specified by the chemical structure of the material. For $Y_1Ba_2Cu_3O_x$, this parameter is determined by the oxygen content, and we assume it to be known. If we disregard the valence band, ν coincides with ν_0:

$$\nu = \frac{n}{2D} = \frac{e^{(2E_2 - U - 2\mu)/T}}{1 + e^{(2E_2 - U - 2\mu)/T}} = \frac{1}{1 + e^{2((E_2 - U/2) - \mu)/T}},$$
$$\Delta\nu = \nu - \nu_0. \tag{10}$$

The number of holes can be calculated by integrating over the entire valence band:

$$p = \int_{E_{vb}}^{E_v} \frac{A\sqrt{E_v - E}}{1 + e^{\frac{\mu - E}{T}}} dE, \quad \Delta p = p. \tag{11}$$

Here, E_v and E_{vb} are the valence-band top and bottom, respectively. For simplicity, we assume that holes arise in the valence band only due to the escape of electrons to the system of negative U centers. Therefore, the absence of negative U centers implies the absence of holes in the valence band.

Combining Eqs. (9)–(11), we obtain the equation for the chemical potential μ:

$$\nu - \nu_0 - p/2D = 0 \longleftarrow \left(\frac{1}{1 + e^{2((E_2 - U/2) - \mu)/T}} \right)$$
$$- \left(\frac{A}{2D} \int_{E_{vb}}^{E_v} \frac{\sqrt{E_v - E}}{1 + e^{(\mu - E)/T}} dE \right) - \nu_0 = 0. \tag{12}$$

After finding the chemical potential μ from Eq. (12), we can calculate the hole density p in the valence band for a specified temperature by formula (11). If we know the hole density, it is easy to calculate the temperature dependence of the resistivity (13) of a material for different values of the parameter ν_0:

$$\rho(T, \nu_0) = \frac{mT^s}{p(T, \nu_0)}. \tag{13}$$

Here, m is a constant independent of temperature and s is a parameter dependent on the hole-scattering mechanism. The parameter s describes the temperature dependence of mobility.

When treating the results, we varied two parameters: A/D and $E_2 - U/2$. The parameter A/D is the ratio of the total density of states in the valence band to the concentration of negative U centers. The energy interval $E_2 - U/2$ determines the mutual position of the middle between the D^+ and D^- levels and the valence band top E_v. Figure 4 shows the results obtained with the following values: the total number of states in the valence band is about 2×10^{21} cm^{-3}, its width is 2 eV (a further increase in the width does not influence the result of calculation), the parameter s is 1.7, the concentration of negative U centers is 5×10^{19} cm^{-3}, and the pseudogap width $E_2 - U/2$ changes from 5.5 to -8 meV. Negative values of the pseudogap width correspond to the case where the Fermi level lies in the valence band (the valence band top is taken to be zero). The density of charge carriers (holes) in the valence band depends on both temperature and doping level. For example, for $x = 6.55$ ($E_2 - U/2 = 5.5$ meV), the valence band is completely occupied at zero temperature and the hole density is 1.3×10^{18} cm^{-3} at 300 K. For $x = 7.0$ ($E_2 - U/2 = -8$ meV), the hole density is 4.77×10^{17} and 4.69×10^{18} cm^{-3} at $T = 0$ and 300 K, respectively.

If the levels of negative U centers are located in such a way that the middle between them is by more than 1 meV above the valence band, the material behaves as a semiconductor near the superconducting transition temperature (the upward pseudogap bend; solid lines in Fig. 4).

If the middle between the levels of negative U centers lies in the valence band (near the top), the resistivity curve bends downward (Fig. 4).

The latter effect can be explained as follows. When the middle between the levels of negative U centers (and, therefore, the Fermi level at zero temperature) enters the valence band, all electrons above the Fermi level pass to negative U centers at zero temperature, giving rise to holes with density p_0. At low temperatures, the slope of the resistivity curve is mainly determined by the ratio $1/p_0$.

At higher temperatures, the number of electrons passed from the valence band to negative U centers increases; therefore, p increases and slope of the
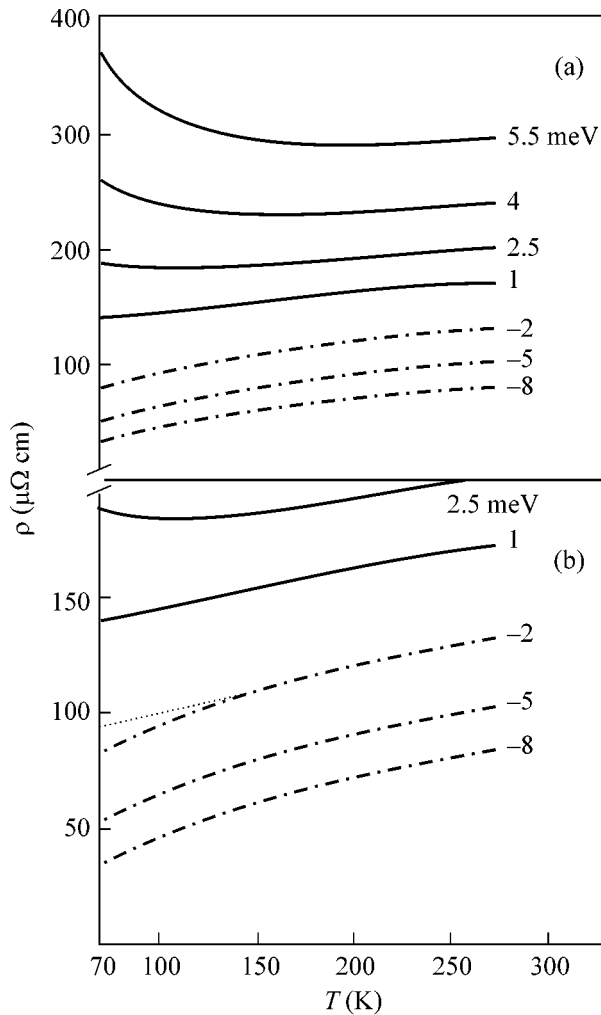
Fig. 4. Resistivity as a function of the oxygen content. The values of the pseudogap width are indicated on the right. Negative values mean that the Fermi level lies in the valence band (dash-and-dot curves). The occurrence of additional conductivity is shown on an enlarged scale (b). For clearness, the metallic behavior (without an additional conductivity) is shown for one of the curves (−2 meV) by the dotted line.

Fig. 5. Position of the Fermi level as a function of the oxygen content in $Y_1Ba_2Cu_3O_x$. The parameter ν_0 is related to x by the formula $\nu_0 = 7.4 - x$ [5]. Shaded area indicates the filling of the valence band by electrons. As the Fermi level penetrates the valence band, the electrons located above the Fermi level pass to negative U centers.

YBaCuO system and the additional conductivity occurring at optimal doping, we derived the position of the Fermi level at $T = 0$ K as a function of the oxygen content (Fig. 5). The change in the Fermi-level position is confirmed by the increase in the conductivity of HTSCs with increasing the doping level. Indeed, at a higher oxygen content, the Fermi level penetrates deeper into the valence band, thereby increasing the density of holes responsible for the conductivity. Figure 2 shows the dependence on ν rather than ν_0, as in Fig. 5. The reason is as follows: by the time when the data shown in Fig. 2 were obtained, the effect of the valence band had not been taken into account and, in this case, ν and ν_0 coincide.

CONCLUSIONS

The pseudogap phenomenon in underdoped and optimally oxygen-doped HTSC samples of the $Y_1Ba_2Cu_3O_x$ system is explained from the unified positions within the model of negative U centers. In the model of negative U centers, the superconductivity is due to the D^+ and D^- bands of states of negative U centers, while the valence-band holes are responsible for the conducting properties in the normal state.

It is shown that the pseudogap features of conductivity are not associated directly with the superconductivity but appear due to the existence of statistical interaction between the negative U centers and the valence-band holes. It is due to this interaction that the hole density in the valence band does not remain constant. Its

dependence $\rho(T)$, which is approximately determined by the ratio $1/p$, decreases (13). The lower the initial hole density p_0, the more pronounced the difference between the two slopes. Therefore, the anomalous situation with the downward bends of the resistivity curves is most pronounced for the samples where the Fermi level lies not very deep in the valence band (Fig. 4b). At the same time, at very small values of p_0, the resistivity curve $1/p_0$ does not show a steeper slopes since it should arise at temperatures below the temperature of superconducting transition. In other words, the effect of additional conductivity will be practically unobservable in this case.

Having analyzed the situation with the semiconductor behavior of oxygen-underdoped HTSCs of the
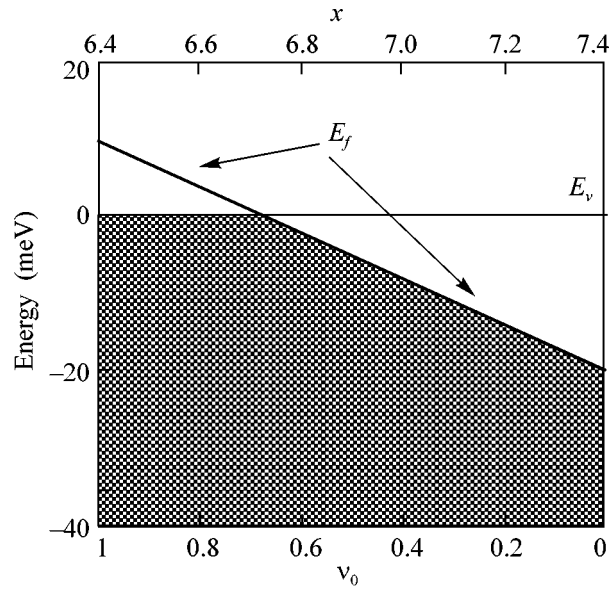
changes with a change in temperature are different for different mutual positions of the Fermi level and the valence band top. These differences lead to the difference in the temperature dependences of conductivity in underdoped and optimally doped samples. Thus, the assumption made in the model of negative U centers that two types of charge carriers exist in HTSCs at temperatures above the superconducting transition (pairs of coupled electrons (holes) and single holes) was confirmed by the calculations of the conductivity of HTSCs in the normal state.

REFERENCES

1. M. V. Sadovskii, Usp. Fiz. Nauk **171**, 539 (2001) [Phys. Usp. **44**, 515 (2001)].
2. L. G. Aslamazov and A. I. Larkin, Phys. Lett. A **26A**, 238 (1978).
3. I. O. Kulik and A. G. Pedan, Zh. Éksp. Teor. Fiz. **79**, 1469 (1980) [Sov. Phys. JETP **52**, 742 (1980)].
4. K. D. Tséndin and B. P. Popov, Pis'ma Zh. Tekh. Fiz. **24** (7), 45 (1998) [Tech. Phys. Lett. **24**, 265 (1998)].
5. K. D. Tsendin and B. P. Popov, Supercond. Sci. Technol. **12**, 255 (1999).
6. N. F. Mott and E. A. Davis, *Electron Processes in Non-Crystalline Materials* (Clarendon Press, Oxford, 1974; Mir, Moscow, 1979).
7. D. D. Prokof'ev, M. P. Volkov, and Yu. A. Boĭkov, Fiz. Tverd. Tela (St. Petersburg) **45**, 1168 (2003) [Phys. Solid State **45**, 1223 (2003)].
8. D. Adler and E. F. Yoffa, Phys. Rev. Lett. **36**, 1197 (1976).
9. P. W. Anderson, Phys. Rev. **109**, 1492 (1975).
10. K. D. Tsendin and D. V. Denisov, Supercond. Sci. Technol. **16**, 80 (2003).
11. S. Tanaka, S. Uchida, H. Takagi, *et al.*, Int. J. Mod. Phys. B **1**, 755 (1987).

Translated by Yu. Sin'kov

Anomalous Charge Transfer in La_2CuO_4 near the Néel Temperature: Evidence of the Transition from Spin Liquid to Two-Sublattice Antiferromagnetic State

O. E. Parfenov* and A. A. Nikonov

Russian Research Centre Kurchatov Institute, Moscow, 123182 Russia
*e-mail: parfenov@isssph.kiae.ru
Received June 22, 2004

The temperature dependence of the electrical resistance and thermopower of $La_{2-x}Sr_xCuO_{4+\delta}$ single crystals with $x \cong 0.003$ and $\delta < 0.05$ has been studied in the temperature range from 100 to 400 K. All crystals exhibiting two-dimensional hopping conductivity via neighboring acceptor sites in the CuO_2 plane show a significant difference in the charge transfer below and above the Néel temperature T_N. This difference indicates that the loss of a two-sublattice antiferromagnetic order strongly affects the charge transport in the CuO_2 plane. The obtained data lead to a conclusion that the crystal above T_N occurs in a resonance valence bond state of the Bose type. © 2004 MAIK "Nauka/Interperiodica".

PACS numbers: 74.25.Fy; 74.72.Dn; 75.50.Pp

Undoped cuprate high-T_c superconductors belong to the class of Mott insulators and offer a good example of realization (with small deviations from the exact model) of two-dimensional (2D) spin 1/2 quantum Heisenberg antiferromagnets on a square lattice [1] with a large exchange coupling constant ($J_\parallel \approx 1600$ K). The problem of determining the ground state of such 2D quantum antiferromagnets is still unsolved. A 2D quantum Heizenberg antiferromagnet on a square lattice may have both a Néel ground state (corresponding to a two-sublattice spin crystal) and some other spin states realized primarily in the form of a spin liquid [2]. Spin liquids are subdivided according to the type of low-energy spin excitations representing resonance valence bond (RVB) states: Bose-RVB [3] versus Fermi-RVB [4].

There is experimental evidence [1] that, in slightly doped cuprate high-T_c superconductors at low temperatures, the magnetic system of copper in the CuO_2 plane corresponds to an antiferromagnetic lattice with a long-range order. However, the observed 3D antiferromagnetic order is caused by weak non-Heiseberg spin interactions: interplane interaction with $J_\perp/J_\parallel \sim 10^{-5}$ and anisotropic interaction in the CuO_2 plane with $J_{xy}/J_\parallel \sim 10^{-4}$. The results of neutron investigations [1, 5] of the temperature dependence of the correlation length in La_2CuO_4 showed that the magnetic spin system of copper above the Néel temperature ($T > T_N$) occurs in the regime of low-temperature renormalized classical fluctuations. Theoretically, this result is equally well described by the model of spin crystal [6] and the models of spin liquids in both Bose-RVB [7] and Fermi-RVB [8] states. However, the spin crystal and spin liquid are characterized by essentially different magnetic excitations. Obtained by the method of inelastic neutron scattering [1, 8], the experimental data on magnetic excitations in the entire Brillouin zone of La_2CuO_4 showed that the spin-excitation dispersion curves are well described both by the theory of spin waves with allowance made for quantum fluctuations and by the models of spin liquids in Bose-RVB [9] and Fermi-RVB [10] states. Only the data on Raman scattering and IR absorption in cuprates are much better described by the RVB theory [10]. Therefore, it is important to continue the search for new experimental facts elucidating the magnetic properties of cuprate high-T_c superconductors in the Mott insulator state.

As is known [11–13], a hole introduced into the CuO_2 plane exhibits different responses to the Néel spin crystal, Bose-RVB, and Fermi-RVB states. It is expected that, due to a large correlation length of antiferromagnetic fluctuations (several hundreds of angströms near the Néel temperature) [5], anomalies in the charge transfer will be manifested only during the transition from spin crystal to spin liquid. Earlier [14], we observed a significant difference in the behavior of the charge-transfer characteristics above and below T_N for the $La_2CuO_{4+\delta}$ crystals with $T_N > 310$ K (Fig. 1). However, the $La_2CuO_{4+\delta}$ crystals with $T_N < 300$ K exhibited a hysteresis caused by the oxygen mobility. Thus, in the above context, it would be of interest to study the charge-transfer process in the $La_{2-x}Sr_xCuO_4$ crystals free of the effects associated with the dopant mobility.

We have studied $La_{2-x}Sr_xCuO_{4+\delta}$ single crystals grown by spontaneous crystallization in the course of slow (2–3 K/h) cooling of a solution melt in a zirconia
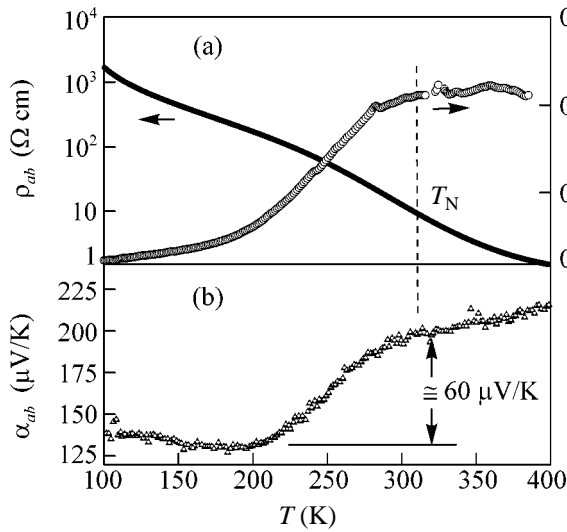
Fig. 1. Temperature dependences of (a) the electrical resistance $\rho_{ab}(T)$ and the local conductivity activation energy $E_{ab}(T) = d(\ln(\rho_{ab}(T))/d(T^{-1})$ and (b) the thermopower $\alpha_{ab}(T)$ measured in the CuO$_2$ plane of a La$_2$CuO$_{4.0013}$ crystal with $T_N = 315$ K.
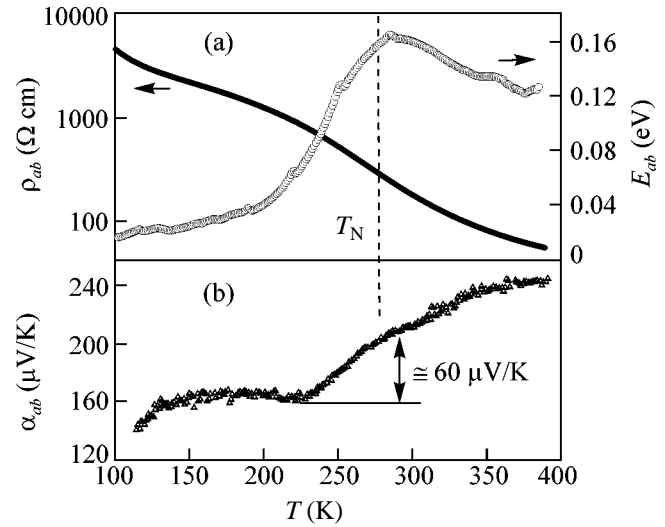

Fig. 2. Temperature dependences of (a) the electrical resistance $\rho_{ab}(T)$ and the local conductivity activation energy $E_{ab}(T)$ and (b) the thermopower $\alpha_{ab}(T)$ measured in the CuO$_2$ plane of a La$_{1.997}$Sr$_{0.003}$CuO$_4$ crystal with $T_N = 275$ K.

crucible. The crystals mechanically extracted from the crucible had the shape of plates and pyramids with a characteristic size of 1–5 mm and a mass of 1–15 mg. The crystal orientation, lattice parameters, and mosaicity were studied by X-ray single-crystal diffractometry. It was established that the sample mosaicity along the *c* axis did not exceed 0.05°. Superstoichiometric oxygen was removed by annealing in vacuum at a temperature of ≤950 K and a partial pressure of oxygen <2 × 10^{-5} bar. The lattice parameters of the grown crystals corresponded to the published data for the La$_2$CuO$_4$ system. Using the well-known concentration dependences of the lattice parameter *c* for the La$_2$CuO$_4$ crystals doped with oxygen [15] and strontium [16], the absolute concentrations of oxygen and strontium were determined according to Vegard's law with an error not exceeding 20%.

The charge transport in single crystals was studied by the standard dc techniques using the samples with ohmic contacts formed by firing a silver paste. The temperature dependence of the electrical resistance was studied by measuring currents in the *ab* plane and along the *c* axis. Over the entire temperature range studied (100–400 K), the anisotropy (ρ_c/ρ_{ab}) varied within 10^2–10^4; for this reason, the charge-carrier transport in the CuO$_2$ plane is considered below as two-dimensional. The results of measurements of the electrical resistance of antiferromagnetic semiconductors with hopping conductivity [17, 18] showed that anomalies in the vicinity of T_N, if observed, had the form of weakly pronounced bending points on the curves in the $\ln(\rho(T))$ versus $1/T$ coordinates. For this reason, we performed

measurements (similar to [14]) of $\rho_{ab}(T)$ with a precision that was sufficient for determining the local conductivity-activation energy $E_{ab}(T) = d\ln(\rho_{ab}(T))/d(T^{-1})$ (see Figs. 1a–3a). Simultaneously, we also measured the thermopower $\alpha_{ab}(T)$ (see Figs. 1b–3b).

The Néel temperature T_N of the crystals studied was determined by measuring the position of the maximum
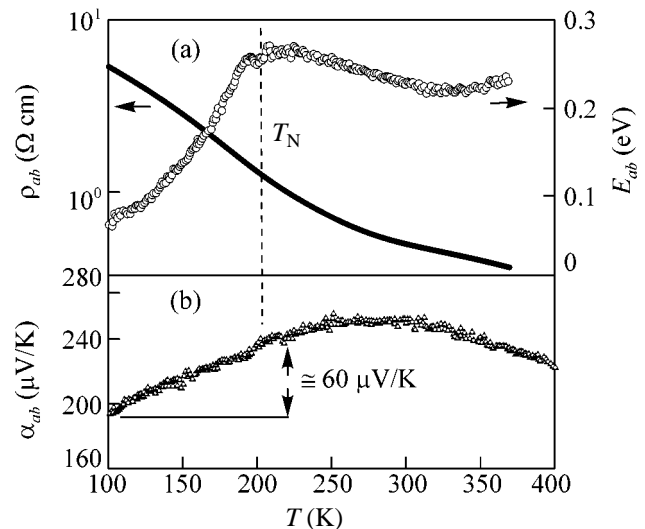

Fig. 3. Temperature dependences of (a) the electrical resistance $\rho_{ab}(T)$ and the local conductivity activation energy $E_{ab}(T)$ and (b) the thermopower $\alpha_{ab}(T)$ measured in the CuO$_2$ plane of a La$_{1.997}$Sr$_{0.003}$CuO$_{4.005}$ crystal with $T_N = 200$ K.

in the differential magnetic susceptibility $\chi_\perp(T) = dM_c/dH_\perp$, thanks to a hidden weak ferromagnetism with the Dzyaloshinski–Moria interaction ($J_{DM}/J_\parallel \approx 10^{-2}$). The uncertainty in the T_N determination by this method was within ±5 K.

The results of measurements of the transport properties of $La_{1.997}Sr_{0.003}CuO_4$ and $La_{1.997}Sr_{0.003}CuO_{4.005}$ were close to the data obtained for $La_2CuO_{4+\delta}$ single crystals doped only with oxygen to $\delta < 0.0015$. The observed anomalies in the charge-transfer near the Néel temperature show that the loss of a two-sublattice antiferromagnetic order strongly affects the charge transport in the CuO_2 plane. Above T_N, there is a strong charge-carrier localization. When the temperature is decreased below T_N, the local activation energy $E_{ab}(T) = d(\ln\rho_{ab}(T))/d(T^{-1})$ decreases by several times (Fig. 4a). An increase in the temperature above T_N gives rise to a "paramagnetic" spin contribution to the thermopower: $\Delta\alpha_{ab} = (e/k)\ln 2 \approx 60\ \mu V/K$ (Figs. 2b and 3b).

In order to elucidate the nature of anomalies observed in the charge-transfer characteristics, we consider some important features of this transport in the crystals studied near the Néel temperature. A comparison of the two temperature dependences, $E_{ab}(T)$ and $\alpha_{ab}(T)$, indicates that the thermopower α does not contain an activation contribution $E_{ab}(T)/T$. For this reason, we can ascertain (see, e.g., [17–19]) that the charge transport proceeds by hopping at the Fermi level and a decisive contribution to $E_{ab}(T)$ comes from the polaron effect. For the crystals slightly doped with oxygen, it was demonstrated [14] that the polaron effect is manifested by the lattice distortion caused by a hole localized at the acceptor, which forms a deep (~1 eV) impurity level in the ~2-eV bandgap. In a sample doped with both oxygen and strontium (Fig. 3b), the thermopower $\alpha_{ab}(T)$ at $T > T_N$ exhibits a weak temperature dependence, indicative of the proximity of the impurity levels of Sr and O. In all samples studied in the temperature range 100–400 K, the behavior of the conductivity and thermopower outside the region of anomalies was characteristic of the charge-carrier transport by hopping between the neighboring impurity centers [19]. Here, the impurity center is not analogous to the Zhang–Rice singlet but, rather, represents a well-defined cluster comprising a hole (localized at the oxygen atom) and a small number of copper spins with a total spin of 1/2. This structure was predicted theoretically (see [20, 21] and references therein) and confirmed in experiment [14, 21].

In order to establish the nature of relations between the anomalies in the charge-transfer characteristics and the changes in the magnetic spin system of copper, it is important to compare the scale ξ_{AF} of antiferromagnetic fluctuations and the average distance d_{ab} between the neighboring impurity centers: $d_{ab} \cong 3.8/(x + 2\delta)^{1/2}$ Å (Fig. 4b). Let us compare the values of d_{ab} with the cor-
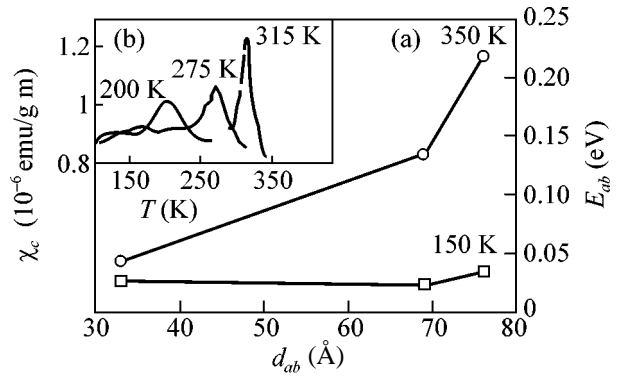

Fig. 4. Plots of (a) the local conductivity activation energy $E_{ab}(T)$ at $T = 350$ and 150 K vs. the distance d_{ab} between the neighboring acceptor centers and (b) the magnetic susceptibility $\chi_c(T)$ vs. temperature T for $La_{1.997}Sr_{0.003}CuO_{4.005}$ ($T_N = 200$ K), $La_{1.997}Sr_{0.003}CuO_4$ ($T_N = 275$ K), and $La_2CuO_{4.0013}$ ($T_N = 315$ K) crystals.

relation length ξ_{AF} of antiferromagnetic fluctuations determined from the results of neutron scattering measurements at various temperatures [5, 22, 23] for La_2CuO_4 crystals with various T_N values within 195–325 K. For a crystal with $T_N = 325$ K [5], $\xi_{AF}(400\ K) \approx 270$ Å and $\xi_{AF}(330\ K) \geq 600$ Å, while, for a sample with $T_N = 195$ K [23], $\xi_{AF}(400\ K) \approx 80$ Å and $\xi_{AF}(195\ K) \approx 400$ Å. Thus, for $T \leq 400$ K, the average distance d_{ab} between the neighboring impurity centers in our samples is always smaller than the correlation length of antiferromagnetic fluctuations. If the observed antiferromagnetic fluctuations reflect the formation of the Néel order, we can hardly expect any change in the charge transport in the CuO_2 plane upon the appearance of a long-range magnetic order.

Of special interest is the study of the behavior of the thermopower $\alpha(T)$ in the crystals with hopping conductivity in the region of magnetic transitions [19]. The thermopower in crystals with hopping polaron transport is usually considered [24] in terms of the entropy change (per unit charge $-e$) caused by various factors involved in the charge transport. For the diffusion part of the thermopower, we have $e\alpha(T) = \Delta S_C + \Delta S_M$, where ΔS_C is a change in the configuration entropy for a spinless particle and ΔS_M is the change in the magnetic entropy. For all Fermi-glass systems, Mott [19] suggested that the thermopower in the case of charge hopping above T_N must contain the component $\Delta S_M = k\ln 2$ caused by the free spins of impurity states.

In La_2CuO_4 below T_N, the interaction of the ith impurity cluster (having the spin $\sigma_i = 1/2$) with the antiferromagnetic environment involves two contributions [21] reflecting the exchange interaction (with $J_i \approx J_\parallel$) and the Dzyaloshinski–Moria interaction ($J_i \sim J_{DM}$). In the molecular-field approximation,

$$H_i \approx \sigma_i(J_i \cdot \mathbf{m}_i + [\mathbf{m}_i \cdot \boldsymbol{\omega}_i]), \qquad (1)$$

where $\mathbf{m}_i$ is the vector of magnetic-moment density near the ith acceptor and $\boldsymbol{\omega}_i$ is the vector of local rhombicity enhanced due to the polaron effect. At $T < T_N$, in the system with a strong lattice polaron effect like that observed in our slightly doped La_2CuO_4 crystals (~0.1 eV), we have $H_i \gg kT_N$. Then, the spin of an impurity cluster is associated with the antiferromagnetic sublattice and its contribution to the magnetic entropy is negligibly small.

Above T_N, taking into account well-developed 2D antiferromagnetic fluctuations with $\xi_{AF} \sim 100$ Å, the interaction of the ith impurity cluster with an antiferromagnetic environment can be described by relation (1) with the magnetic-moment density vector replaced by its statistical average $\langle \mathbf{m}_i \rangle$ over the time $\tau_s \sim \hbar/kT \approx 3 \times 10^{-14}$ s ($T \approx 300$ K) of the spin thermal fluctuations of the impurity hole. If the antiferromagnetic fluctuations above T_N are fluctuations of the Néel order parameter, the characteristic fluctuation time of the $\mathbf{m}_i$ vector on the correlation length ξ_{AF} is $\xi_{AF} : \tau_{AF} \approx 1/\omega_{AF} \approx 10^{-12}$–$10^{-13}$ s, where $\hbar\omega_{AF}$ is the characteristic energy of antiferromagnetic fluctuations (in La_2CuO_4, $\hbar\omega_{AF} \approx 0.02(T)^{1/2}/\xi_{AF}$ eV [5]). Thus, τ_{AF} is greater by more than an order of magnitude than the characteristic time τ_s of spin thermal fluctuations of the impurity hole. Therefore, the fluctuations of the Néel order parameter are quasi-stationary, and $\langle \mathbf{m}_i \rangle \approx \mathbf{m}_i$. In this case, interaction (1) exceeds the Néel temperature and, hence, the spin of the impurity cluster is associated with the copper spins, and the magnetic contribution $\Delta S_M/e$ must not be manifested in the thermopower.

A different situation takes place for La_2CuO_4 in the spin liquid state [4, 13], where most pairs of the neighboring copper spins are fixed only within $\tau_{RVB} \sim \hbar/J_\| \approx 5 \times 10^{-15}$ s. This value is an order of magnitude smaller than the time of thermal fluctuations of the impurity cluster spin and, hence, $\langle \mathbf{m}_i \rangle \approx 0$ and $H_i \approx 0$. Thus, the spin of an impurity hole becomes free upon the "3D Néel ferromagnet $\longrightarrow$ 2D spin liquid" transition and the thermopower acquires the magnetic contribution $\Delta S_M/e = k/e \ln 2 \approx 60$ μV/K due to the impurity paramagnetism—just what was observed in our experiments (see Figs. 1b–3b).

It is difficult to explain the observed strong decrease in the activation energy of hopping conductivity at $T < T_N$ (Fig. 1a–4a) within the framework of the usual hopping-transport model, where the probability of a jump to the neighboring impurity center (with allowance made for the quantum effects [25]) weakly depends on the magnetic state of these centers. However, it should be noted (Fig. 4a) that both the local conductivity activation energy $E_{ab}(T > T_N)$ and its change $\Delta E_{ab} = E_{ab}(350 \text{ K}) - E_{ab}(150 \text{ K})$ strongly depend on the distance between the neighboring impurity clusters. This can be explained by relating the lattice polaron effect to the influence of a magnetic string appearing during the

jump of a hole. According to the results of our thermopower measurements, the activation energy is mostly determined by the polaron effect. Therefore, we can assume that $E_{ab}(T) \approx W_p(T)$, where $W_p(T)$ is the lattice polarization energy [19]:

$$W_p(T) = e^2/(4\varepsilon_p)(1/r_p - 1/d_{ab}). \qquad (2)$$

Here, r_p is the localization radius of the impurity state (hole) and $1/\varepsilon_p = 1/\varepsilon_\infty - 1/\varepsilon_0$ is the difference between the inverse optical and static dielectric constants for the slightly doped La_2CuO_4 ($1/\varepsilon_p \approx 1/6$ [22]). Upon hole tunneling to the neighboring impurity center, a "virtual" string of frustrated antiferromagnetic bonds is formed behind the hole. The mechanism of an additional hole localization consists in this string effect. In the Néel antiferromagnet and the Fermi-RVB state, the string of frustrated bonds is healed by the exchange interaction due to the transverse copper spin fluctuations, after which the hole acquires a finite mobility. In the Bose-RVB state [3, 12, 13], there are long-range antiferromagnetic pair correlations in addition to the short-range correlations. Because of the short-range exchange, the long-range frustrated correlations are not healed and the probability of a jump to the neighboring impurity center decreases. The probability of hole tunneling from a filled acceptor center to an empty center exponentially depends on the hopping distance and, hence, on the string length and the number of unhealed bonds. This results in a decrease of the localization radius r_p of the impurity state and, according to formula (2), to an increase in the local activation energy $E_{ab}(T)$.

Thus, the results of our measurements of the electrical resistance and thermopower in a La_2CuO_4 weakly doped with oxygen and strontium showed that an additional charge-carrier localization takes place at temperatures above T_N. A decrease in the temperature in the vicinity of T_N leads to the disappearance of the magnetic contribution to the thermopower, which is probably due to the formation of a magnetic polaron state below T_N [26]. Analysis of the obtained experimental data leads to the conclusion that La_2CuO_4 above the Néel temperature occurs in the state of spin liquid with resonance valence bonds of the Bose type.

REFERENCES

1. E. Manousakis, Rev. Mod. Phys. **63**, 1 (1991).
2. S. Liang, B. Doucot, and P. W. Anderson, Phys. Rev. Lett. **61**, 365 (1988).
3. Y. C. Chen and Z. Y. Weng, Phys. Rev. B **53**, 289 (1996).
4. P. W. Anderson, Science **235**, 1196 (1987).
5. R. J. Birgeneau, M. Greven, M. A. Kastner, *et al.*, Phys. Rev. B **59**, 13788 (1999).

6. S. Chakravarty, B. I. Halperin, and D. R. Nelson, Phys. Rev. B **39**, 2344 (1989).

7. A. Auerbach and D. P. Arovas, Phys. Rev. Lett. **61**, 617 (1988).

8. S. I. Belov and B. I. Kochelaev, Solid State Commun. **103**, 249 (1997).

9. R. Coldea, S. M. Hayden, G. Aeppli, *et al.*, Phys. Rev. Lett. **86**, 5377 (2001).

10. C. M. Ho, V. N. Muthukumar, M. Ogata, and P. W. Anderson, Phys. Rev. Lett. **86**, 1626 (2001).

11. R. Hayn, A. F. Barabanov, J. Schulenburg, and J. Richter, Phys. Rev. B **53**, 11714 (1996).

12. D. N. Sheng, Y. C. Chen, and Z. Y. Weng, Phys. Rev. Lett. **77**, 5102 (1996).

13. Z. Y. Weng, V. N. Muthukumar, D. N. Sheng, and C. S. Ting, Phys. Rev. B **63**, 075 102 (2001).

14. O. E. Parfenov, A. A. Nikonov, and S. N. Barilo, Pis'ma Zh. Éksp. Teor. Fiz. **76**, 719 (2002) [JETP Lett. **76**, 616 (2002)].

15. J. C. Grenier, N. Laqueyte, A. Wattiaux, *et al.*, Physica C (Amsterdam) **202**, 209 (1992).

16. S. Wakimoto, S. Ueki, Y. Endoh, and K. Yamada, Phys. Rev. B **62**, 3547 (2000).

17. *Polarons*, Ed. by Yu. A. Firsov (Nauka, Moscow, 1975) [in Russian].

18. A. A. Samokhvalov, N. A. Viglin, B. A. Gizhevskiǐ, *et al.*, Zh. Éksp. Teor. Fiz. **103**, 951 (1993) [JETP **76**, 463 (1993)].

19. N. F. Mott and E. A. Davis, *Electronic Processes in Non-Crystalline Materials*, 2nd ed. (Clarendon Press, Oxford, 1979; Mir, Moscow, 1982).

20. K. J. von Szczerpanski, T. M. Rice, and F. G. Zhang, Europhys. Lett. **8**, 797 (1989); K. M. Rabe and R. N. Bhatt, J. Appl. Phys. **69**, 4508 (1991).

21. A. O. Gogolin and A. S. Ioselevich, Zh. Éksp. Teor. Fiz. **98**, 681 (1990) [Sov. Phys. JETP **71**, 380 (1990)]; Pis'ma Zh. Éksp. Teor. Fiz. **51**, 154 (1990) [JETP Lett. **51**, 174 (1990)].

22. M. A. Kastner, R. J. Birgenau, G. Shirane, and Y. Endoh, Rev. Mod. Phys. **70**, 897 (1998).

23. Y. Endoh, K. Yamada, R. J. Birgeneau, *et al.*, Phys. Rev. B **37**, 7443 (1988).

24. D. Emin, Phys. Rev. B **59**, 6205 (1999).

25. W. F. Brinkman and T. M. Rice, Phys. Rev. B **2**, 1324 (1970).

26. L. A. Maksimov, A. F. Barabanov, E. Zasinas, and O. V. Urazaev, Pis'ma Zh. Éksp. Teor. Fiz. **66**, 173 (1997) [JETP Lett. **66**, 182 (1997)].

Translated by P. Pozdeev

Study of Ferroelectric Switching by Domain-Wall Induced Light Scattering[¶]

D. V. Isakov[1], T. R. Volk[1],*, L. I. Ivleva[2], K. Betzler[3], C. David[3], A. Tunyagi[3], and M. Wöhlecke[3]

[1] *Institute of Crystallography, Russian Academy of Sciences, Moscow, 119333 Russia*
[2] *Institute of General Physics, Russian Academy of Sciences, Moscow, 117942 Russia*
[3] *Fachbereich Physik, Universität Osnabrück, D-49069 Osnabrück, Germany*
*e-mail: volk@ns.crys.ras.ru
Received July 13, 2004

Measurements of 90°-scattering of weak laser light are used to investigate pulsed domain switching in ferroelectrics. The studies were performed on strontium–barium niobate (SBN) single crystals. A good agreement of the switching parameters estimated from the optical measurements with those obtained by means of conventional electrical methods proves the validity of the optical method for switching studies. Due to the limited scattering volume in all three spatial dimensions, the method facilitates local probing of the switching within the crystal bulk. In particular, local specialities of the domain density can be detected. Furthermore, the excellent time resolution inherent in optical probing techniques allows for a comprehensive study of the dynamics. © 2004 MAIK "Nauka/Interperiodica".

PACS numbers: 77.80.Fm; 77.84.Dy; 78.35.+c

Studies in ferroelectric switching are at present taking on special significance in light of developing optical frequency conversion in the quasi-phase matching (QPM) mode of operation on periodically poled, i.e., regular domain structures (RDS) in ferroelectrics. The ferroelectric solid solution $Sr_xBa_{1-x}Nb_2O_6$ (SBN-x) represents a material appropriate for these purposes due to its relatively high nonlinear-optical susceptibilities [1] and rather low coercive fields $E_c \propto 10^3$ V/cm. Two successful attempts at optical frequency conversion on RDS in SBN crystals have been reported [2, 3]. Manufacturing RDS requires studies of ferroelectric properties, particularly of ferroelectric switching. However, there are only a few publications devoted to direct studies of the polarization process in SBN [4–7]. The results of [4, 5] were obtained under quasistatic (slowly varying) fields; switching under pulsed fields was observed by means of the conventional method of switching currents [6, 7].

In the present work, we report—for the first time, to our knowledge—on investigations of the ferroelectric switching of SBN crystals performed by means of light scattering measurements at domain walls. This method provides certain advantages over electrical methods, because it permits observation of the switching process with good spatial resolution over the complete crystal and shows a better time resolution.

In SBN crystals, a 90°-scattering of a laser beam propagating normally to the polar axis was formerly reported [8, 9]. The scattering intensity drastically

decreased in poled (single-domain) crystals or at temperatures above the phase transition to the paraelectric phase [9] and could be modulated by applying a low-frequency sinusoidal field [8], so it was undoubtedly attributed to domain evolutions. This type of scattering is due to the domain walls, which are the regions of an inhomogeneity in the dielectric permittivity ϵ and can be treated, for example, as sandwichlike optical local inhomogeneities in the refractive index n_i [10]. Following this assumption, an incident plane wave characterized by a momentum vector k_i is partially reflected by a domain wall into the direction $k_r = k_i + 2(k_iq_m)q_m$, where q_m is the normal unit vector describing the wall geometry. The reflected amplitude due to a differential inhomogeneity δn and wall area dA can be approximated as

$$dE_r = E_i|k_i|H\frac{\delta n}{2n}dA, \qquad (1)$$

where H is the thickness of the wall corresponding to δn (approximation valid for $|k_i|H \ll 1$). The total scattered intensity is obtained by integrating dE_r for a typical coherence volume and then incoherently, by integrating over the illuminated volume. Following Eq. (1), the complete intensity of the 90° light scattering is proportional to three parameters: (1) the average domain wall thickness, (2) the typical magnitude of the inhomogeneity in n in the vicinity of the wall, and (3) the total wall area (i.e., number of domain walls within the illuminated volume). In turn, δn depends on the applied field E via the linear electrooptic effect.

[¶] This article was submitted by the authors in English.

The crystals under study were SBN-0.75 and SBN-0.61, for which we recently published the measurement of switching currents under pulsed fields [6, 7]. The samples were optically polished cubes $5 \times 5 \times 5$ mm in size. A focused beam from a He–Ne-laser propagated normally to the polar z axis along the x direction, and 90° scattered radiation was registered in the mutually orthogonal direction y. Both the incident laser beam and scattered light were polarized parallel to the z axis (extraordinary polarization). We measured the scattering only within a small part of the illuminated area limited by a small diaphragm placed directly in front of the crystal. Electric field pulses with a rise time of less than 1 μs were applied in the z direction. Due to the low intensity (0.05 W/cm^2) of the propagating laser beam, any photorefractive effects under applying fields were avoided and a uniform voltage distribution within the crystal bulk could be assured.

Figure 1 shows a typical scattering response (lower curve) upon an electric-field pulse (upper curve) in a polydomain SBN-0.75 sample. At $E = 0$, both in polydomain and poled SBN crystals, a nonzero scattered intensity I_b exists that may be related to a variety of reasons, in addition to a contribution from the domains. Below, in terms of domain evolutions, we discuss a change of the scattered intensity $\Delta I = I_s - I_b$ (a "flash") under an applied field pulse. According to [9], we can assume that, in the first approximation, a variation in the scattered intensity under applied fields may be attributed to variations in the domain wall density. Field-induced changes in H (see Eq. (1)) should only contribute as a second-order effect. Field-induced changes of the refractive indices are to be neglected, as they should follow the field immediately and not in a retarded way as we find it in the $\Delta I(t)$ response (Fig. 1). Therefore, the temporal characteristics of $\Delta I(t)$ depend on domain evolutions under a field pulse.

The kinetics of pulsed switching in ferroelectrics is characterized by switching times τ_s and velocities $v_s \propto \tau_s^{-1}$ depending on the field amplitude (e.g., [11]). Using our technique, we deduce τ_s directly from the kinetics of $\Delta I(t)$ (Fig. 1), which may be fitted by an exponential function $\Delta I = \Delta I_{sat}[1 - \exp(-t/\tau_s)]$ (the dashed lower curve in Fig. 1). From a set of $\Delta I(t)$ curves obtained under a pulse train (presented in the inset in Fig. 1), we can derive the dependences $\tau_s(E)$ and $\tau_s^{-1}(E)$. Figure 2 presents the plot $\tau_s(E)$ in an initially polydomain sample SBN-0.75. The values of τ_s range over tens of microseconds and are in good agreement with switching times obtained under pulse fields in the same crystal by the switching current method [6, 7]. The field dependence of the switching velocity $\tau_s^{-1}(E)$ in ferroelectrics at moderate fields often obeys the exponential law $\tau_s^{-1} = A\exp(-E_a/E)$ [11]. A fit to the measured values of τ_s^{-1}, shown as a dashed line in the inset in Fig. 2, yields
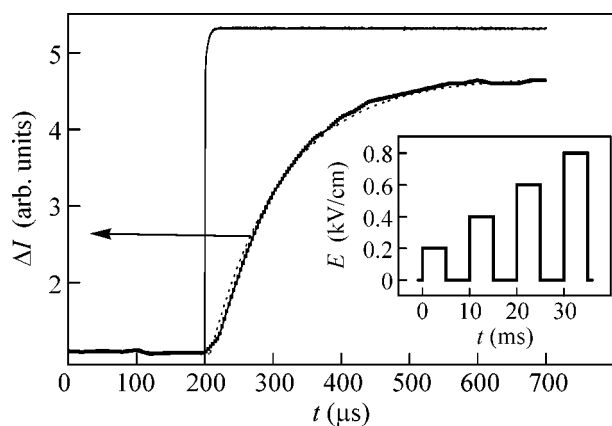

Fig. 1. Example of the scattering kinetics (the lower curve) for applying a rectangular field pulse (the upper curve). The dashed curve in the lower represents a fit of experimental data to the exponential function. The inset shows the field pulse trains.
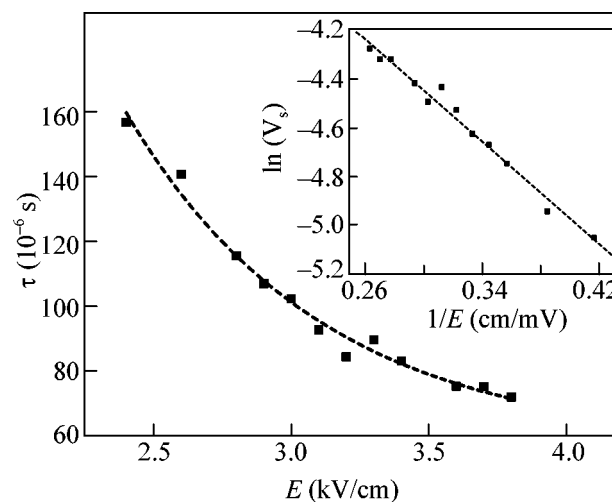
Fig. 2. Switching times as a function of the field amplitude in a polydomain SBN-0.75. The inset shows the switching velocity τ_s^{-1}, the dashed curve represents its fit by the exponential function (see text).

$A = 5.42 \times 10^4$ s^{-1} and $E_a = 5.1$ kV/cm. The latter amount, characterizing an "activation field" of the switching, is reasonable and close to the values of E_a found in other ferroelectrics, such as BaTiO$_3$ and TGS [11].

We continue with a discussion of the field dependence of the scattering intensity, i.e., of the domain density. Figure 3 presents the plots $\Delta I(E)$ for initially polydomain SBN-0.61 and SBN-0.75 crystals. The right and left branches of the curves correspond to "+" and "–" field signs, respectively, that are uniquely settled with respect to the crystal geometry. Every time before

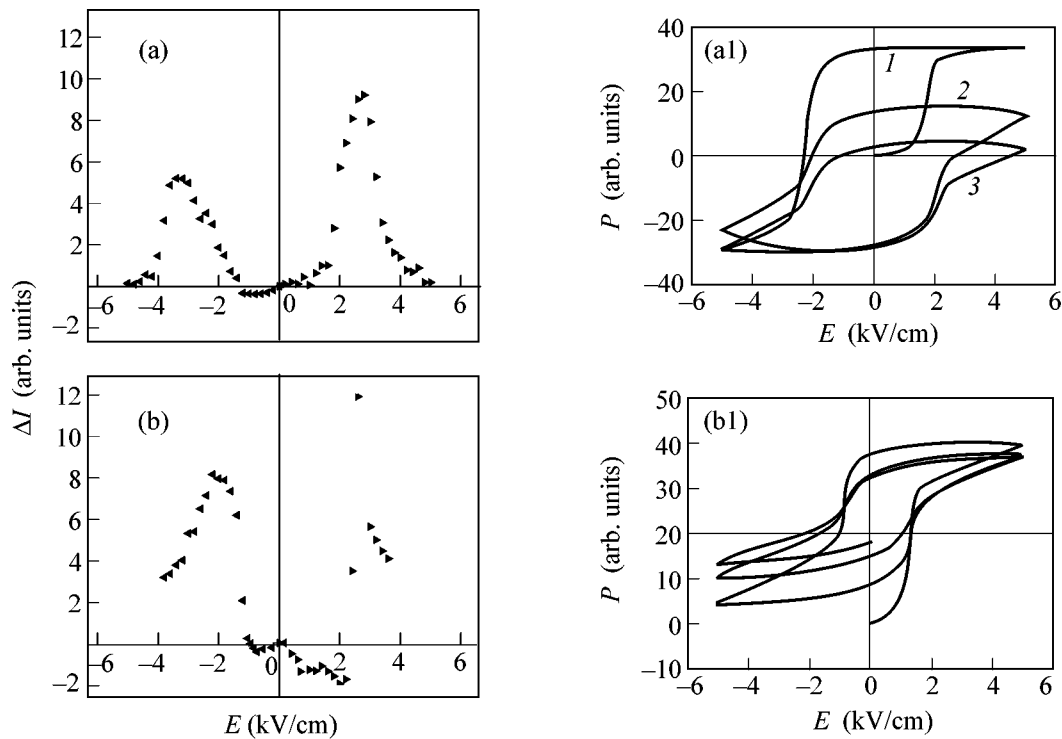**Fig. 3.** Light scattering intensities as a function of the field amplitude in polydomain crystals SBN-0.61 (a, a1) and SBN-0.75 (b, b1). Panels (a1) and (b1) show P–E loops obtained under quasistatic fields in the same crystals; labels *1, 2, 3* denote successive field cycling.

applying a pulse train of a given polarity, the crystal was brought into polydomain equilibrium by annealing it in the paraelectric phase. This means that $+E$ and $-E$ branches of $\Delta I(E)$ were measured under identical conditions. The following common features may be recognized in the $\Delta I(E)$ curves for the two crystals under study. In the range of relatively low fields of both the signs, ΔI only very slightly varies with E; at a certain E_{max}, depending on the composition, ΔI passes a maximum; and the curves are asymmetrical—namely, in a given crystal, the values of the E_{max} and peaks ΔI are different for two field polarities. To discuss these curves using the language of ferroelectricity, recall that, according to the classical model [11], the polarization (or switching) process proceeds only very slightly under low external fields and is strongly enhanced when approaching the coercive field E_c. At E close to E_c, the domain structure is reconstructed, namely, new domains are being nucleated and growing through the crystal bulk either frontally or by means of side domain-wall movement [11]; the domain density drastically increases when approaching E_c. Provided that the pulse duration exceeds the switching time, the crystal is totally polarized (or repolarized) during a single pulse $E \propto E_c$, and so on, further enhancing the field amplitude, the domain density tends to zero. Therefore, the dependence of the domain density on the pulse train amplitudes would schematically be $D \neq 0$ for $E < E_c$, D

$= D_{max}$ for $E = E_c$, and $D = 0$ for $E > E_c$. In the light of this simplified presentation, the values of E_{max} in the curves of Fig. 3 should correlate with the coercive field E_c. Different absolute values of E_{max}^+ and E_{max}^- and different peak intensities for $+E$ and $-E$ branches in a given crystal should characterize the so-called unipolarity, i.e., a preferable direction of P_s or, which is the same thing, an initial nonequality of the domain densities of "+" and "–" domains, in a crystal as a whole or at a given crystal position.

To justify this interpretation, in the insets in Fig. 3 we show dielectric hysteresis loops obtained in the same samples in a quasistatic regime with a cycling loop of about 2 h. The observed specific of P–E hysteresis, namely, "open-shaped" loops and a noncoincidence of their trajectories on several first cyclings, is characteristic for all SBN crystals [4, 5] and is accounted for by the relaxor origin of this material [12]. The averaged values of E_c estimated from several first P–E cycles for SBN-0.75 and SBN-0.61 are 1.5 and 2.5 kV/cm, respectively, which is in good agreement with the average values of E_{max} for the same crystals (2 and 3 kV/cm). The P–E loops are unipolar, that is, shifted along the E axis. The unipolarity is usually characterized by a bias field $E_b = (|E_1 - E_2|)/2$, where E_1 and E_2 are coercive fields corresponding to the left and right halves of a P–E loop [11]. Averaged values of E_b esti-

mated from first P–E cycles are 0.15 and 0.3 kV/cm in SBN-0.75 and SBN-0.61, respectively. For the optical curves $\Delta I(E)$, we define a bias field in a similar manner $E_b = (|E_{max}^+ - E_{max}^-|)/2$, yielding $E_b = 0.3$ and 0.4 kV/cm for SBN-0.75 and SBN-0.61, respectively. These amounts are in reasonable agreement with the dielectric results. The values of E_b in P–E loops slightly differ from those obtained from $\Delta I(E)$ curves because of different measurement conditions and rather conventional estimates of $E_{1,2}$ from "open-shaped" P–E loops.

The results presented in Figs. 1–3 demonstrated the validity of the optical method for ferroelectric switching studies, because all parameters deduced from the optical measurements (coercive and bias fields, unipolarity, switching times, and velocities) agree with those obtained by traditional electrical methods.

We now emphasize a fundamental divergence of the switching process in SBN as reported in [4–7] from the usual model scenario [11]. In SBN crystals, unlike in ideal ferroelectrics, no uniquely determined coercive field exists and a switched charge Q_s is controlled not only by field amplitudes but the pulse duration as well. The total polarization (or polarization reversal) requires applying fields over tens of seconds [6, 7], so, under short pulses, $Q_s \ll P_s$ even at $E \gg E_c$. Under our experimental conditions, we deal with a partial switching. For this reason, the background intensity I_b in a polydomain crystal is practically unchanged after applying a pulse train, and the peak ΔI_{max} is smeared over a rather wide field range. The times shown in Fig. 2 describe the switching of a small part of the crystal volume. Note again that, despite the fact that the crystals were preliminarily annealed in the paraelectric phase to bring them to a polydomain state, they retain unipolarity. This is why the initial domain density after annealing $D_0 < D_{max}$ (the initial light scattering $I_0 < I_{max}$). This unipolarity in an annealed crystal seems to be a specific of a relaxor ferroelectric.

Now, we show an example of a local specialty of ferroelectric switching in SBN, which was observed by scanning the bulk and, hence, not found by integrating electrical methods. The field dependences $\Delta I(E)$ presented in Fig. 3 with a small scatter in the values of $E_{max}^\pm$ are qualitatively similar in any region of a given crystal apart from the electrodes. However, when approaching them, these dependences become qualitatively different. Figure 4 presents curves $\Delta I(E)$ obtained in SBN-0.75 (the same as in Fig. 3b) in spots adjacent to the electrodes—approximately 0.1 mm apart from the upper and lower ones, respectively (the inset in Fig. 4). Both branches of these curves were obtained in the polydomain state, again after preliminary annealing in the paraelectric phase. These edge-related dependences of $\Delta I(\pm E)$ show a pronounced asymmetry. When a positive potential is applied to an electrode, the dependence $\Delta I(+E)$ is similar to $\Delta I(\pm E)$, apart from the
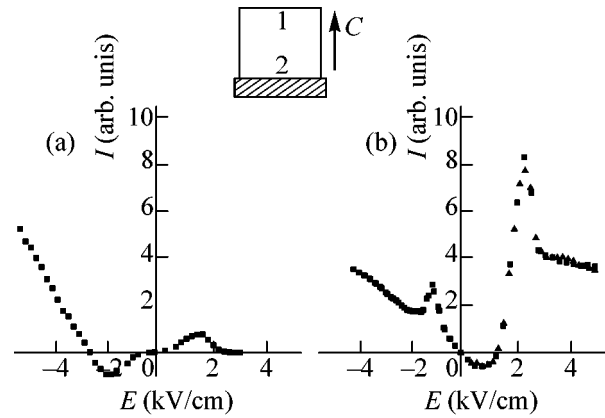

Fig. 4. Light scattering intensities as a function of the field amplitude in the vicinity of the upper (1) and lower (2) electrode in a polydomain SBN-0.75 crystal. The inset represents the layout of the sample schematically.

electrodes, shows a maximum at E_{max}^+ coinciding with the average E_{max} in the bulk, and comes to a low saturation level at $E > E_{max}^+$. In contrast, if a negative potential is applied to the same electrode (left branches of the curves in Figs. 4a and 4b), then ΔI, after passing over a slight maximum, gradually increases with E without tending to saturate. It should be emphasized that these dependences unambiguously correlate with the polarity of the electrode: a gradual increase of $\Delta I(E)$ is always observed close to the negative one. This means that, with increasing field amplitude, the domain density grows at the negative electrode only and becomes nonuniformly distributed along the polar axis. The only explanation of this asymmetry in the domain density is a preferable domain nucleation at the negative electrode and subsequent evolution in the region adjacent to it, whereas the positive electrode is "silent." This asymmetry in the domain density under short field pulses corroborates the fact that a total polarization (or polarization reversal) in SBN requires applied fields for tens of seconds [6, 7] so that domains nucleated at the negative electrode cannot germinate through the crystal bulk during application of short pulses even at $E \gg E_c$. Such a nonequiprobability of the domain nucleation is not unique; for example, a preferable domain nucleation at the negative electrode was observed in $LiNbO_3$ as well [13] by means of a successive etching of the crystal in the course of a long-term field application. An *in situ* observation of a nonuniformity of the domain density distribution in SBN crystals presented here would be useful for elaborating techniques for creation of RDS.

The domain-wall induced light scattering is obviously common for a wide group of ferroelectric crystals. For example, it was also observed in Gd_2MoO_4 [14] and $Sn_2P_2S_6$ [15]. In SBN crystals, this effect is very pronounced, perhaps because of a relatively large

thickness of a domain wall or, to be more precise, of a perturbed layer adjacent to it. A possible reason may be either an elastic strain or a space-charge field in the vicinity of the domain wall, which would lead to a large inhomogeneity in the refractive indices via the elasto- or electrooptic effects, respectively. A large elastic strain at a moving domain wall may be specific for ferroelectric crystals with a large piezoelectric effect. A space-charge field arises if the domain walls are inclined with regard to P_s, which is actually realized in SBN, e.g., in [16].

In summary, we were able to demonstrate that 90° light scattering is an excellent tool for investigating ferroelectric switching. The scattered light intensity is due to contributions from domain walls. The results can complement and extend those obtained by conventional electrical measurements. In addition to its good time resolution, the method facilitates spatially resolved measurements of switching processes. For example, we detected a preferred polarity of the electrode for domain nucleation. The potential applications of the technique include a wide group of crystals, particularly those possessing extended domain walls.

REFERENCES

1. A. M. Prokhorov and Yu. S. Kuzminov, *Ferroelectric Crystals for Laser Radiation Control* (Adam Hilger, Bristol, 1990), XIX, p. 447.
2. Y. Y. Zhu, J. S. Fu, R. F. Xiao, *et al.*, Appl. Phys. Lett. **70**, 1793 (1997).
3. Y. Y. Zhu, R. F. Xiao, J. S. Fu, *et al.*, Opt. Lett. **22**, 1382 (1997).
4. V. V. Gladkii, V. A. Kirikov, T. R. Volk, *et al.*, Zh. Éksp. Teor. Fiz. **120**, 678 (2001) [JETP **93**, 596 (2001)].
5. T. Granzow, U. Dörfler, Th. Woike, *et al.*, Phys. Rev. B **63**, 174 101 (2001).
6. T. Volk, D. Isakov, L. Ivleva, *et al.*, Appl. Phys. Lett. **83**, 2220 (2003).
7. T. R. Volk, D. V. Isakov, and L. I. Ivleva, Fiz. Tverd. Tela (St. Petersburg) **45**, 1463 (2003) [Phys. Solid State **45**, 1537 (2003)].
8. A. I. Bezhanova, V. G. Silvestrov, G. A. Zeinalova, *et al.*, Ferroelectrics **111B**, 299 (1990).
9. J. P. Wilde and R. E. Wilde, J. Appl. Phys. **71**, 418 (1992).
10. S. Kawai, T. Ogawa, H. S. Lee, *et al.*, Appl. Phys. Lett. **73**, 768 (1998).
11. M. E. Lines and A. M. Glass, *Principles and Application of Ferroelectrics and Related Materials* (Clarendon Press, Oxford, 1977; Mir, Moscow, 1981).
12. L. E. Cross, Ferroelectrics **76**, 241 (1987).
13. N. F. Evlanova, PhD Thesis (Moscow State Univ., Moscow, 1978).
14. M. A. Osman, A. M. Mamedov, and I. M. Efendieva, J. Phys.: Condens. Matter **2**, 6227 (1990).
15. A. Grabar, J. Phys.: Condens. Matter **10**, 2339 (1998).
16. G. Fogarty, B. Steiner, M. Cronin-Golomb, *et al.*, J. Opt. Soc. Am. B **13**, 2636 (1996).

Investigation of the Field-Tuned Quantum Critical Point in CeCoIn₅[¶]

V. R. Shaginyan

St. Petersburg Institute of Nuclear Physics, Russian Academy of Sciences, Gatchina, 188300 Russia
e-mail: vrshag@thd.pnpi.spb.ru
Received July 8, 2004

The main properties and the type of the field-tuned quantum critical point in the heavy-fermion metal CeCoIn₅ that arise upon application of magnetic fields B are considered within a scenario based on fermion condensation quantum phase transition. We analyze the behavior of the effective mass, resistivity, specific heat, charge, and heat transport as functions of applied magnetic fields B and show that, in the Landau Fermi liquid regime, these quantities demonstrate critical behavior, which is scaled by the critical behavior of the effective mass. We show that, in the high-field non-Fermi liquid regime, the effective mass exhibits very specific behavior, $M^* \sim T^{-2/3}$, and the resistivity demonstrates $T^{2/3}$ dependence. Finally, at elevated temperatures, it changes to $M^* \sim T^{-1/2}$, while the resistivity becomes linear in T. In zero magnetic field, the effective mass is controlled by temperature T and the resistivity is also linear in T. The obtained results are in good agreement with recent experimental facts. © 2004 MAIK "Nauka/Interperiodica".

PACS numbers: 71.10.Hf; 71.27.+a; 74.72.-h

Magnetic-field tuning of quantum critical points (QCPs) in heavy-fermion (HF) metals becomes a subject of intense current interest because, as it is widely accepted, an understating of quantum criticality can clear up a mystery of the fundamental physics of strongly correlated systems [1]. A fundamental question is whether the QCPs observed in HF metals are different and related to different quantum phase transition or their nature can be captured by the physics of a single quantum phase transition. To answer this question, we have at least to explore a particular quantum critical point in order to identify its nature. It can hardly be done on pure theoretical grounds since there can exist a great diversity of quantum phase transitions and corresponding QCPs in nature [2, 3]. Therefore, mutually complementary experimental facts related to the critical behavior and collected in measurements on the same HF metal are of crucial importance for understanding the physics of HF metals. Obviously, such HF metal will exhibit the critical behavior and has no additional phase transitions. For example, the HF metal CeRu₂Si₂ can be regarded as fit for such study because the measurements have shown neither evidence of the magnetic ordering, superconductivity nor conventional Landau Fermi-liquid (LFL) behavior down to ultralow temperatures [4]. Unfortunately, by now, only precise ac susceptibility and static magnetization measurements at small magnetic fields and ultralow temperatures are known [4]. While additional measurements of such properties as the heat and charge transport and the specific heat could produce valuable information about the existence of Landau quasiparticles and their degradation and clarify the role of the critical fluctuations near the corresponding QCP. Such measurements on the HF metal CeCoIn₅ were recently reported [5–8]. It was shown that the resistivity $\rho(T)$ of CeCoIn₅ as a function of temperature T is linear in T in the absence of a magnetic field [5]. Due to the existence of a magnetic field-tuned QCP with a critical field $B_{c0} \simeq 5.1$ T, the LFL behavior is restored at magnetic fields $B \geq B_{c0}$ [6–8]. At the LFL regime, the measurements of the specific heat and the coefficient A in the resistivity, $\rho(T) = \rho_0 + A(B)T^2$, describing the electron–electron scattering, have demonstrated that the Kadowaki–Woods ratio, $K = A(B)/\gamma^2(B)$ [9], is conserved [7]. Here, $\gamma(B) = C/T$ and C is the specific heat. It was also shown that the coefficient A diverges as $A(B) \propto (B - B_{c0})^{-\alpha}$, with $\alpha \simeq 4/3$ [6, 8]. Moreover, a recent study of CeCoIn₅ in magnetic fields $B > B_{c0}$ has revealed that the coefficients $A(B)$ and $C(B)$, with $C(B)$ describing a T^2 contribution to thermal resistivity κ_r, possess the same critical field dependence $A(B) \propto C(B) \propto (B - B_{c0})^{-\alpha}$, so that the ratio $A(B)/C(B) = c$ [8]. Here, c is a field-independent constant characterizing electron–electron scattering in metals and having a typical value of 0.47 (see, e.g., [10, 11]). The same study discovered that the resistivity behaves as $\rho(T) \propto T^n$ in the high-field non-Fermi liquid (NFL) regime, with $n \simeq 2/3$, while in the low-field NFL regime, at $B \sim B_{c0}$, the exponent $n \simeq 0.45$ [8]. Note that the same behavior of the resistivity was observed in the HF metals URu₂Si₂ [12] and YbAgGe [13] on the verge of the LFL regime and that the critical behavior takes

---

[¶] This article was submitted by the author in English.

place up to rather high temperatures comparable with the effective Fermi temperature T_k and up to high magnetic fields. For example, the resistivity measured on $CeCoIn_5$ shows the $T^{2/3}$ behavior over one decade in temperature from 2.3 to 20 K, and the coefficients $A(B)$ and $C(B)$ exhibit the same behavior at fields from $B = B_{c0} = 5.1$ T to at least 16 T [8].

In this letter, we present an explanation of the observed behavior of the electronic system of the heavy-fermion metal $CeCoIn_5$ that arises upon applying magnetic fields B. We analyze the behavior of the effective mass, resistivity, specific heat, charge, and heat transport as functions of applied magnetic field B and show that, in the Landau Fermi liquid regime, these quantities demonstrate the critical behavior, which is scaled by the critical behavior of the effective mass. In that case, the critical behavior is determined by the fermion condensation quantum phase transition (FCQPT), the physics of which is controlled by quasiparticles with the effective mass, which strongly depends on the applied magnetic field B and diverges at $B \longrightarrow B_{c0}$. In zero magnetic field, the effective mass is controlled by temperature T and the resistivity is linear in T. In the high-field non-Fermi liquid regime when the system comes from the LFL behavior to the NFL one, the effective mass exhibits very specific behavior, $M^* \sim T^{-2/3}$, and the resistivity demonstrates $T^{2/3}$ dependence. In the low-field NFL regime, at $B \sim B_{c0}$, this behavior becomes complicated, so that the resistivity behaves as T^n, with $n \sim 0.7$–0.8. At elevated temperatures and in zero magnetic field, the behavior changes to $M^* \sim T^{-1/2}$, while the resistivity becomes linear in T.

We start with a brief consideration of the LFL regime restored by the application of magnetic field $B > B_{c0}$. If the electronic system approaches FCQPT from the disordered side, the effective mass $M^*(B)$ of the restored LFL depends on magnetic field B as [14, 15]

$$M^*(B) \propto \frac{1}{(B - B_{c0})^{2/3}}. \tag{1}$$

Note that Eq. (1) is valid at $T \ll T^*(B)$, where the function $T^*(B) \propto (B - B_{c0})^{4/3}$ determines the line on the B–T phase diagram separating the region of the LFL behavior from the NFL behavior taking place at $T > T^*(B)$ [14]. To estimate the coefficient A, we observe that, at the highly correlated regime when $M^*/M \gg 1$, the coefficient $A \propto (M^*)^2$, here M is the bare electron mass [16]. As a result, we have

$$A^2(B) \propto \frac{1}{(B - B_{c0})^{4/3}}, \tag{2}$$

and observe that, in the LFL regime, the Kadowaki–Woods ratio, $K = A(B)/\gamma^2(B)$, is conserved because $\gamma(B) \propto M^*(B)$.

Let us now turn to consideration of the system's behavior at elevated temperatures, paying special attention to the transition region. To do this, we use the well-known Landau equation relating the quasiparticle energy $\varepsilon(\mathbf{p})$ near the Fermi surface to variations $\delta n(\mathbf{p}, T)$ of the quasiparticle distribution function $n_F(\mathbf{p}, T)$ [17, 18],

$$\varepsilon(\mathbf{p}) - \mu = \frac{p_F(p - p_F)}{M^*} + \int F(\mathbf{p}, \mathbf{p}_1)\delta n(\mathbf{p}_1, T)\frac{d\mathbf{p}_1}{(2\pi)^3}. \tag{3}$$

Here, μ is the chemical potential, p_F is the Fermi momentum, $F(\mathbf{p}, \mathbf{p}_1)$ is the Landau amplitude. For the sake of simplicity, the summation over the spin variables is omitted. In our case, the variation $\delta n(\mathbf{p}, T)$ is induced by temperature T and defined as $\delta n(\mathbf{p}, T) = n_F(\mathbf{p}, T) - n_F(\mathbf{p}, T = 0)$ with $n_F(\mathbf{p}, T)$ being given by the Fermi–Dirac function,

$$n_F(\mathbf{p}, T) = \left\{1 + \exp\left[\frac{\varepsilon(\mathbf{p}) - \mu}{T}\right]\right\}^{-1}. \tag{4}$$

Taking into account that $\varepsilon(p \simeq p_F) - \mu = p_F(p - p_F)/M^*$, one directly obtains from Eq. (4) that $n_F(\mathbf{p}, T \longrightarrow 0) \longrightarrow \theta(p_F - p)$, where $\theta(p_F - p)$ is the step function. In our case, Eq. (3) can be used to estimate the behavior of the effective mass $M^*(T)$ as a function of temperature. Actually, differentiating both parts of Eq. (3) with respect to the momentum p, we observe that the difference $p_F/M^*(T) - p_F/M^*(T = 0)$ is given by the integral. In turn, the integral I can be estimated upon using the standard procedure of calculating integral when the integrand contains the Fermi–Dirac function (see, e.g., [19]). As a result, we obtain

$$\frac{M}{M^*(T)} \simeq \frac{M}{M^*} + a_1\left(\frac{TM^*(T)}{T_k M}\right)^2 + a_2\left(\frac{TM^*(T)}{T_k M}\right)^4 + \dots. \tag{5}$$

Here, a_1 and a_2 are constants proportional to the derivatives of the Landau amplitude with respect to the momentum p. Equation (5) can be regarded as a typical equation of the LFL theory, the only exception being the effective mass M^*, which strongly depends on the magnetic field and diverges at $B \longrightarrow B_{c0}$ as it follows from Eq. (1). Nonetheless, at $T \longrightarrow 0$, the corrections to $M^*(B)$ start with T^2 terms, provided that

$$M/M^*(B) \gg a_1\left(\frac{TM^*(B)}{T_k M}\right)^2, \tag{6}$$

and the system exhibits the LFL behavior. At some temperature $T_1^*(B) \ll T_k$, the value of the sum on the right-hand side of Eq. (5) is determined by the second term. Then, Eq. (6) is not valid and, upon omitting the first and third terms, Eq. (5) can be used to determine the effective mass $M^*(T)$ in the transition region,

$$M^*(T) \propto T^{-2/3}. \tag{7}$$

We note that Eq. (7) has been derived in [15]. Upon comparing Eqs. (1) and (7) and taking into account that the effective mass $M^*(T)$ is a continuous function of T, we can conclude that $T_1^*(B) \propto (B - B_{c0})$.

A few remarks are in order here. Equation (7) is valid if the second term in Eq. (5) is much bigger than the first one; that is,

$$\frac{T}{T_k} \gg \left(\frac{M}{M^*}\right)^{3/2}, \tag{8}$$

and this term is bigger than the third one,

$$\frac{T}{T_k} \ll \frac{M}{M^*}. \tag{9}$$

Obviously, both Eqs. (8) and (9) can be simultaneously satisfied if $M/M^* \ll 1$. It is seen from Eqs. (1) and (9) that, at $B \longrightarrow B_{c0}$, the range of temperatures over which Eq. (7) is valid shrinks to zero, as well as $T_1^*(B) \longrightarrow 0$. Thus, it is possible to observe the behavior of the effective mass given by Eq. (7) in a wide range of temperatures provided that the effective mass $M^*(B)$ is diminished by the application of the high magnetic field (see Eq. (1)). At $B \longrightarrow B_{c0}$ and finite temperatures, Eq. (9) cannot be satisfied. Therefore, at elevated temperatures, the third term comes into play, complicating the function $M^*(T)$. To estimate the exponent n, we take into account only the third term in Eq. (5) and obtain $M^*(T) \propto T^{-n}$ with $n = 4/5$. As a result, at $B \longrightarrow B_{c0}$ and $T > T_1^*(B)$, we have the approximation

$$M^*(T) \propto T^{-n}, \tag{10}$$

with the exponent $n \sim 0.7$–0.8. The contribution coming from the other terms can only enlarge the exponent. On the other hand, $n < 1$ because, behind FCQPT, when the fermion condensate is formed, $M^*(T) \propto 1/T$ [20]. Detailed analysis of this item will be published elsewhere. Then, at elevated temperatures, the system comes to a different regime. Smoothing out the step function $\theta(p_F - p)$ at p_F, the temperature creates the variation $\delta n(\mathbf{p}) \sim 1$ over the narrow region $\delta p \sim M^*T/p_F$. In fact, the series on the right-hand side of Eq. (5) representing the value of the integral I in Eq. (3) is valid, provided that the interaction radius q_0 in the momentum space of the Landau amplitude F is much larger than δp, $q_0 \gg \delta p$. Otherwise, if $q_0 \sim \delta p$, the series does not represent I and Eqs. (5) and (7) are no longer valid. Such a situation takes place at rising temperatures because the product M^*T grows as $q_0 \sim \delta p \sim M^*T/p_F \propto T^{1/3}$, as follows from Eq. (7). As a result, the integral runs over the region q_0 and becomes proportional to M^*T/p_F. Upon omitting the first term on the right-hand side of Eq. (3) and substituting the integral by this esti-

mation, we obtain the equation that determines the behavior of the effective mass at $T > T^*(B)$ [14, 21],

$$M^*(T) \propto T^{-1/2}. \tag{11}$$

To capture and summarize the salient features of the LFL behavior observed recently in $CeCoIn_5$ [7, 8], we apply the above consideration based on FCQPT. The study of $CeCoIn_5$ in the LFL regime has shown that the coefficients $A(B)$ and $C(B)$, determining the T^2 contributions to the resistivity ρ and thermal resistivity κ_r, respectively, possess the same critical field dependence [8],

$$A(B) \propto C(B) \propto \frac{1}{(B - B_{c0})^{4/3}}. \tag{12}$$

The observed critical exponent 4/3 is in excellent agreement with that given by Eq. (2). Such a parallel behavior of charge and heat transport with the scattering rate growing as T^2 shows that the delocalized fermionic excitations are the Landau quasiparticles carrying charge e. We note that these should be destroyed in the case of conventional quantum phase transitions [2, 3]. Nonetheless, let us assume for a moment that these survive. Since the heat and charge transport tend to strongly differ in the presence of critical fluctuations of superconducting nature, the constancy of the ratio rules out critical fluctuations [8]. Therefore, we are led to the conclusion that the observed value of the critical magnetic field $B_{c0} = 5.1$ T that coincides approximately with $H_{c2} = 5$ T, the critical field at which the superconductivity vanishes, cannot be considered as giving grounds for the existence of quantum critical behavior of a new type. Then, one could expect that some kind of critical fluctuations might cause the observed parallel behavior of charge and heat transport. For example, this is impossible in the case of ferromagnetic fluctuations with a wavevector $q \simeq 0$, but large-q scattering from antiferromagnetic fluctuations of finite momenta could degrade the heat and charge transport in a similar way [11]. In this case, in order to preserve the Kadowaki–Woods ratio, these fluctuations are to properly influence the specific heat, which characterizes the thermodynamic properties of the system and is not directly related to the transport one. On the other hand, there are no theoretical grounds for the conservation of the Kadowaki–Woods ratio within the frameworks of conventional quantum phase transitions [22]. Therefore, the conservation of the Kadowaki–Woods ratio observed in recent measurements of $CeCoIn_5$ [7] definitely seems to rule out these fluctuations. However, both the constancy of the Kadowaki–Woods ratio [7] and the constancy of the $A(B)/C(B)$ ratio [8] give strong evidence in favor of the quasiparticle picture.

Now, we turn to consideration of the resistivity $\rho(T)$. As we will see below, striking recent measurements of the resistivity [8, 12, 13] furnish new evidence in favor

of the quasiparticle picture and the existence of FCQPT.

As follows from Eq. (11) and the above-mentioned relation $A \propto (M^*)^2$, the term $AT^2 \propto M^*T^2$ turns out to be $\propto T$ [14]. As a result, in zero magnetic field and relatively high temperatures $T > T_c$, the resistivity of CeCoIn$_5$ is linear in T. Here, T_c is the critical temperature at which the superconductivity vanishes. This observation is in good agreement with the experimental facts [5].

At temperatures $T < T_1^*(B)$ and magnetic field $B > B_{c0}$, the system exhibits LFL behavior with T^2 dependence of the resistivity $\rho(T)$. Such a behavior is in agreement with the experimental facts [6–8].

At a high applied magnetic field and finite temperatures $T > T_1^*(B)$ when the system comes into the NFL regime, the effective mass M^* is determined by Eq. (7). In this case, the range of temperatures over which Eq. (7) is held becomes rather wide and the system demonstrates an anomalous $T^{2/3}$. Actually, upon using the same arguments, we obtain that $AT^2 \propto (M^*)^2 T^2 \propto T^{2/3}$ and conclude that the resistivity $\rho(T) \propto T^{2/3}$. Again, this result is in excellent agreement with the reported observations [8, 12, 13].

If the magnetic field $B \longrightarrow B_{c0}$ and the temperature is relatively high, $T > T_1^*(B)$, so that the system enters the NFL regime, the effective mass is given by Eq. (10). In this case, the resistivity $\rho(T) \propto (M^*)^2 T^2 \propto T^k$, with $k = 2 - 2n = 0.6$–0.4. This result is in reasonable agreement with the reported observation of anomalous $T^{0.45}$ dependence of the resistivity in a small region near the critical field $B_{c0} = 5.1$ T [8].

In conclusion, we have shown that the experimentally observed behavior of the electronic system of the heavy-fermion metal CeCoIn$_5$ arising upon applying magnetic fields can be understood within the framework of the FCQPT scenario. We have shown that, in the LFL regime, the resistivity, specific heat, charge, and heat transport, as functions of applied magnetic field B, demonstrate critical behavior, which is scaled by the critical behavior of the effective mass. We have observed that this critical behavior is determined by FCQPT, the physics of which is controlled by quasiparticles with the effective mass, which in the LFL regime

strongly depends on the applied magnetic field and diverges at $B \longrightarrow B_{c0}$. In zero magnetic field, the effective mass is controlled by temperature T and the resistivity is linear in T. In a high-field NFL regime, the effective mass exhibits very specific behavior, $M^* \sim T^{-2/3}$, while the resistivity demonstrates $T^{2/3}$ dependence. At elevated temperatures, the behavior changes to $M^* \sim T^{-1/2}$, while the resistivity becomes linear in T.

REFERENCES

1. G. R. Stewart, Rev. Mod. Phys. **73**, 797 (2001).
2. S. Sachdev, *Quantum Phase Transitions* (Cambridge Univ. Press, Cambridge, 1999).
3. M. Vojta, Rep. Prog. Phys. **66**, 2069 (2003).
4. D. Takahashi *et al.*, Phys. Rev. B **67**, 180407 (2003).
5. C. Petrovic *et al.*, J. Phys.: Condens. Matter **13**, L337 (2001).
6. J. Paglione, M. A. Tanatar, D. G. Hawthorn, *et al.*, Phys. Rev. Lett. **91**, 246405 (2003).
7. A. Bianchi, R. Movshovich, I. Vekhter, *et al.*, Phys. Rev. Lett. **91**, 257001 (2003).
8. J. Paglione *et al.*, cond-mat/0405157.
9. K. Kadowaki and S. B. Woods, Solid State Commun. **58**, 507 (1986).
10. A. J. Bennet and M. J. Rice, Phys. Rev. **185**, 968 (1969).
11. J. Paglione, cond-mat/0404269.
12. K. H. Kim, N. Harrison, M. Jaime, *et al.*, Phys. Rev. Lett. **91**, 256401 (2003).
13. S. L. Bud'ko, E. Morosan, and P. C. Canfield, Phys. Rev. B **69**, 014415 (2004).
14. V. R. Shaginyan, JETP Lett. **77**, 99 (2003); JETP Lett. **77**, 178 (2003).
15. M. V. Zverev and V. A. Khodel, JETP Lett. **79**, 632 (2004).
16. V. A. Khodel and P. Schuck, Z. Phys. B **104**, 505 (1997).
17. L. D. Landau, Sov. Phys. JETP **3**, 920 (1956).
18. E. M. Lifshitz and L. P. Pitaevskiǐ, *Course of Theoretical Physics*, Vol. 5: *Statistical Physics* (Nauka, Moscow, 1978; Butterworth, London, 1999), Part 2.
19. E. M. Lifshitz and L. P. Pitaevskiǐ, *Course of Theoretical Physics*, Vol. 5: *Statistical Physics* (Nauka, Moscow, 1978; Butterworth, London, 1999), Part 1, p. 168.
20. J. Duckelsky *et al.*, Z. Phys. B **102**, 245 (1997).
21. V. R. Shaginyan, JETP Lett. **79**, 286 (2004).
22. V. R. Shaginyan, J. G. Han, and J. Lee, Phys. Lett. A (in press); cond-mat/0405025.

Observation of Stimulated Raman Scattering in CVD-Diamond¶

A. A. Kaminskii[1], V. G. Ralchenko[2], and V. I. Konov[2]

[1] Institute of Crystallography, Russian Academy of Sciences, Moscow, 119333 Russia
[2] Natural Sciences Center, Institute of General Physics, Russian Academy of Sciences, Moscow, 119991 Russia
e-mail: kaminalex@mail.ru; ralchenko@nsc.gpi.ru
Received July 1, 2004

We report the first experimental observation of a nonlinear laser effect, stimulated Raman scattering (SRS), in manmade diamond grown from the gaseous phase by the chemical vapor deposition (CVD) technique. Multiple Stokes and anti-Stokes generation in the visible and near-IR ranges was excited under nanosecond and picosecond pumping in a 350-μ-thick plate. All the registered Raman-induced lasing wavelengths were identified. We classify the CVD-diamond as a promising $\chi^{(3)}$-active material for Raman laser converters in a record wide spectral range. © 2004 MAIK "Nauka/Interperiodica".

PACS numbers: 42.65.Dr; 42.70.-a; 81.05.Uw

1. In the last decade, the use of the stimulated Raman scattering (SRS) phenomenon in crystalline materials to shift the wavelengths of laser emission has become more widespread in solid-state laser physics (see, e.g., [1–4]). The SRS process allows to compress laser pulses. It can also improve the spatial quality of laser beams, etc. Modern laser applications require crystals providing large Raman frequency shifts of considerably more than 1000 cm^{-1}. (For the list of these SRS-active materials, see Table 1. Natural diamonds are also included in the list.) Recently, great progress has been achieved in synthesis of large-area diamonds at low pressure using a chemical vapor deposition (CVD) technique [5]. The material is essentially polycrystalline with arbitrary oriented grains. In many respects, the quality of CVD diamonds approaches that of the purest natural diamonds. In contrast to natural stones, the impurity and defect contents in CVD diamond are quite reproducible and of low level.

This work is devoted to reporting on the results of the first experimental observation of $\chi^{(3)}$-nonlinear laser effect, namely, the high-order Stokes and anti-Stokes generation in CVD diamond thin plates under nano- and picosecond excitation in the visible and near-IR ranges.

2. Diamond belongs to the O_h^7 cubic space group with eight atoms per unit cell (two per primitive cell) giving to six phonon branches in the dispersion relation. At the center of the Brillouin zone ($\mathbf{k} = 0$), the three optical branches are triply degenerate and the corresponding phonons belong to the F_{2g} irreducible representation. The first-order Raman spectrum contains one peak corresponding to the excitation of these optical phonons. Diamond consists of the light mass of the C-atoms held together by strong covalent bonding, and this combination produces many remarkable properties for laser physics—e.g., high thermal conductivity and a relatively large energy of Raman-active mode ≈1332.5 cm^{-1}—that promote SRS lasing. Some physical properties of natural and manmade diamonds that are known by us are listed in Table 2.

3. In the present work, a transparent diamond film of ≈450 μ thickness was grown on a Si substrate in a microwave-plasma-assisted CVD reactor using CH$_4$/H$_2$ mixture as a source gas [6]. After the substrate was etched off in acid, the film was laser-cut to 6 × 8 mm^2 samples and mechanically polished to get plane-parallel plates of 350 μ thickness. The major impurities were 75 ppm hydrogen and 1 ppm nitrogen (1 ppm = 1.76 × 10^{17} cm^{-3}) as determined from IR and UV absorption spectra, respectively [7]. Upon growth, the grains, being chaotically oriented in the film plane, form columns with their axes directed perpendicular to surface. Columns with a lateral size of about 40–100 μ are predominantly ⟨110⟩-oriented.

4. The SRS experiments with CVD diamond plate were performed at 300 K using a cavity-free single-pass excitation scheme and nano- and picosecond Nd^{3+}:Y$_3$Al$_5$O$_{12}$ lasers with a ≈30% efficient external frequency doublers as pumping sources (see, e.g., [17, 18]). Their generation with a Gaussian beam profile at fundamental $\lambda_{f1} = 1.06415$ μ (pump pulse duration $\tau_{p1} \approx 15$ ns and ≈110 ps, respectively) or SHG at $\lambda_{f2} = 0.53207$ μ ($\tau_{p1} \approx 15$ ns and ≈80 ps, respectively) wavelength was focused onto the diamond plate by a lens with focal distance adjusted, so that the SRS-lasing was

---

¶ This article was submitted by the authors in English.

Table 1

Crystal*	Space group	Nonlinearity (class)	ω_{SRS}, cm^{-1}**	References
Inorganic crystals				
LiHCOO · H$_2$O	C_{2v}^9	$\chi^{(2)} + \chi^{(3)}$ (polar)	≈ 1372	[8]
Natural diamond***	O_h^7	$\chi^{(3)}$	≈ 1332	[9, 10]
CVD-diamond****	O_h^7	$\chi^{(3)}$	1332.5 ± 0.8	This work
CaCO$_3$ (calcite)	D_{3d}^6	$\chi^{(3)}$	≈ 1086	[9, 11, 2]
Sr(NO$_3$)$_2$	T_h^6	$\chi^{(3)}$	≈ 1057	[13]
Y(HCOO)$_3$ · 2H$_2$O	D_2^4	$\chi^{(2)} + \chi^{(3)}$	$\approx 1395, \approx 1377, \approx 2895$	[14]
Ba(NO$_3$)$_2$	T_h^6	$\chi^{(3)}$	≈ 1049	[15, 16]
Organic crystals				
C$_{12}$H$_{22}$O$_{11}$ (sugar, sucrose)	C_2^2	$\chi^{(2)} + \chi^{(3)}$ (polar)	≈ 2960	[17]
C$_{15}$H$_{19}$N$_3$O$_2$ (AANP)	C_{2v}^9	$\chi^{(2)} + \chi^{(3)}$ (polar)	≈ 1280	[18]
C$_{16}$H$_{15}$N$_3$O$_4$ (MNBA)	C_s^4	$\chi^{(2)} + \chi^{(3)}$ (polar)	≈ 1587	[19]
Metal–organic crystal				
C$_{14}$H$_{26}$N$_8$O$_{13}$Zr (CuZn-III)	D_2^5	$\chi^{(2)} + \chi^{(3)}$	$\approx 1008, \approx 2940$	[20]

 * Some of these crystals are already commercial materials.
 ** Room-temperature data.
 *** Natural diamond crystals of type IIA with a thickness of about 2 mm.
**** Manmade polycrystalline diamond.

maximum while avoiding surface and volume optical damaging of the sample. This was achieved when the waist beam diameter into diamond plate was 100–160 μ. These excitation conditions provided a steady-state $\chi^{(3)}$-generation regime effectively, because, for the studied CVD diamond, $\tau_p \gg T_2 = 1/\pi\Delta\nu_R \approx 4.2$ ps (here, T_2 and $\Delta\nu_R$ are the phonon relaxation time and the linewidth of the corresponding peak in the spontaneous Raman scattering spectrum, respectively). The spectral composition of Stokes and anti-Stokes lasing in the visible and near-IR under maximum possible pump density power was measured with grating monochromators equipped with appropriate detectors (Si-CCD, InSb-diode, etc.). The generated SRS wavelengths observed are summarized in Table 3, which contains room-temperature Stokes and anti-Stokes generation wavelengths in CVD diamond (350-μ-thick plate) with natural abundance of isotopic (carbon) composition connected with its SRS-active vibration mode $\omega_{SRS} = 1332.5$ cm^{-1} under nano- and picosecond Nd^{3+}:Y$_3$Al$_5$O$_{12}$-laser excitation at $\lambda_{f1} = 1.06415$ μ and $\lambda_{f2} = 0.53207$ μ (SHG) fundamental wavelengths.

5. For rough estimation of the steady-state Raman gain coefficient $g_{ssR}^{St_1}$ in the near-IR, we applied a simple comparative method using the well-known relation

(see, e.g., [23]) $g_{ssR}^{St_1} I_{thr} l_{SRS} = 25$–$30$ (where I_{thr} is the threshold pump intensity and l_{SRS} is the SRS-active length of the sample) and based on a measurement of the pumping threshold for the first Stokes generation component in our ≈ 350 μ CVD diamond ($\lambda_{St1} = 1.2400$ μ; see Table 3) and in a reference ≈ 500 μ C$_{15}$H$_{19}$N$_3$O$_2$ (AANP) crystal ($\lambda_{St1} = 1.2320$ μm [18]) under the same excitation conditions. We observed that the threshold for the first Stokes nanosecond lasing of the diamond threshold was about 40% less than for the AANP plate. This means that the coefficient $g_{ssR}^{St_1}$ is no less than 8 cm/GW. The SRS conversion efficiency into all Stokes and anti-Stokes components in the examined diamond sample, even when grown in not optimized conditions, reached a value of about 30% at pump power density of approximately 2.5 GW/cm^2 under picosecond excitation at $\lambda_{f2} = 0.53207$ μm wavelength.

6. In conclusion, we have discovered a $\chi^{(3)}$-nonlinear laser potential for CVD diamonds. Due to continuous progress in CVD diamond technology, large-size (diameter >100 mm, thickness >2 mm) and even ultra-pure CVD diamond single crystals [24] have become available. From these considerations, we believe that new generation of CVD diamonds in near future can

Table 2

Space group	$O_h^7 - Fm\bar{3}d$ (No. 227)
Unit-cell parameter, Å	$a_0 = 3.56676$
Site symmetry of atoms	C_1
Formula units per cell	$Z = 8*$
Density, g/cm^{-3}	$d \approx 3.51$
Melting point, °C	>3400
Debye temperature, K	≈ 1860
Band gap, eV	≈ 5.4
Optical transparency range, μ	≈ 0.225–3.8; 5.5–∞ (till radio frequencies)
Dielectric constant	$\varepsilon \approx 5.7$ (for f = up to 10^{11} Hz)
Refractive index (Sellmeier equation) (λ in μ)	$n^2 = 1 + \dfrac{4.3356\lambda^2}{\lambda^2 - 0.0256} + \dfrac{0.3306\lambda^2}{\lambda^2 - 0.030625}$
$dn/dT \times 10^6$, K^{-1}	≈ 10 (for $\lambda = 0.587$ μ)
Nonlinear refractive index, 10^{-13} cm^3 erg (at $\lambda = 0.545$ μ and laser pulse duration $\tau_p = 4$ ns)	$n_2 \approx 7.2$
Thermal conductivity, W/(cm K) (for our polycrystalline CVD-diamond)	≈ 18
Thermal expansion coefficient, 10^{-6} K^{-1}	≈ 1
Elastic constants, 10^{11} N m^2	$C_{11} = 10.40$; $C_{12} = 1.70$; $C_{44} = 5.50$
Elastooptic coefficients (at $\lambda = 0.540$–0.589 μ)	$p_{11} = -0.278$; $p_{12} = 0.123$; $p_{44} = -0.161$; $p_{11} - p_{12} = -0.385$
Energy of SRS-active vibration mode, cm^{-1}	$\omega_{SRS} = 1332.5 \pm 0.8$
Linewidth (FWHM) of the Raman-shifted line in first-order spontaneous Raman scattering spectra, cm^{-1}	$\Delta\nu_R \approx 2.5$ (for our polycrystalline CVD-diamond) $\Delta\nu_R$ for natural diamonds ranges from 1.65 to 2.7 (see, e.g., [21, 22])
Phonon spectrum extension, cm^{-1}**	≈ 1333

  * Primitive (Bravais) cell contains two formula units $N^{Br} = 2$.
** From first-order spontaneous Raman scattering spectra.

Table 3

Nanosecond pumping		Picosecond pumping		Line attribution
Wavelength, μ	Line	Wavelength, μ	Line	
Pumping at $\lambda_{f1} = 1.06415$ μ				
		0.7466	ASt$_3$	$\omega_{f1} + 3\omega_{SRS}$
		0.8290	ASt$_2$	$\omega_{f1} + 2\omega_{SRS}$
0.9320	ASt$_1$	0.9320	ASt$_1$	$\omega_{f1} + \omega_{SRS}$
1.06415 ($\approx$1.3)*	λ_{f1}	1.06415 ($\approx$2.5)*	λ_{f1}	ω_{f1}
1.2400	St$_1$	1.2400	St$_1$	$\omega_{f1} - \omega_{SRS}$
1.4854	St$_2$			$\omega_{f1} - 2\omega_{SRS}$
Pumping at $\lambda_{f2} = 0.53207$ μ				
		0.4660	ASt$_2$	$\omega_{f2} + 2\omega_{SRS}$
0.4968	ASt$_1$	0.4968	ASt$_1$	$\omega_{f2} + \omega_{SRS}$
0.53207 ($\approx$0.3)*	λ_{f2}	0.53207 ($\approx$0.7)*	λ_{f2}	ω_{f2}
0.5727	St$_1$	0.5727	St$_1$	$\omega_{f2} - \omega_{SRS}$
		0.6200	St$_2$	$\omega_{f2} - 2\omega_{SRS}$

* Pump power density (in parentheses) given in GW/cm^2.

hold a leading position among all known $\chi^{(3)}$-active crystalline materials for Raman laser converters.

ACKNOWLEDGMENTS

REFERENCES

1. M. J. Weber, *Handbook of Lasers* (CRC Press, Boca Raton, 2001).

2. A. A. Kaminskii, *Crystalline Lasers: Physical Processes and Operating Schemes* (CRC Press, Boca Raton, 1996).

3. Special issue of Opt. Mater. **11** (March) (1999), Ed. by T. T. Basiev and R. C. Powell.

4. G. A. Pasmanik, Laser Focus World **35**, 137 (1999).

5. *Handbook of Industrial Diamonds and Diamonds Films*, Ed. by M. Prelas *et al.* (Marcel Dekker, New York, 1997).

6. V. G. Ralchenko, A. A. Smolin, V. I. Konov, *et al.*, Diamond Relat. Mater. **6**, 417 (1997).

7. S. V. Nistor, M. Stefan, V. Ralchenko, *et al.*, J. Appl. Phys. **87**, 8741 (2000).

8. K. K. Lai, W. Schusslbauer, H. Silberbauer, *et al.*, Phys. Rev. B **42**, 5834 (1990).

9. G. Eckhard, D. P. Bortfeld, and M. Geller, Appl. Phys. Lett. **3**, 137 (1963).

10. A. K. McQuillan, W. R. L. Clements, and B. P. Stoicheff, Phys. Rev. A **1**, 628 (1970).

11. R. Chiao and B. P. Stoicheff, Phys. Rev. Lett. **12**, 290 (1964).

12. V. A. Chirkov, V. S. Gorelik, G. V. Peregudov, and M. M. Sushinskii, JETP Lett. **10**, 416 (1969).

13. A. A. Kaminskii, J. Hulliger, H. Eichler, *et al.*, Dokl. Phys. **44**, 69 (1999).

14. A. A. Kaminskii, L. Bohaty, P. Becker, *et al.*, Phys. Status Solidi A **202** (1) (2004).

15. A. S. Eremenko, S. N. Karpukhin, and A. I. Stepanov, Sov. J. Quantum Electron. **10**, 113 (1986).

16. P. G. Zverev, J. T. Murreay, R. C. Powell, *et al.*, Opt. Commun. **97**, 59 (1993).

17. A. A. Kaminskii, Crystallogr. Rep. **48**, 295 (2003).

18. A. A. Kaminskii, T. Kaino, T. Taima, *et al.*, Jpn. J. Appl. Phys. **41**, L603 (2002).

19. A. A. Kaminskii, J. Hulliger, and H. J. Eichler, Phys. Status Solidi A **186**, R19 (2001).

20. A. A. Kaminskii, E. Haussuhl, J. Hulliger, *et al.*, Phys. Status Solidi A **193**, 167 (2002).

21. S. A. Solin and A. K. Ramdas, Phys. Rev. B **1**, 1687 (1970).

22. T. T. Basiev, A. A. Sobol, P. G. Zverev, *et al.*, Appl. Opt. **38**, 594 (1999).

23. W. Kaiser and M. Maier, in *Laser Handbook*, Ed. by F. T. Arecchi and E. O. Schulz-Dubois (North-Holland, Amsterdam, 1972), p. 1077; Y. R. Shen, *The Principles of Nonlinear Optics* (Wiley, New York, 1984; Nauka, Moscow, 1989).

24. J. Isberg, J. Hammersberg, E. Johansson, *et al.*, Science **297**, 1670 (2002).

Influence of Retardation Effects
on a 2D Magnetoplasmon Spectrum[¶]

M. V. Cheremisin

Ioffe Physicotechnical Institute, Russian Academy of Sciences, St. Petersburg, 194021 Russia
e-mail: maksim.vip1@pop.ioffe.rssi.ru
Received May 27, 2004; in final form, July 12, 2004

Within a dissipationless limit, the magnetic field dependence of the magnetoplasmon spectrum for an unbounded two-dimensional electron gas (2DEG) system was found to intersect the cyclotron resonance line and, then, approach the frequency given by light dispersion relation. Recent experiments done for macroscopic disc-shaped 2DEG systems confirm theoretical expectations. © *2004 MAIK "Nauka/Interperiodica".*

PACS numbers: 73.20.Mf; 71.36.+c

Plasma oscillations in two-dimensional electron gas (2DEG) were first predicted in the mid-1960s [1] and then observed experimentally in a liquid helium system [2] and silicon inversion layers [3, 4]. The recent observation [5] of a magnetoplasmon (MP) spectrum reported to be affected by retardation effects, which was discussed more than three decades ago, is sparking new interest in the above problem. Taking into account the retardation effects, we analyze 2D MP spectrum first derived in [6]. It will be argued that, in large-mesa two-dimensional (2D) systems [5], the role of edges becomes less significant; therefore, the observed MP features can be accounted for within conventional MP theory [6] for an unbounded 2D system.

Let us assume an unbounded 2D electron gas imbedded in dielectric in the presence of a perpendicular magnetic field. Following [7], the Maxwell equations for in-plane components of the electrodynamic potentials A, ϕ yield

$$\Box^{\phi} = 4\pi\rho, \quad \Box^{\mathbf{A}} = \frac{4\pi\mathbf{j}}{c},$$

$$\text{div}\mathbf{A} + \frac{\epsilon}{c}\frac{\partial\phi}{\partial t} = 0, \tag{1}$$

$$\mathbf{j} = -\sigma^*\left(\nabla\phi + \frac{1}{c}\frac{\partial\mathbf{A}}{\partial t}\right),$$

where $\Box = (\epsilon/c^2)(\partial^2/\partial t^2) - \Delta$ is the d'Lambert operator and σ^* is the conductivity tensor. Assuming the magnetoplasmon $e^{(i\mathbf{q}\mathbf{r} - i\omega t)}$ propagated in 2DEG and then separating longitudinal and transverse in-plane compo-

---

[¶] This article was submitted by the author in English.

nents of the vector potential [7], the 2D magnetoplasmon dispersion relation yields

$$\left(\frac{\epsilon}{2\pi} + \frac{i\sigma_{xx}\kappa}{\omega}\right)\left(\frac{1}{2\pi} - \frac{i\omega\sigma_{xx}}{c^2\kappa}\right) + \frac{\sigma_{yx}^2}{c^2} = 0, \tag{2}$$

where $\kappa = \sqrt{q^2 - \epsilon\omega^2/c^2}$. This result is exactly that obtained by Chiu [6]. Within a dissipationless limit, the components of the conductivity tensor,

$$\sigma_{xx} = \sigma_{yy} = \frac{i\omega ne^2}{m(\omega^2 - \omega_c^2)}, \quad \sigma_{yx} = -\sigma_{xy} = \frac{i\omega_c}{\omega}\sigma_{xx}$$

allow us to simplify Eq. (2) as follows:

$$(Q^2 - \Omega^2)^{\frac{1}{2}} = \sqrt{\frac{(1 + \Omega_c^2 - \Omega^2)^2}{4} + \Omega^2} - \frac{1 + \Omega_c^2 - \Omega^2}{2}, \tag{3}$$

where we introduce the dimensionless wave vector $Q = qc/\omega_p\sqrt{\epsilon}$, frequency $\Omega = \omega/\omega_p$, and cyclotron frequency $\Omega_c = \omega_c/\omega_p$, which are all expressed in a certain frequency unit $\omega_p = 2\pi ne^2/mc\sqrt{\epsilon}$. We further clarify the physical sense of ω_p.

In absence of the magnetic field, Eq. (3) reproduces the conventional [1, 7] zero-field longitudinal plasmon dispersion relation $\epsilon = 2\pi i\sigma_{xx}\kappa/\omega$ as follows:

$$Q^2 = \Omega_0^2 + \Omega_0^4. \tag{4}$$

In the short-wavelength limit $Q \gg 1$, one obtains the well-known square-root plasmon dispersion as $\omega_0 = \sqrt{(2\pi ne^2/m\epsilon)q}$. The opposite long-wavelength limit case $Q \ll 1$ corresponds to the light dispersion relation $\omega_l = cq/\sqrt{\epsilon}$ shown in Fig. 1 by the dotted line. In actual fact, ω_p denotes the frequency when the zero-field plas-
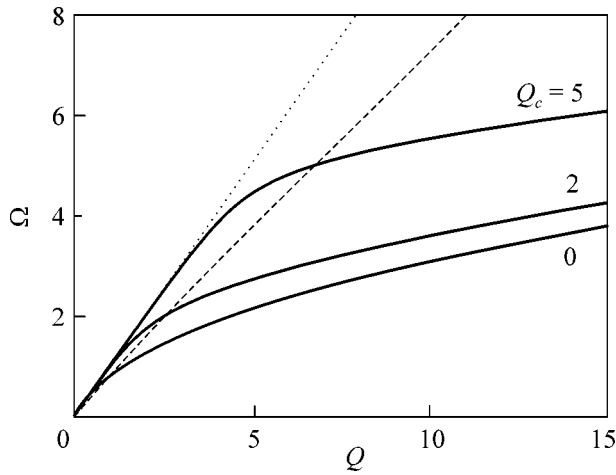
Fig. 1. Magnetoplasmon dispersion at $\Omega_c = 0$ (zero-field plasmon), 2, and 5. Asymptote: light dispersion (dotted line). Dashed line represents the dependence $\Omega_{cr}(Q)$ when the condition $\omega = \omega_c$ is satisfied.
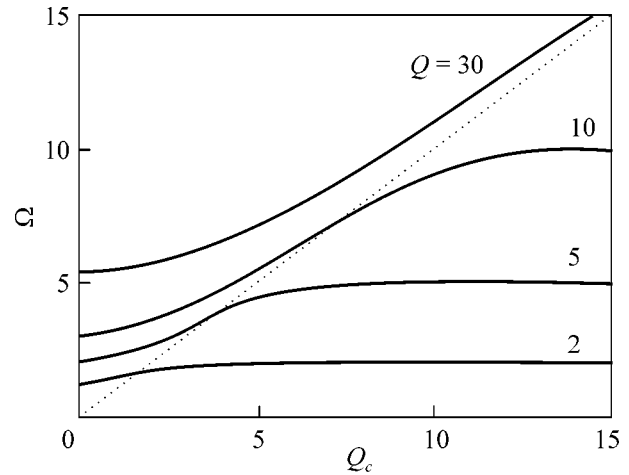

Fig. 2. 2D magnetoplasmon spectra vs. dimensionless cyclotron frequency Ω_c for different MP wave vector $Q = 2$, 5, 10, and 30. Arrows represent the light frequency. Cyclotron resonance is represented by dotted line.

mon phase velocity deduced from the square-root dispersion law approaches the speed of light. Note that the authors of [5] demonstrate an excellent agreement between the zero-field 2D plasmon theory [1, 8] and the experimental results. For different disc-geometry quantum well samples, the wave vector reported to relate to 2DEG disc diameter via $q = \alpha/d$, $\alpha = 2.4$ is consistent with theory, $\alpha = 3\pi/4$ [9].

The question we are attempting to answer is whether retardation effects should modify the 2D magnetoplasmon spectrum. In actual fact, Eq. (3) demonstrates that, at fixed Q, the plasma frequency grows with the magnetic field and then intersects the CR line (see Figs. 1, 2). This behavior is, however, unexpected within edge magnetoplasmon formalism [10, 11]. Substituting $\Omega = \Omega_c$ into Eq. (3), we derive the dependence (Fig. 1, dashed line) of the MP-CR intersection frequency vs. wave vector $\Omega_{cr}(Q)$. It is to be noted that low-field magnetoplasmon remains longitudinal at $\omega_c < \omega$ and then becomes transverse when $\omega_c > \omega$.

Further increase of the magnetic field results in saturation of the magnetoplasmon spectrum (Fig. 2) at a certain frequency given by the light dispersion relation. Experimentally, irrespective of 2DEG density, the mac-

roscopic ($d = 1$ mm) disc-mesa samples demonstrate [5] MP spectra (with the lowest radial and angular momenta numbers) cutoff at a frequency of 50 GHz. The latter is larger than that deduced from the light dispersion relation $\omega_l/2\pi = 32$ GHz, where we use the GaAs dielectric constant $\epsilon = 12.8$. However, for an actual (GaAs + free space) system, the average dielectric constant [9], i.e., $\epsilon^* = (1 + \epsilon)/2$, provides much better agreement (see table), namely, that $f_l = (1/2\pi)(qc/\sqrt{\epsilon^*}) = 44$ GHz. Note that, in contrast to the predicted MP spectrum saturation in strong fields, the experiments in [5] demonstrate an intriguing zigzag behavior that remains unexplained in our formalism.

It is instructive to compare the lowest angular momentum MP spectrum reported in [5] with that provided by the present theory. For example, for GaAs/AlGaAs heterostructure ($n = 2.54 \times 10^{11}$ cm^{-2}, $m = 0.067m_0$, $d = 1$ mm, $\epsilon = 12.8$), one obtains $\omega_p = 5.6 \times 10^{10}$ s^{-1} and $Q = 3.6$. With the help of Eqs. (4) and (3), the zero-field plasmon frequencies $f_0 = \omega_0/2\pi = 16$ GHz and $f_{cr} = \omega_{cr}/2\pi = 25$ GHz are found to be comparable with the experimental values 20 and 32 GHz, respectively. An excellent agreement ($f_0 = 21$ GHz and $f_{cr} = 34$ GHz, respectively) with experiment is provided using the average dielectric constant, ϵ^*. The table represents the comparison between the present theory and available experimental data. Note that, in [5], the experimental range of frequencies <60 GHz is less than that expected to include MP-CR intersection and subsequent spectra saturation in a low density, small disc-mesa 2DEG case.

In conclusion, we demonstrate the strong influence of retardation effects on the magnetoplasmon spectrum in an unbounded 2DEG system. The magnetic field dependence of an MP spectrum is found to intersect the

Theory vs. experiment [5]

d, mm	$n \times 10^{10}$ cm^{-2}	Q	f_0^*, GHz	f_{cr}, GHz	f_l, GHz
1.0	66.0	1.4	**31**/27	**36**/37	**44**/50
1.0	25.4	3.6	**21**/20	**34**/32	**44**/50
0.2	4.2	108	**21**/20	**155**/–	**218**/–
0.1	4.2	359	**23**/29	**308**/–	**435**/–

* f values are given as theory/experiment.

cyclotron resonance line and then approach the frequency given by the light dispersion relation. Recent MP experiments in large disc-shape 2DEG systems confirm the theoretical predictions.

ACKNOWLEDGMENTS

REFERENCES

1. F. Stern, Phys. Rev. Lett. **18**, 546 (1967).

2. C. C. Grimes and G. Adams, Phys. Rev. Lett. **36**, 145 (1976).

3. S. J. Allen, D. C. Tsui, and R. A. Logan, Phys. Rev. Lett. **38**, 980 (1977).

4. T. N. Theis, J. P. Kotthaus, and P. J. Stiles, Solid State Commun. **26**, 603 (1978).

5. I. V. Kukushkin, J. H. Smet, S. A. Mikhailov, *et al.*, Phys. Rev. Lett. **90**, 156801 (2003).

6. K. W. Chiu and J. J. Quinn, Phys. Rev. B **9**, 4724 (1974).

7. V. I. Falko and D. E. Khmel'nitskii, Sov. Phys. JETP **68**, 1150 (1989).

8. In both 3D and 2D cases, the edge plasmon frequency is known to differ with respect to the bulk case (see K. W. Chiu and J. J. Quinn, Phys. Rev. B **5**, 4707 (1972) and [10, 11]).

9. R. P. Leavitt and J. W. Little, Phys. Rev. B **34**, 2450 (1986).

10. A. L. Fetter, Phys. Rev. B **32**, 7676 (1985).

11. V. A. Volkov and S. A. Mikhailov, Sov. Phys. JETP **67**, 1639 (1988).

Stability of the Bose System in Bose–Fermi Mixture with Attraction between Bosons and Fermions[¶]

S. T. Chui[1], V. N. Ryzhov[2, *], and E. E. Tareyeva[2]

[1] *Bartol Research Institute, University of Delaware, DE 19716 Newark, USA*
[2] *Institute for High Pressure Physics, Russian Academy of Sciences, Troitsk, Moscow region, 142190 Russia*
**e-mail: ryzhov@hppi.troitsk.ru*
Received June 24, 2004; in final form, July 12, 2004

An effective Hamiltonian for the Bose system in the mixture of ultracold atomic clouds of bosons and fermions is obtained by integrating out the Fermi degrees of freedom. An instability of the Bose system is found in the case of attractive interaction between components that is in good agreement with an experiment on the bosonic ^{87}Rb and fermionic ^{40}K mixture. © *2004 MAIK "Nauka/Interperiodica".*

PACS numbers: 03.75.Hh; 03.75.Mn; 67.57.Fg; 67.90.+z

Since the first realization of Bose–Einstein condensation in ultracold atomic gas clouds [1–3], studies in this area have yielded unprecedented insight into the quantum statistical properties of matter. Besides studies using bosonic atoms, growing interest has been focused on the cooling of fermionic atoms to a temperature regime where quantum effects dominate the properties of the gas [4–6]. This interest is mainly motivated by the quest for the Bardeen–Cooper–Schrieffer (BCS) transition in ultracold atomic Fermi gases [7–9].

Strong *s*-wave interactions that facilitate evaporative cooling of bosons are absent among spin-polarized fermions due to the exclusion Pauli principle. So, the fermions are cooled to degeneracy through the mediation of fermions in another spin state [4, 6–9] or via a buffer gas of bosons [5, 10, 11] (sympathetic cooling). Bose gas, which can be cooled evaporatively, is used as a coolant, the fermionic system being in thermal equilibrium with the cold Bose gas through boson–fermion interaction in the region of overlapping of the systems.

However, the physical properties of Bose–Fermi mixtures are interesting in their own right and are the subject of intensive investigations, including analysis of ground-state properties, stability, effective Fermi–Fermi interaction mediated by the bosons, and new quantum phases in optical lattices [12–16]. Several successful attempts to trap and cool mixtures of bosons and fermions have been reported. Quantum degeneracy was first reached with mixtures of bosonic ^{7}Li and fermionic ^{6}Li atoms [5, 10]. Later, experiments to cool mixtures of ^{23}Na and ^{6}Li [17], as well as ^{87}Rb and ^{40}K [11, 18], to ultralow temperatures succeeded.

In this article, we study the instability and collapses of the trapped boson–fermion mixture due to boson–fermion attractive interaction, using the effective

Hamiltonian for the Bose system [14]. We analyze quantitatively properties of the ^{87}Rb and ^{40}K mixture with an attractive interaction between bosons and fermions recently studied by Modugno and coworkers [11]. They found that, as the number of bosons is increased, there is an instability value N_{Bc} at which a discontinues leakage of the bosons and fermions occurs and collapse of boson and fermion clouds is observed. Using experimental parameters, we estimated the instability boson number N_{Bc} for the collapse transition as a function of the fermion number and temperature and found a good agreement with the experimental results.

First of all, we briefly discuss the effective boson Hamiltonian [14]. Our starting point is the functional–integral representation of the grand-canonical partition function of the Bose–Fermi mixture. It has the form [15, 19, 20]

$$Z = \int D[\phi^*]D[\phi]D[\psi^*]D[\psi]$$

$$\times \exp\left\{-\frac{1}{\hbar}(S_B(\phi^*, \phi) + S_F(\psi^*, \psi) + S_{int}(\phi^*, \phi, \psi^*, \psi))\right\} \quad (1)$$

and consists of an integration over a complex field $\phi(\tau, \mathbf{r})$, which is periodic on the imaginary-time interval $[0, \hbar\beta]$, and over the Grassmann field $\psi(\tau, \mathbf{r})$, which is antiperiodic on this interval. Therefore, $\phi(\tau, \mathbf{r})$ describes the Bose component of the mixture, whereas $\psi(\tau, \mathbf{r})$ corresponds to the Fermi component. The term describing the Bose gas has the form

$$S_B(\phi^*, \phi) = \int_0^{\hbar\beta} d\tau \int d\mathbf{r} \left\{\phi^*(\tau, \mathbf{r})\left(\hbar\frac{\partial}{\partial\tau} - \frac{\hbar^2\nabla^2}{2m_B}\right.\right.$$

$$\left.\left. + V_B(\mathbf{r}) - \mu_B\right)\phi(\tau, \mathbf{r}) + \frac{g_B}{2}|\phi(\tau, \mathbf{r})|^4\right\}. \quad (2)$$

[¶] This article was submitted by the authors in English.

Because the Pauli principle forbids s-wave scattering between fermionic atoms in the same hyperfine state, the Fermi-gas term can be written in the form

$$S_F(\psi^*, \psi) = \int_0^{\hbar\beta} d\tau \int d\mathbf{r} \left\{ \psi^*(\tau, \mathbf{r}) \left(\hbar \frac{\partial}{\partial \tau} - \frac{\hbar^2 \nabla^2}{2m_F} \right. \right.$$
$$\left. \left. + V_B(\mathbf{r}) - \mu_F \right) \psi(\tau, \mathbf{r}) \right\}. \tag{3}$$

The term describing the interaction between the two components of the Fermi–Bose mixture is

$$S_{\text{int}}(\phi^*, \phi, \psi^*, \psi) = g_{BF} \int_0^{\hbar\beta} d\tau \int d\mathbf{r} |\psi(\tau, \mathbf{r})|^2 |\phi(\tau, \mathbf{r})|^2, \tag{4}$$

where $g_B = 4\pi\hbar^2 a_B/m_B$, $g_{BF} = 2\pi\hbar^2 a_{BF}/m_I$, $m_I = m_B m_F/(m_B + m_F)$; m_B and m_F are the masses of bosonic and fermionic atoms, respectively; and a_B and a_{BF} are the s-wave scattering lengths of boson–boson and boson–fermion interactions.

The integral over the Fermi fields is Gaussian; we can calculate this integral and obtain the partition function of the Fermi system as a functional of the Bose field $\phi(\tau, \mathbf{r})$. Let us rewrite the integral over $\psi(\tau, \mathbf{r})$ in the form

$$Z_F = \int D[\psi^*] D[\psi] \exp\left(-\frac{1}{\hbar} (S_F(\psi^*, \psi) \right.$$
$$\left. + S_{\text{int}}(\phi^*, \phi, \psi^*, \psi)) \right)$$
$$= \int D[\psi^*] D[\psi] \exp\left\{ \int_0^{\hbar\beta} d\tau \int d\mathbf{r} \int_0^{\hbar\beta} d\tau' \int d\mathbf{r}' \right. \tag{5}$$
$$\left. \times \psi^*(\tau, \mathbf{r}) \mathbf{G}^{-1}(\tau, \mathbf{r}, \tau', \mathbf{r}') \psi(\tau', \mathbf{r}') \right\},$$

where

$$\mathbf{G}^{-1} = \mathbf{G}_0^{-1} - \mathbf{\Sigma} \tag{6}$$

is the Dyson equation and $\Sigma(\tau, \mathbf{r}, \tau', \mathbf{r}')$ is a self-energy,

$$\mathbf{G}_0^{-1}(\tau, \mathbf{r}, \tau', \mathbf{r}') = -\frac{1}{\hbar} \left(\hbar \frac{\partial}{\partial \tau} - \frac{\hbar^2 \nabla^2}{2m_F} \right.$$
$$\left. + V_F(\mathbf{r}) - \mu_F \right) \delta(\mathbf{r} - \mathbf{r}') \delta(\tau - \tau'); \tag{7}$$

$$\mathbf{\Sigma}(\tau, \mathbf{r}, \tau', \mathbf{r}') = \frac{g_{BF}}{\hbar} |\phi(\tau, \mathbf{r})|^2 \delta(\mathbf{r} - \mathbf{r}') \delta(\tau - \tau'). \tag{8}$$

Using the formula for the Gaussian integral over the Grassmann variables [19, 20],

$$\int \prod_n d\psi_n^* d\psi_n \exp\left\{ -\sum_{n, n'} \psi_n^* A_{n, n'} \psi_{n'} \right\} = e^{\text{Sp}[\ln A]} \tag{9}$$

one has

$$Z_F = \exp(\text{Sp}\ln(-\mathbf{G}^{-1})) = \exp\left(-\frac{1}{\hbar} S_{\text{eff}} \right). \tag{10}$$

S_{eff} can be expanded in powers of $|\phi(\tau, \mathbf{r})|^2$ by using the series

$$\mathbf{G}^{-1} = \mathbf{G}_0^{-1} - \mathbf{\Sigma} = \mathbf{G}_0^{-1}(\mathbf{I} - \mathbf{G}_0 \Sigma),$$
$$\text{Sp}(\ln(-\mathbf{G}^{-1})) = \text{Sp}(\ln(-\mathbf{G}_0^{-1})) - \sum_{n=1}^{\infty} \frac{1}{n} \text{Sp}[(\mathbf{G}_0 \Sigma)^n]. \tag{11}$$

To proceed, let us rewrite $\mathbf{G}_0$ in the form

$$\mathbf{G}_0(\tau, \mathbf{r}, \tau', \mathbf{r}') = \sum_{\omega, n} \frac{-\hbar}{-i\hbar\omega + \epsilon_n - \mu_F}$$
$$\times \xi_n(\mathbf{r}) \xi_n^*(\mathbf{r}') \frac{e^{-i\omega(\tau - \tau')}}{\hbar\beta}, \tag{12}$$

where $\omega = \pi(2s + 1)/\hbar\beta$, $s = 0, \pm 1, \ldots,$ and

$$\left(-\frac{\hbar^2 \nabla^2}{2m_F} + V_F(\mathbf{r}) \right) \xi_n(\mathbf{r}) = \epsilon_n \xi_n(\mathbf{r}).$$

Because of the large number of fermionic atoms in the system, one can use the semiclassical Thomas–Fermi approximation [21],

$$\sum_n \xi_n(\mathbf{r}) \xi_n^*(\mathbf{r}) F(\epsilon_n) = \frac{1}{(2\pi\hbar)^3} \int d\mathbf{p} F(H_0(\mathbf{p}, \mathbf{r})), \tag{13}$$

where $H_0(\mathbf{p}, \mathbf{r}) = p^2/2m_F + V_F(\mathbf{r})$ and $F(x)$ is an arbitrary function.

We suppose that all $|\phi(\tau_i, \mathbf{r}_i)|^2$ have one and the same argument $(\tau_1, \mathbf{r}_1)$ (see, for example, [19]). Using Eq. (13), S_{eff} may be written in the form

$$S_{\text{eff}} = \int_0^{\hbar\beta} d\tau d\mathbf{r} f_{\text{eff}}(|\phi(\tau, \mathbf{r})|), \tag{14}$$

$$f_{\text{eff}} = -\frac{3}{2} \kappa \beta^{-1} \int_0^{\infty} \sqrt{\epsilon} d\epsilon \ln(1 + e^{\beta(\tilde{\mu} - \epsilon)})$$
$$= -\kappa \int_0^{\infty} \frac{\epsilon^{3/2} d\epsilon}{1 + e^{\beta(\epsilon - \tilde{\mu})}}, \tag{15}$$

where $\epsilon = p^2/2m_F$, $\tilde{\mu} = \mu_F - V_F(\mathbf{r}) - g_{BF}|\phi(\tau, \mathbf{r})|^2$ and $\kappa = 2^{1/2} m_F^{3/2}/3\pi^2\hbar^3$.

Thus, we can write the effective bosonic Hamiltonian in the form

$$H_{\text{eff}} = \int d\mathbf{r} \left\{ \frac{\hbar^2}{2m_B} |\nabla\phi|^2 + (V_B(\mathbf{r}) - \mu_B)|\phi|^2 \right. \tag{16}$$

$$\left. + \frac{g_B}{2}|\phi|^4 + f_{\text{eff}}(|\phi|) \right\}.$$

The first three terms in (16) have the conventional Gross–Pitaevskii [22] form and the last term is a result of boson–fermion interaction. In the low temperature limit $\tilde{\mu}/k_B T \gg 1$, one can write $f_{\text{eff}}(|\phi|)$ in the form

$$f_{\text{eff}}(|\phi|) = -\frac{2}{5}\kappa\tilde{\mu}^{5/2} - \frac{\pi^2}{4}\kappa(k_B T)^2\tilde{\mu}^{1/2}. \tag{17}$$

As usual, μ_F can be determined from the equation

$$N_F = \int d\mathbf{r}\, n_F(\mathbf{r}), \tag{18}$$

where

$$n_F(\mathbf{r}) = \frac{3}{2}\kappa \int_0^\infty \frac{\sqrt{\epsilon}\,d\epsilon}{1 + e^{\beta(\epsilon - \tilde{\mu})}}. \tag{19}$$

At low temperatures, we have

$$n_F(\mathbf{r}) = \kappa\tilde{\mu}^{3/2} + \frac{\pi^2\kappa}{8\tilde{\mu}^{1/2}}(k_B T)^2. \tag{20}$$

In the general case, the Bose and Fermi systems have different temperature scales and Eqs. (17) and (20) may be useful for studying the temperature behavior of the Bose system, including the calculation of the critical temperature. For example, the characteristic temperature for the Bose system (the transition temperature for the ideal Bose gas) is [22] $k_B T_c^0 = 0.94\hbar\omega_B(\lambda N_B)^{1/3}$. The Fermi temperature for a pure system is [21] $k_B T_F = \hbar\omega_F(6\lambda N_F)^{1/3}$. Taking into account that $\omega_F = \sqrt{m_B/m_F}\,\omega_B$, one can see that, for $m_B > m_F$ and approximately the same numbers of bosons and fermions, one can safely use Eqs. (17) and (20) to describe the behavior of the Bose system.

Let us consider now an ^{87}Rb and ^{40}K mixture with an attractive interaction between bosons and fermions [11]. The parameters of the system are the following: $a_B = 5.25$ nm, $a_{BF} = -21.7^{+4.3}_{-4.8}$ nm. K and Rb atoms were prepared in the doubly polarized states $|F = 9/2, m_F = 9/2\rangle$ and $|2, 2\rangle$, respectively. The magnetic potential had an elongated symmetry, with harmonic oscillation frequencies for Rb atoms $\omega_{B,\,r} = \omega_B = 2\pi \times 215$ Hz and $\omega_{B,\,z} = \lambda\omega_B = 2\pi \times 16.3$ Hz and $\omega_F = \sqrt{m_B/m_F}\,\omega_B \approx 1.47\omega_B$, so that $m_B\omega_B^2/2 = m_F\omega_F^2/2 = V_0$. The collapse

was found for the following critical numbers of bosons and fermions: $N_{Bc} \approx 10^5$, $N_K \approx 2 \times 10^4$.

At the zero temperature limit, expanding $f_{\text{eff}}(|\phi|)$ up to the third order in g_{BF}, we obtain the effective Hamiltonian in the form

$$H_{\text{eff}} = \int d\mathbf{r} \left\{ \frac{\hbar^2}{2m_B}|\nabla\phi|^2 + (V_{\text{eff}}(\mathbf{r}) - \mu_B)|\phi|^2 \right. \tag{21}$$

$$\left. + \frac{g_{\text{eff}}}{2}|\phi|^4 + \frac{\kappa}{8\mu_F^{1/2}}g_{BF}^3|\phi|^6 \right\},$$

where

$$V_{\text{eff}}(\mathbf{r}) = \left(1 - \frac{3}{2}\kappa\mu_F^{1/2}g_{BF}\right)\frac{1}{2}m_B\omega_B^2(\rho^2 + \lambda^2 z^2), \tag{22}$$

$$g_{\text{eff}} = g_B - \frac{3}{2}\kappa\mu_F^{1/1}g_{BF}^2, \tag{23}$$

and $\rho^2 = x^2 + y^2$.

In principle, one can study the properties of a Bose–Fermi mixture with the help of f_{eff} (17) without any expansion. However, the form of the Hamiltonian (21) gives the possibility to get a clear insight into the physics of the influence of the Fermi system on the Bose one (see discussion below). It may be easily verified that the expansion of the function $f(x) = (1 + x)^{5/2}$ (see Eq. (17)) up to the third order in x gives a reasonably good approximation for $f(x)$ even for rather large values of x, in contrast with the higher-order expansions, so one can safely use Eq. (21) as a starting point for the investigation of the properties of the Bose subsystem.

In the derivation of Eqs. (21)–(23), we also use the fact that, due to the Pauli principle (quantum pressure), the radius of the Bose condensate is much smaller than the radius of the Fermi cloud $R_F \approx \sqrt{\mu_F/V_0}$, so one can use expansions in powers of $V_F(\mathbf{r})/\mu_F$.

From Eq. (22), one can see that the interaction with Fermi gas leads to modification of the trapping potential. For attractive fermion–boson interaction, the system should behave as if it were confined in a magnetic trapping potential with larger frequencies than the actual ones, in agreement with experiment [11]. Boson–fermion interaction also induces additional attraction between Bose atoms, which does not depend on the sign of g_{BF}.

The last term in H_{eff} (21) corresponds to the three-particle *elastic* collisions induced by the boson–fermion interaction. In contrast with *inelastic* three-body collisions, which result in the recombination and removing particles from the system [23], this term for $g_{BF} < 0$ leads to increase of the gas density in the center of the trap in order to lower the total energy. The positive zero point energy and boson–boson repulsion

energy (the first two terms in Eq. (21)) stabilize the system. However, if the central density grows too much, the kinetic energy and boson–boson repulsion are no longer able to prevent collapse of the gas. Likewise, in the case of Bose condensate with attraction (see, for example, [22–24]), collapse is expected to occur when the number of particles in the condensate exceeds the critical value N_{Bc}.

The critical number N_{Bc} can be calculated using the well-known ansatz for the bosonic wave function [22]:

$$\phi(\mathbf{r}) = \left(\frac{N_B\lambda}{w^3 a^3 \pi^{3/2}}\right)^{1/2} \exp\left(-\frac{(\rho^2 + \lambda^2 z^2)}{2w^2 a^2}\right), \quad (24)$$

where w is a dimensionless variational parameter that fixes the width of the condensate and $a = \sqrt{\hbar/m_B\omega_B}$.

In this case, the variational energy E_B has the form

$$\frac{E_B}{N_B\hbar\omega_B} = \frac{2+\lambda}{4}\frac{1}{w^2} + bw^2 + \frac{c_1 N_B}{w^3} + \frac{c_2 N_B^2}{w^6},$$

$$b = \frac{3}{4}\left(1 - \frac{3}{2}\kappa\mu_F^{1/2}g_{BF}\right),$$

$$c_1 = \frac{1}{2}\left(g_B - \frac{3}{2}\kappa\mu_F^{1/2}g_{BF}^2\right)\frac{\lambda}{(2\pi)^{3/2}\hbar\omega_B a^3}, \quad (25)$$

$$c_2 = \frac{\kappa}{8\mu_F^{1/2}}g_{BF}^3\frac{\lambda^2}{3^{3/2}\pi^3\hbar\omega_B a^6}.$$

This energy is plotted in Fig. 1 as a function of w for several values of N_B. It is seen that, when $N_B < N_{Bc}$, there is a local minimum of E_B, which corresponds to a metastable state of the system. This minimum arises due the competition between the positive first three terms in Eq. (25) and negative fourth term. The local minimum disappears when the number of bosons N_B exceeds the critical value, which can be calculated by requiring that the first and second derivatives of E_B vanish at the critical point. In this case, the behavior of E_B is mainly determined by the second and fourth terms in Eq. (25). For $N_K = 2 \times 10^4$ and $a_{BF} = -19.44$ nm, we obtain $N_{Bc} \approx 9 \times 10^4$ in good agreement with the experiment [11]. It is interesting to note that the critical number of Bose atoms in the Bose–Fermi mixture is about two orders larger than the critical number for the condensate with a purely attractive interaction. For example, in the experiments with trapped ^{7}Li [3], it was found that the critical number of bosons is about 1000.

In Eq. (25), we use $\mu_F^0 = \hbar\omega_F[6\lambda N_F]^{1/3}$ as the chemical potential of the Fermi system μ_F. The corrections to μ_F due to interaction with the Bose system have the form $\mu_F = \hbar\omega_F[6N_F]^{1/3}[1 + m_1 + m_2]$,
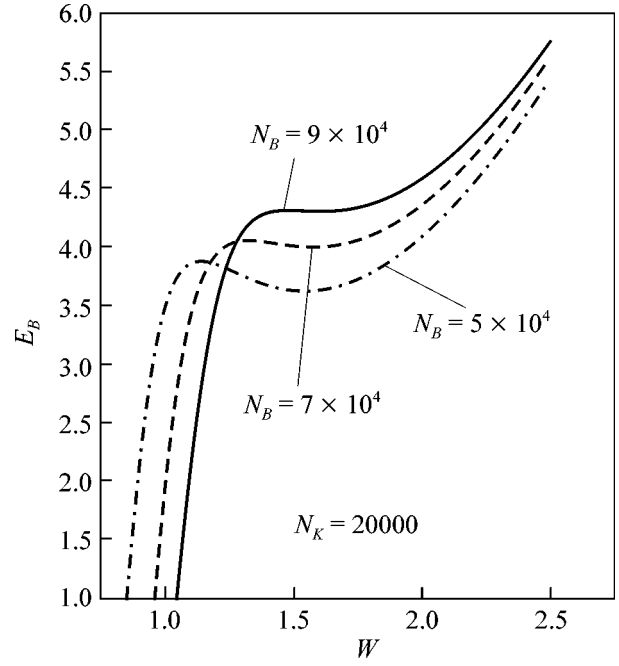

Fig. 1. Variational energy $E_B/N_B\hbar\omega_B$ as a function of w for various numbers of bosons.
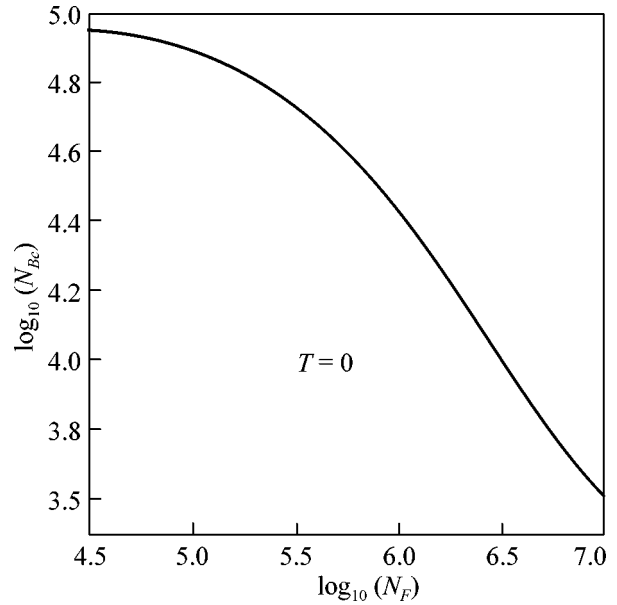

Fig. 2. Critical number of bosons N_{Bc} as a function of the number of fermions N_F at $T = 0$.

where $m_1 = \dfrac{1/2\kappa g_{BF}(\mu_F^0)^{1/2}N_B}{N_F}$ and $m_2 = -\dfrac{3/4\kappa g_{BF}(\mu_F^0)^{-1/2}m_F\omega_F^2 w^2 a^2 N_B}{N_F}$. It may be shown that $m_1 + m_2 \approx 0.09$ for the values of the parameters used in these calculations.
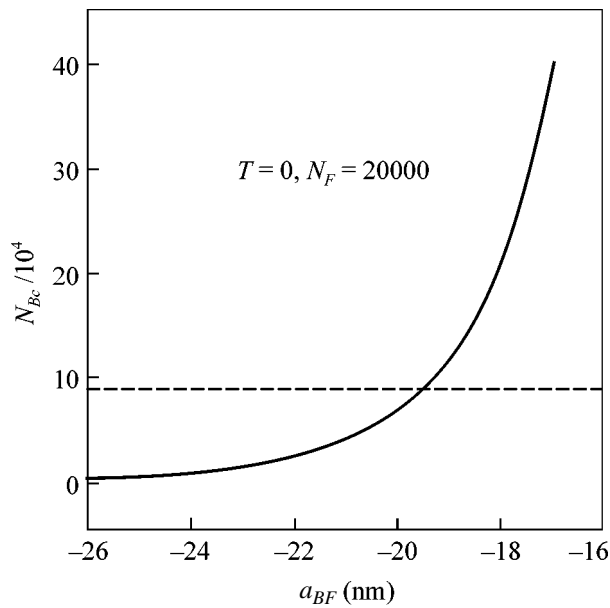
Fig. 3. Critical number of bosons N_{Bc} as a function of the boson–fermion scattering length a_{BF}.
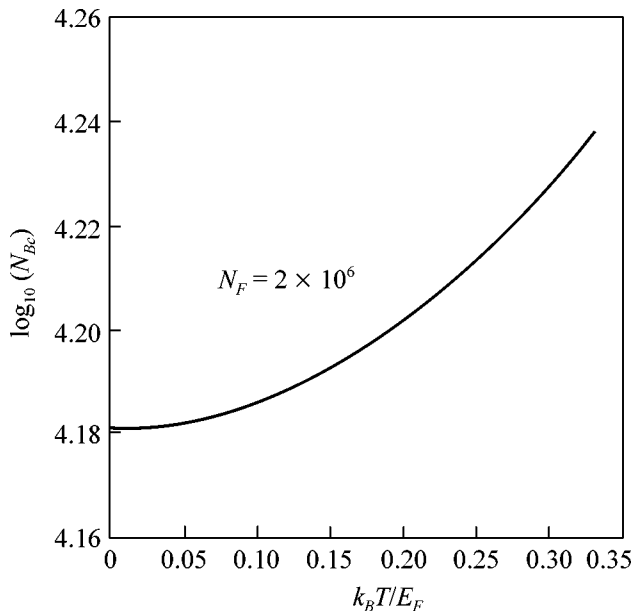

Fig. 4. Critical number of bosons N_{Bc} as a function of reduced temperature $k_B T/E_F$ for $N_F = 2 \times 10^6$.

Upon increasing the number of fermions, the repulsion between bosons decreases, leading to the collapse for the smaller numbers of the bosonic atoms. In Fig. 2, the critical number of bosons N_{Bc} is represented as a function of the number of fermions.

The critical number of bosons N_{Bc} is extremely sensitive to the precise value of the boson–fermion *s*-wave scattering length. This is illustrated in Fig. 3.

Figure 4 shows the dependence of the critical number of bosons N_{Bc} on the temperature calculated with the help of Eq. (17). This dependence has a simple explanation: an increase of the temperature results in the decrease of the local density of fermions and reduces the interaction energy between Bose and Fermi systems.

Finally, we make a short remark on the nature of the collapse transition. In this article, we found the instability point of the Bose–Fermi mixture with attractive interaction between components. A strong rise of density of bosons and fermions (see Eq. (20)) in the collapsing condensate enhances intrinsic inelastic processes, in particular, the recombination in three-body interatomic collisions, as is the case for the well-known ^{7}Li condensates [23]. However, recently, M.Yu. Kagan and coworkers suggested a new microscopic mechanism of removing atoms from the system, which is specific for Bose–Fermi mixtures with attraction between components and is based on the formation of boson–fermion bound states [25]. It seems that the description of the evolution of the collapsing condensate should include both these mechanisms.

REFERENCES

1. M. N. Anderson, J. R. Ensher, M. R. Matthews, *et al.*, Science **269**, 198 (1995).
2. K. B. Davis, M.-O. Mewes, M. R. Andrews, *et al.*, Phys. Rev. Lett. **75**, 3969 (1995).
3. C. C. Bradley, C. A. Sackett, and R. G. Hulet, Phys. Rev. Lett. **78**, 985 (1997).
4. B. DeMarco and D. S. Jin, Science **285**, 1703 (1999).
5. A. G. Truscott, K. E. Strecker, W. I. McAlexander, *et al.*, Science **291**, 2570 (2001).
6. K. M. O'Hara, S. L. Hemmer, M. E. Gehm, *et al.*, Science **298**, 2179 (2002).
7. C. A. Regal, C. Ticknor, J. L. Bohn, and D. S. Jin, Nature **424**, 47 (2003).
8. M. Greiner, C. A. Regal, and D. S. Jin, Nature **426**, 537 (2003).
9. S. Jochim, M. Bartenstein, A. Altmeyer, *et al.*, Science **302**, 210 (2003).
10. F. Schreck, L. Khaykovich, K. L. Corwin, *et al.*, Phys. Rev. Lett. **87**, 080403 (2001).
11. G. Modungo, G. Roati, F. Riboli, *et al.*, Science **297**, 2240 (2002).

12. T. Miyakawa, T. Suzuki, and H. Yabu, Phys. Rev. A **64**, 033611 (2001).

13. R. Roth, Phys. Rev. A **66**, 013614 (2002).

14. S. T. Chui and V. N. Ryzhov, Phys. Rev. A **69**, 043607 (2004).

15. M. J. Bijlsma, B. A. Heringa, and H. T. C. Stoof, Phys. Rev. A **61**, 053601 (2000).

16. M. Lewenstein, L. Santos, M. A. Baranov, and H. Fehrmann, Phys. Rev. Lett. **92**, 050401 (2004).

17. Z. Hadzibabic, C. A. Stan, K. Dieckmann, *et al.*, Phys. Rev. Lett. **88**, 160401 (2002).

18. J. Goldwin, S. B. Papp, B. DeMarco, and D. S. Jin, Phys. Rev. A **65**, 021402(R) (2002).

19. V. N. Popov, *Functional Integrals in Quantum Field Theory and Statistical Physics* (Reidel, Dordrecht, 1983).

20. H. T. C. Stoof, cond-mat/9910441.

21. D. A. Butts and D. S. Rokhsar, Phys. Rev. A **55**, 4346 (1997).

22. F. Dalfovo, S. Giorgini, L. P. Pitaevskii, and S. Stringari, Rev. Mod. Phys. **71**, 463 (1999).

23. Yu. Kagan, A. E. Muryshev, and G. V. Shlyapnikov, Phys. Rev. Lett. **81**, 933 (1998).

24. Yu. Kagan, G. V. Shlyapnikov, and J. T. W. Walraven, Phys. Rev. Lett. **76**, 2670 (1996).

25. M. Yu. Kagan, I. V. Brodsky, D. V. Efremov, and A. V. Klaptsov, cond-mat/0209481.

Anticlinic-Synclinic Transitions in Superthin Free-Standing Smectic Films[¶]

P. V. Dolganov[1],*, G. Joly[2], P. Cluzeau[3], V. K. Dolganov[1], C. Gors[2], and H. T. Nguyen[3]

[1] Institute of Solid State Physics RAS, Chernogolovka, Moscow region, 142432 Russia
* e-mail: pauldol@issp.ac.ru
[2] Laboratoire de Dynamique et Structures des Matériaux Moleculaire, Université de Lille 1, Villeneuve d'Ascq, 59655 France
[3] Centre de Recherche Paul Pascal, CNRS, Pessac, 33600 France
Received July 14, 2004

Anticlinic-synclinic transition was studied in superthin smectic films using polarized light reflected microscopy. The measurements were made in a compound exhibiting the SmC_{FI1}^* subphase in a narrow temperature interval between antiferroelectric SmC_A^* and ferroelectric SmC^* phases. In films, we observed series of transitions with numbers increasing with increasing film thickness. Surface ordering leads to increasing transition temperatures with decreasing film thickness and to change of orientation of the molecular tilt plane in layers. Succession of transitions results from competition between the surface and the bulk ordering. We found that line string defects may form in a film, their orientation and collective behavior resulting from elastic deformation of molecular ordering. © *2004 MAIK "Nauka/Interperiodica".*

PACS numbers: 61.30.-v; 64.70.Md

The unique structural quality of thin free-standing smectic films makes them ideal objects for studies of surface phenomena and phase transitions in restricted geometry [1]. Of special interest are studies of structures with a two-component order parameter, when the surface may influence both the modulus and the phase of the order parameter. Such structures are liquid crystals with polar ordering of smectic layers: fundamental ferroelectric Smectic-C^* (SmC^*) [2], the antiferroelectric Smectic-C_A^* (SmC_A^*)[3, 4] phases, and intermediate smectic subphases [3, 4]. In smectic-C (SmC) type liquid crystals, each layer may be regarded as an orientationally ordered liquid with long molecular axes tilted by an angle θ with respect to the smectic layer normal. The azimuthal orientation of molecules in layers is characterized by the order parameter phase φ. The structure of tilted smectics may also be described by a two-dimensional vector, the so-called **c** director (projection of the nematic **n** director onto the smectic layer plane) [5]. Different sequences of variation from layer to layer of phase φ and modulus θ of the order parameter lead to the formation of a variety of smectic structures. In the SmC^* structure, the order parameter phase φ in neighboring layers (i and $i + 1$) differs insufficiently $\Delta\varphi = \varphi_{i+1} - \varphi_i \approx 0$. In the Sm$C_A^*$ structure, molecules in adjacent layers are tilted in nearly opposite directions $\Delta\varphi = \varphi_{i+1} - \varphi_i \approx \pi$. The order parameter modulus is the same in all layers. The difference of $\Delta\varphi$ from 0 and π in these structures is related to the fact that

chirality of molecules forming the SmC^* and SmC_A^* induces the formation of a long-wave helix with its axis parallel to the normal to the smectic layers.

The influence of the surface on structure and phase transitions may be divided into two parts. (a) The surface breaks up the translational and rotational symmetry. Smectic layers in the free-standing films are perfectly parallel to the surfaces. The absence of layers from one side of the surface and, hence, of interactions related to these layers induces a modification of the structure near the surface. In tilted smectic liquid crystals, the interlayer interaction is anisotropic in the plane of the smectic layer, i.e., the surface influences the modulus and the phase of the order parameter. (b) The second reason for modification of surface structure is related to a change in its dynamics with respect to the bulk. "Freezing" of transverse fluctuations of surface layers leads to an increase of the order parameter [6, 7] and to a high temperature shift of the surface SmC^*–SmA transition [8]. It is commonly admitted that "freezing" of fluctuations directly influences the modulus of the smectic order parameter. However, in compounds with a structure formed by a change of the molecular tilt direction from layer to layer, interaction of the order parameter modulus with its phase may also lead to a change of the order parameter phase near the surface, i.e., to a change of the interlayer orientational structure.

In previous studies of the SmC_A^* structure and SmC_A^*–SmC^* transition in thin films, a number of

---

principal and important results have been obtained [9–12]. The absence of net transverse polarization in $\mathrm{Sm}C_A^*$ films with an even number of layers [9, 10] was one of the main proofs of anticlinic structure of antiferroelectric. It has been shown that the temperatures of bulk and surface $\mathrm{Sm}C_A^*$–$\mathrm{Sm}C^*$ transitions in films with a number of layers $N > 4$ differ [12]. However, a number of points remain unclear, in particular, the direction of the temperature shift of the $\mathrm{Sm}C_A^*$–$\mathrm{Sm}C^*$ transition in superthin films [9–12] and the influence of the number of layers on the structural states. The present investigations are the first studies of the antiferro-ferri-ferroelectric transition in superthin films with different numbers of smectic layers.

In this paper, investigations of free-standing films have been performed in a 4-(1-methylheptyloxycarbonyl)-3-fluoro-phenyl–4'[4-dodecyloxybenzoyloxy]-benzoate (MHOFPDC) antiferroelectric liquid crystal exhibiting the following phase sequence: $\mathrm{Sm}C_A^*$ (109.5°C) $\mathrm{Sm}C_{FI1}^*$ (110°C) $\mathrm{Sm}C^*$ (123°C) $\mathrm{Sm}A$. Formation of subphases between $\mathrm{Sm}C_A^*$ and $\mathrm{Sm}C^*$ is typical for antiferroelectric liquid crystals [3, 4]. In the bulk sample of MHOFPDC, the transition from the anticlinic to synclinic ordering occurs via a three-layer $\mathrm{Sm}C_{FI1}^*$ structure [13–16]. The symmetry of the $\mathrm{Sm}C_{FI1}^*$ and numerical calculations [17, 18] show that this structure is formed by change of both the phase and modulus of the order parameter from layer to layer. Investigations of phase transitions and defects in thin films were performed using polarized and depolarized reflected light microscopy. The films were prepared by spreading a small amount of the compound in the $\mathrm{Sm}C^*$ phase over a 3-mm hole in a thin glass plate. The number of smectic layers in the film was determined by the intensity of reflected light in the backscattering geometry [19]. For orientation of the tilt plane, we used a magnetic field, the direction of which could be changed with respect to the film plane [20]. Studies of phase transitions and structure of defects were performed using a digital camera.

In thin films, we observed a series of transitions with transformation of anticlinic structure to synclinic (Fig. 1). At higher temperatures, we also observed transformation of the film structure related to the bulk $\mathrm{Sm}C^*$–$\mathrm{Sm}A$ transition. It is known that these transitions in films occur near and above the bulk transition temperature [12, 21–24]. In the present paper, we discuss the results of investigations of the $\mathrm{Sm}C_A^*$–$\mathrm{Sm}C_{FI1}^*$–$\mathrm{Sm}C^*$ transitions in thin films. In a two-layer film we observed the transition at temperature about 140°C. This is not only higher than the transition to the $\mathrm{Sm}C^*$ phase, but also above the phase transition in the bulk sample from the $\mathrm{Sm}C^*$ to untilted $\mathrm{Sm}A$ phase. However, the two-layer film both below and above the
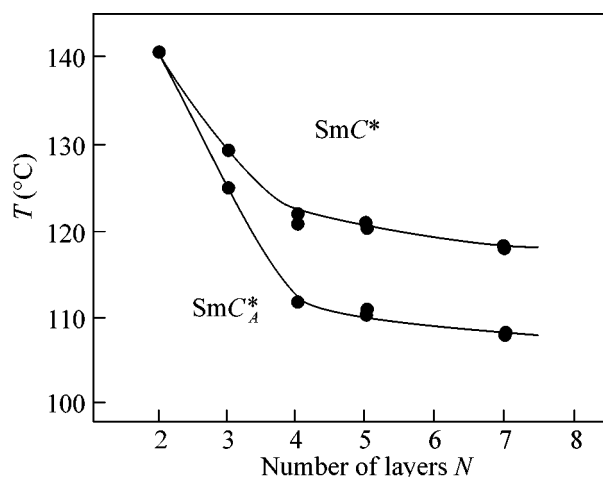

Fig. 1. Transitions in thin free-standing films of MHOFPDC. In thick films, the low-temperature branch is related to two interior transitions in films and the high-temperature branch to two surface transitions. In five- and seven-layer films, there are two pairs of transitions with close temperatures of transition. N is the number of smectic layers in the films.

transition possesses the in-plane optical anisotropy; i.e., upon heating, the transition from antiferroelectric to the tilted synclinic structure occurs with a sufficiently high temperature shift (about 30°C) with respect to the bulk sample. With increasing film thickness, the number of transitions increases (Fig. 1). In a three-layer film, we observed two transitions; in a four-layer film, three transitions; and in a five- or seven-layer film, four transitions. Transition temperatures decrease with increasing film thickness. In thick films, the four transitions are grouped into two pairs and the temperature range of the transitional region between anticlinic and synclinic structures is about 10°C (Fig. 1).

As a rule, transitions occur with thermal hysteresis. In states overheated or overcooled with respect to equilibrium transition temperature, the transition occurs in a short time interval in the whole film (less than 0.1 s). The reason for the existence of this hysteresis seems to be related to a substantial potential barrier between anticlinic and synclinic orientations. In the case of large thermal hysteresis, in some of the experiments, a smaller number of transitions than shown in Fig. 1 were observed due to their combination. For example, in a five-layer film, three or only two transitions can occur: one in the region of the low-temperature branch of transitions and one in the high-temperature region. When we are able to observe the transitions at an equilibrium temperature, they look like a sharp front moving in the plane of the film (Fig. 2a). Figure 2b shows the transition in a film upon motion of fronts formed by two germs of the new structure. Besides a boundary between two structures (*1–2* and *1–2'*), in a number of cases we could observe a breaking of **c** director orientation in the same structure in the place of meeting of
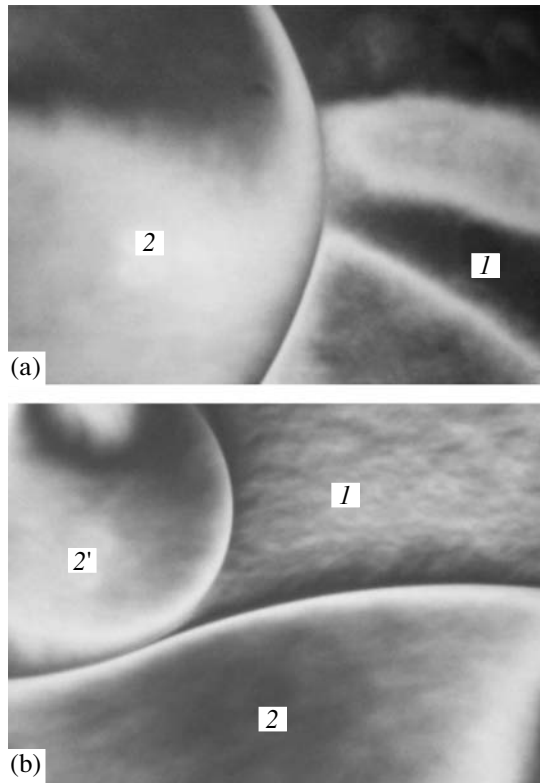
Fig. 2. Sharp front of the transition from an anticlinic (*1*) to intermediate (*2*) structure in a five-layer film (a). The meeting of two transition fronts (*2–1*) and (*2'–1*) may lead to formation of a boundary (*2–2'*) with breaking of the **c** director orientation (b) four-layer film. $T = 120.5°C$ (a), $T = 111.3°C$ (b). The horizontal size of the images is 710 μm.

Fig. 3. Structures formed during transition of the film from an anticlinic ordering (SmC_A^*) to synclinic (SmC^*). *N* is the number of smectic layers in the films.

two fronts (*2–2'*, Fig. 2b). Such sharp boundaries are not typical for liquid crystals with in-plane orientation ordering, in which the transition from one orientation to another occurs, as a rule, by continuous change of **c** director orientation. We shall return to this question later when we discuss orientational defects forming in films.

Comparing the number of observed transitions with possible orientation of molecular tilt planes in different smectic layers we may deduce practically unambiguously the structures of superthin films and, with a large degree of probability, the structures of thicker films. As was mentioned before, in a two-layer film, the transition between in-plane anisotropic structures can be only an anticlinic-synclinic transition (Fig. 3). In a three-layer film, the transition between the SmC_A^* and SmC^* occurs via an intermediate structure with anticlinic orientation of surface layers (Fig. 3). In the center of thick films, the sequence and temperature range of the phases should correspond to the bulk sample. Two low-temperature transitions in thick films should be interpreted as transitions from an anticlinic structure to a three-layer one and, then, to a synclinic state (Fig. 3). Surface transitions are shifted to the high temperature
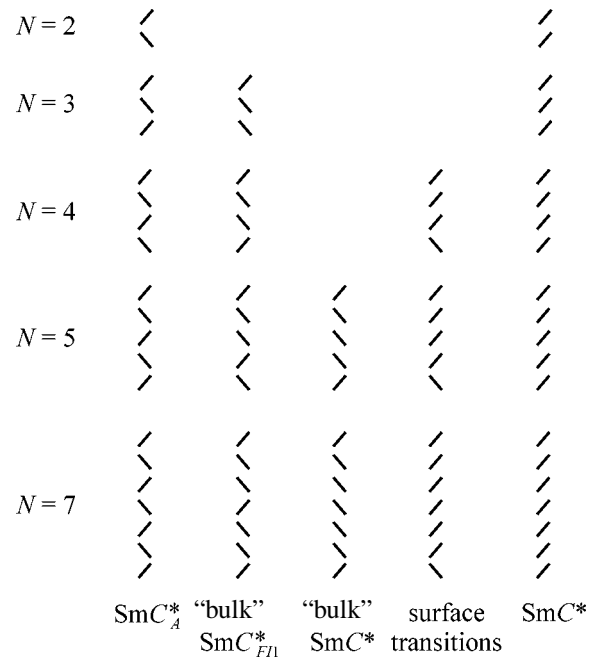
region (high temperature branch). As a rule, these transitions occur independently on the two surfaces at close temperatures.

A number of qualitative conclusions about the interlayer interactions could be drawn from the appearance of the phase diagram (Fig. 1). In a two-layer film, the high temperature shift of the transition between synclinic SmC^* and untilted Sm*A* with respect to the bulk sample is about 30°C [8, 25]. Surface ordering also leads to increase of the anticlinic–synclinic transition temperature in a two-layer film (Fig. 1). The same value of temperature shift means that the transition between tilted structures in the two-layer film occurs at the same value of molecular tilt angle as in the bulk sample. Antiferroelectric–ferroelectric transition results from competition between F_a and F_s, interactions stabilizing anticlinic and synclinic ordering in the nearest neighboring (NN) layers. These interactions alone cannot lead to formation of an intermediate structure in a three-layer film. It is necessary to form a structure with both anticlinic and synclinic orientations in a three-layer film interaction between next-nearest neighboring (NNN). Such interaction in the discrete phenomenological theory [26, 27] is the so-called frustrating interaction (F_f), stabilizing anticlinic orientation in NNN layers. In a three-layer film, the surface ordering (i) increases the region of existence of anticlinic structure due to NN interaction F_a and (ii) stabilizes the intermediate structure at higher temperatures with respect to the bulk sample through NNN interaction F_f.
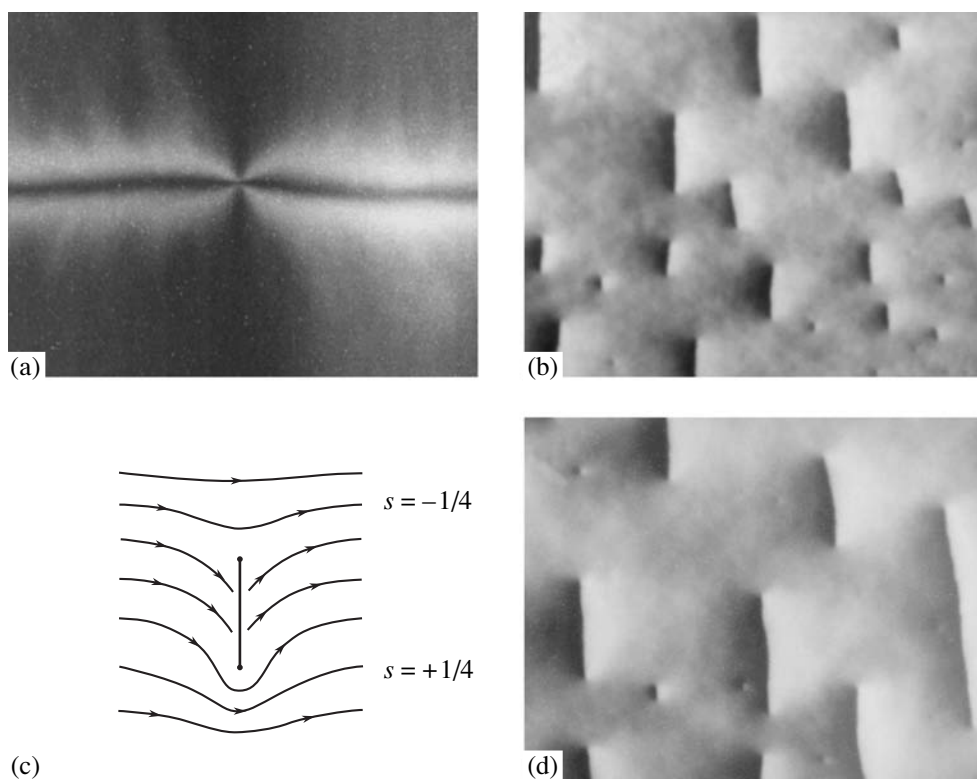
$s = -1/4$

$s = +1/4$

(a) (b) (c) (d)

Fig. 4. Linear defects in MHOFPDC films. The tilt plane is oriented by a magnetic field in a horizontal direction. (a) π-walls with continuous change of **c** director orientation. Two walls are separated by a point topological defect. The polarizers are crossed. (b) Strings with breaking of orientation of the **c** director in the center of the line defect. Strings are oriented perpendicularly to the **c** director. The polarizer and the analyzer are slightly decrossed. (c) Orientation of the **c** director near the string ending with two $|s| = 1/4$ point defects. (d) Strings attract and link by ends having point defects of opposite signs, forming longer strings. $N = 6$, $H = 2$ kG, $T = 115.2°C$. The horizontal size of the photographs is about 500 μm.

In thick films, before the transition to the SmC^*, the surface structure is anticlinic if one considers two surface layers, while it is SmC^*_{FI1}-like if we take into account three layers (Fig. 3), i.e., surface ordering makes a contribution to stabilization of the surface structure both via NN and frustrating NNN interaction. Description of the SmC^*_A–SmC^*_{FI1}–SmC^* transitions in thick films needs consideration of NNNN interaction [16, 28]. Until now, such a theoretical description of the transitions in films has not been done.

In thin films, we observed two types of linear orientation defects: walls with continuous change of **c** director orientation across the defects (Fig. 4a) and string defects with a sharp core (Fig. 4b). Strings were first found in films by J. Pang *et al.* [29] but, up to now, their internal structure and origin remain unclear. The appearance of string defects is also connected with thinning transitions [30]. We investigated strings in oriented samples and found that strings orient perpendicularly to the **c** director (Fig. 4b) and interact even at large distances. In the present case, the nucleation of defects is connected with structural transition. Figure 4c shows the distribution of the **c** director near an isolated

string obtained by depolarized light reflected microscopy. This is a so-called 1/4-string [29] with the **c** director oriented by an angle $\pm\pi/4$ to the string near its core and with a discontinuous change of orientation on the angle $\pi/2$ upon crossing the string. The **c** director orientation near the string ends corresponds to two point topological defects with strengths $s = +1/4$ and $s = -1/4$. Short strings may be considered as a topological dipole [31]. Long strings repel in the direction perpendicular to the strings due to the same direction of the bend deformation of the **c** director orientation between neighboring strings. Such strings are situated at substantial distances. With time, the average length of the strings increases (Fig. 4d). This occurs not due to elongation of isolated strings, but as a result of their head-to-tail adjoining and formation of longer strings. Strings shifted with respect to each other by a distance of the order of their length interact more like topological defects with strength $\pm1/4$. These strings are attracted to each other and adjoin by ends having topological defects of opposite signs.

Several proposals have been made concerning the structure of the core [29], in particular, that it is formed by small particles of impurities. We observed formation

of strings after a fast transition in a film and their disappearance as a result of the next transition. We may propose that the string core consists of nuclei of another structure, such as a boundary formed as a result of transitions starting in two different parts of the film (Fig. 2b). Particles of impurities trapped on this linear defect may prevent string collapse from its ends.

In summary, we have reported optical reflection measurements of a compound possessing the $\mathrm{Sm}C_A^*$, $\mathrm{Sm}C^*$ phases and the $\mathrm{Sm}C_{FI1}^*$ subphase with a small temperature interval. Our results show that the surface ordering effectively interacts with the phase of the order parameter, leading to increase of transition temperature in thin films and to formation of two branches of transitions (interior and surface transitions). In film, besides conventional walls, we observed narrow string defects with a total topological strength of zero. Their orientation in anisotropic film and collective behavior are determined by elastic deformation of the in-plane molecular ordering.

REFERENCES

1. W. H. de Jeu, B. I. Ostrovskii, and A. N. Shalaginov, Rev. Mod. Phys. **75**, 181 (2003).

2. R. B. Meyer, L. Liébert, L. Strzecki, and P. Keller, J. Phys. Lett. **36**, L69 (1975).

3. A. D. L. Chandani, E. Gorecka, Y. Ouchi, *et al.*, Jpn. J. Appl. Phys., Part 2 **28**, L1265 (1989).

4. A. Fukuda, Y. Takanishi, T. Isozaki, *et al.*, J. Mater. Chem. **4**, 997 (1994).

5. P. G. de Gennes and J. Prost, *The Physics of Liquid Crystals*, 2nd ed. (Clarendon Press, Oxford, 1993; Mir, Moscow, 1982).

6. D. Ronis and C. Rosenblatt, Phys. Rev. A **21**, 1687 (1980).

7. R. Hołist, Phys. Rev. A **44**, 3692 (1991).

8. S. Henekamp, R. A. Pelcovits, E. Fontes, *et al.*, Phys. Rev. Lett. **52**, 1017 (1984).

9. Ch. Bahr and D. Fliegner, Phys. Rev. Lett. **70**, 1842 (1993).

10. D. R. Link, J. E. Maclennan, and N. A. Clark, Phys. Rev. Lett. **77**, 2237 (1996).

11. D. R. Link, G. Natale, N. A. Clark, *et al.*, Phys. Rev. Lett. **82**, 2508 (1999).

12. C. Y. Chao, C. R. Lo, P. J. Wu, *et al.*, Phys. Rev. Lett. **86**, 4048 (2001).

13. P. Mach, R. Pindak, A.-M. Levelut, *et al.*, Phys. Rev. Lett. **81**, 1015 (1998).

14. P. Mach, R. Pindak, A.-M. Levelut, *et al.*, Phys. Rev. E **60**, 6793 (1999).

15. P. M. Johnson, D. A. Olson, S. Pankratz, *et al.*, Phys. Rev. Lett. **84**, 4870 (2000).

16. E. Gorecka, D. Pociecha, M. Čepič, *et al.*, Phys. Rev. E **65**, 061703 (2002).

17. P. V. Dolganov, V. M. Zhilin, V. E. Dmitrienko, and E. I. Kats, Pis'ma Zh. Éksp. Teor. Fiz. **76**, 579 (2002) [JETP Lett. **76**, 498 (2002)].

18. P. V. Dolganov, V. M. Zhilin, V. K. Dolganov, and E. I. Kats, Phys. Rev. E **67**, 041 716 (2003).

19. M. Born and E. Wolf, *Principles of Optics*, 6th ed. (Pergamon, Oxford, 1980; Nauka, Moscow, 1973).

20. P. V. Dolganov and B. M. Bolotin, Pis'ma Zh. Éksp. Teor. Fiz. **77**, 503 (2003) [JETP Lett. **77**, 429 (2003)].

21. Ch. Bahr and D. Fliegner, Phys. Rev. A **46**, 7657 (1992).

22. P. O. Andreeva, V. K. Dolganov, C. Gors, *et al.*, Phys. Rev. E **59**, 4143 (1999).

23. D. Schlauf, Ch. Bahr, V. K. Dolganov, and J. W. Goodby, Eur. Phys. J. B **9**, 461 (1999).

24. P. M. Johnson, D. A. Olson, S. Pankratz, *et al.*, Phys. Rev. E **62**, 8106 (2000).

25. S. M. Amador and P. S. Pershan, Phys. Rev. A **41**, 4326 (1990).

26. M. Čepič and B. Žekš, Mol. Cryst. Liq. Cryst. Sci. Technol., Sect. A **263**, 61 (1995).

27. B. Rovšek, M. Čepič, and B. Žekš, Phys. Rev. E **62**, 3758 (2000).

28. D. A. Olson, X. F. Han, A. Cady, and C. C. Huang, Phys. Rev. E **66**, 021702 (2002).

29. J. Pang, C. D. Muzny, and N. A. Clark, Phys. Rev. Lett. **69**, 2783 (1992).

30. P. Cluzeau, G. Joly, H. T. Nguyen, *et al.*, Phys. Rev. E **62**, R5899 (2000).

31. D. Pettey, T. C. Lubensky, and D. Link, Liq. Cryst. **25**, 5 (1998).

The Mesoscopic Chiral Metal–Insulator Transition[¶]

S. Kettemann[1], B. Kramer[1], and T. Ohtsuki[1, 2]

[1] *Institut für Theoretische Physik, Universität Hamburg, 20355 Hamburg, Germany*
[2] *Department of Physics, Sophia University, Chiyoda-Ku, 102-8554 Tokyo, Japan*
Received July 16, 2004

Sharp localization transitions of chiral edge states in disordered quantum wires subject to a strong magnetic field are shown to be driven by crossovers from two- to one-dimensional localization of bulk states. As a result, the two-terminal conductance is found to exhibit discontinuous transitions at zero temperature between *exactly* integer plateau values and zero, reminiscent of first-order phase transitions. We discuss the corresponding phase diagram. The spin of the electrons is shown to result in a multitude of phases when the spin degeneracy is raised by the Zeeman energy. The width of conductance plateaus is found to depend sensitively on the spin flip rate $1/\tau_s$. © 2004 MAIK "Nauka/Interperiodica".

PACS numbers: 72.10.Fk; 72.15.Rn; 73.20.Fz

The high precision of the quantization of the Hall conductance of a two-dimensional (2D) electron system (2DES) in a strong magnetic field [1] is known to be due to the binding of electrons to localized states in the bulk of the 2DES. Thereby, a change of electron density does not change the Hall conductance [2–4]. The localization length in tails of Landau bands is very small, on the order of the cyclotron length $l_{\mathrm{cyc}} = v_F/\omega_B = \sqrt{2n+1}\, l_B$. It increases toward the centers of the Landau bands, $E_{n0} = \hbar\omega_B(n + 1/2)$ ($n = 0, 1, 2, \ldots$), with $\omega_B = eB/m^*$ is the cyclotron frequency (e is the elementary charge, m^* is the effective mass), v_F is the Fermi velocity, and $l_B^2 = \hbar/eB$ defines the magnetic length. In an *infinite* 2DES in a perpendicular magnetic field, the localization length at energy E diverges as $\xi \sim |E - E_{n0}|^{-\nu}$, reminiscent of second-order phase transitions. The critical exponent ν is found numerically for the lowest two Landau bands, $n = 0, 1$, to be $\nu = 2.33 \pm 0.04$ for spin-split Landau levels [5, 6]. Analytical [7] and experimental studies [8] are consistent with this value. In a *finite* 2DES, a region of extended states should exist in the centers of disorder of broadened Landau bands. These states extend beyond the system size L. The width of these regions is given by $\Delta E = (l_{\mathrm{cyc}}/L)^{1/\nu}\Gamma$, where $\Gamma = \hbar(2\omega_B/\pi\tau)^{1/2}$ is the bandwidth, with elastic scattering time τ.

In quantum Hall bars of finite width, there exist, in addition, edge states with energies raised by the confinement potential above the energies of the centers of bulk Landau bands, E_{n0} [4]. Previously, there has been considerable interest in the study of mesoscopically narrow quantum Hall bars [9], with emphasis on conductance fluctuations [10, 11], edge state mixing [12–

15], breakdown of the quantum Hall effect [16], and quenching of the Hall effect due to classical commensurability effects [17]. It is known that, in the presence of white noise disorder, the edge states mix with the bulk states when the Fermi energy is moved into the center of a Landau band. It has been suggested that this might result in localization of edge states [14, 15]. In this paper, we show that this is indeed the case. In particular, at zero temperature, the two-terminal conductance of a quantum wire in a magnetic field exhibit, for uncorrelated disorder and hard wall confinement, discontinuous transitions between integer plateau values and zero (Fig. 1).

Localization length ξ in a 2DES with broken time reversal symmetry is expected from scaling theory [19–22] and numerical scaling studies [23, 24] to be

$$\xi_{2D} = l_0 e^{\pi^2 g^2}, \tag{1}$$

depending exponentially on g, the 2D conductance parameter per spin channel. l_0 is the short distance cutoff, which is the elastic mean free path $l = 2g(B = 0)/k_F$ (k_F is the Fermi wavenumber) at moderate magnetic fields, $b \equiv \omega_B\tau < 1$. For stronger magnetic fields, $b > 1$, l_0 crosses over to the cyclotron length l_{cyc}. g exhibits Shubnikov–de Haas oscillations as a function of magnetic field for $b > 1$. Maxima occur when the Fermi energy is in the center of Landau bands. Thus, the localization length increases strongly from band tails to band centers, even when the wire width L_y is too narrow to allow delocalization of bulk states. For uncorrelated impurities, within a self-consistent Born approximation [25], the maxima are given by $g(E = E_{n0}) = (2n + 1)/\pi = g_n$. Thus, $\xi_{2D}(E_{n0}) = l_{\mathrm{cyc}}\exp(\pi^2 g_n^2)$ are macroscopically large in centers of higher Landau bands, $n > 1$ [6, 26]. However, when the width of the system L_y is smaller

---

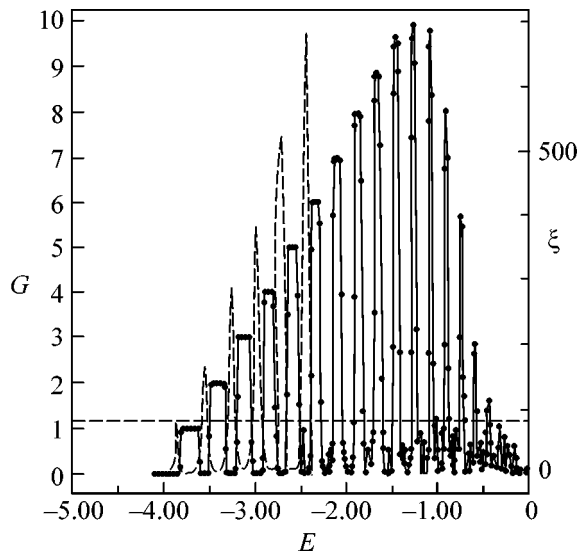[¶] This article was submitted by the authors in English.

Fig. 1. Solid curve, left axis: two-terminal conductance of a wire (width $L_y = 80a$, length $L = 5000a$, hard wall confinement) in units of $G_0 = e^2/h$ as a function of energy E in units of t (hopping amplitude in the tight binding model). Disorder strength, $W = 0.8t$. There are $x = 0.025$ magnetic flux quanta through an elementary cell a^2. Dashed curve, right axis: bulk localization length ξ in units of a as function of E, from transfer matrix method for wire of identical properties but periodic boundary conditions and $L_{\max} = 100000a$. Straight dashed line: $L_y = 80a$.
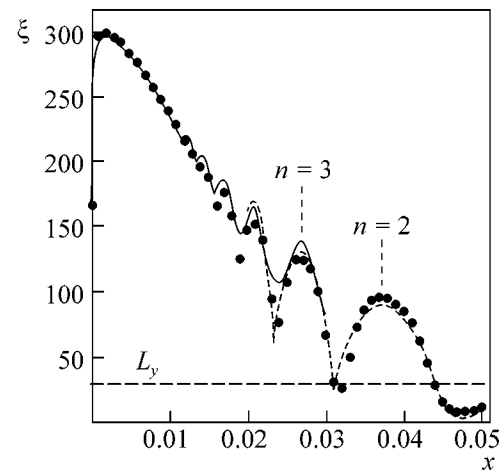

Fig. 2. The localization length, ξ, as obtained by inserting $g(B)$ into a second-order Born approximation in Eq. (3), including a summation over all Landau levels (full line). Broken line: ξ, with $g(B)$ in SCBA, neglecting overlap between Landau bands (Eq. (4)). The result of transfer matrix calculations is plotted (dot size: numerical error $\approx 1\%$) for periodic boundary conditions [31] as a function of magnetic flux through unit cell $x = a^2/2\pi l_B^2$. The dimensionless conductance parameter per spin channel is $g(B = 0) = 5.1$. At weak magnetic fields, doubling of ξ due to breaking of time reversal symmetry is seen, in good agreement with the analytical crossover formula (full line) [30, 32]. Horizontal dashed line: $L_y = 30a$.

than ξ_{2D}, localization is expected to behave in a quasi-1D fashion. In other words, electrons in centers of Landau bands can diffuse between the edges of the system but are localized parallel to the edges if $L_y < \xi_{2D}$. The quasi-1D localization length is known to depend only linearly on g. In a magnetic field, when time reversal symmetry is broken, it is [27–29]

$$\xi_{1D} = 2g(B)L_y. \qquad (2)$$

There is a crossover from 2D to 1D localization as the Fermi energy moves from tails to centers of Landau bands. Performing renormalization of the wire conductance, for the localization length, one obtains [30]

$$\xi^2 = 4L_y^2 g^2 - \frac{2L_y^2}{\pi^2}\ln\left[\frac{1 + (L_y/l_0)^2}{1 + (L_y/\xi)^2}\right]. \qquad (3)$$

Its solution shows a crossover between quasi-1D and 2D behavior (Eqs. (2) and (1), respectively).

The conductance per spin channel, $g(b) = \sigma_{xx}(B)/\sigma_0$, is given by the Drude formula $g(b) = g_0/(l + b^2)$ ($g_0 = E\tau/\hbar$, $b = \omega_B\tau$) for weak magnetic field, $b < 1$. For $b > 1$, when the cyclotron length l_{cyc} is smaller than the mean

free path l, disregarding the overlap between Landau bands, g is obtained in SCBA [25],

$$g(B) = \frac{1}{\pi}(2n + 1)\left(1 - \frac{(E_F - E_n)^2}{\Gamma^2}\right), \qquad (4)$$

for $|E - E_n| < \Gamma$. One obtains the localization length for $b > I$ and $|\epsilon/b - n - 1/2| < 1$ by inserting g (Eq. (4)) into Eq. (3). It oscillates between maximal values in centers of Landau bands and minimal values in band tails (Fig. 2). For $n > 1$, in band centers, one finds

$$\xi_n = \frac{2}{\pi}(2n + 1)L_y\left[1 - \frac{\ln\sqrt{1 + (l_y/l_{\text{cyc}})^2}}{(n + 1/2)^2}\right]^{1/2}. \qquad (5)$$

In the center of the lowest Landau band ($n = 0$), Eq. (2) gives a value $\xi_0(B) \approx (2/\pi)L_y$ smaller than L_y. There, the localization is 2D and the topological term [34] is effective, leading to criticality and diverging localization lengths. In a wire of finite width L_y, localization length ξ saturates to the critical value $\xi_{\text{crit}} \approx 1.2L_y$ [5, 6] larger than L_y. Comparison with ξ_n (Eq. (5)) shows that the noncritical quasi-1D localization length exceeds ξ_{crit} in all but the lowest Landau bands.

If all states in centers of higher Landau bands are localized along the wire, the question arises if there exist extended states in the quantum Hall wire at all.

Consider an annulus with a circumference larger than the localization length in the center of a Landau band. When a magnetic flux pierces the annulus, localized states are unaffected. Guiding centers of states that extend around the annulus do shift in position and energy, however [4]. In a confined wire, there exist chiral edge states that extend around the annulus. A magnetic flux change moves these states down and up inner and outer edges, respectively. As was shown above, in the middle of the Landau band, the electrons can diffuse freely from edge to edge but are localized along the annulus with $\xi > L_y$. As a consequence, when adiabatically changing the magnetic flux, an "edge state" has to move from the inner to the outer edge, since it cannot enter the band of localized states. This fact has been interpreted as proof for the existence of an extended bulk state extending around the annulus and between edges at the energy E_m, with $\xi(E_m) = L_y$ [4]. In the following, we show that, instead, a transition from extended chiral edge states to localized states occurs at these energies, E_m.

Using the transfer matrix method [24], we have calculated the localization length as function of energy E in a tight binding model of a disordered quantum wire in a perpendicular magnetic field with periodic boundary conditions (Fig. 1, dashed curve, right axis). Indeed, its maxima are seen to increase linearly with energy E, in agreement with Eq. (5). The transfer matrix result for the two-terminal conductance G [35] is shown in Fig. 1 (solid curve, left axis) for a wire of identical properties, but hard wall boundary conditions and finite length L.

We verify that the condition $\xi(E_{m,p}) = L_y$ yields the energies $E_{m,p}$, $p = \pm$, at which m edge states mix and transitions from the quasi-1D chiral metal to an insulator occur, as signaled by sharp jumps of G in Fig. 1. Here, $m = n$ when this energy is above the bulk energy of the nth Landau band, $p = +$, and $m = n - 1$ when it is below it, $p = -$. For $\xi < L_y$, backscattering between edges is exponentially suppressed and the localization length of edge states increases exponentially as $\xi_{edge} = \xi \exp(L_y/\xi)$. These results are summarized in the phase diagram (Fig. 3a), where the value of G, in units of e^2/h, is given as a function of wire width L_y and energy E in units of $\hbar\omega_B$. We find that $G = m$, where m is the number of extended edge states. When $L_y \le l_{cyc} \propto \sqrt{2n+1}$, all edge states are localized and all conductance plateaus collapse, $G = 0$, as seen in Fig. 1, close to the middle of the band, and $E = 0$.

Taking into account the spin, the Zeeman splitting $E_n^+ = E_n^- = g_z\mu_B B$ lifts the spin degeneracy, where g_z is the material-dependent Zeeman g-factor and μ_B is the Bohr's magneton. Without spin flip scattering, edge states of different spins are not mixed. The phase diagram (Fig. 3b) is, then, a superposition of two phase diagrams (Fig. 3a) for each spin. There are phases where the conductance is equal to the total number of
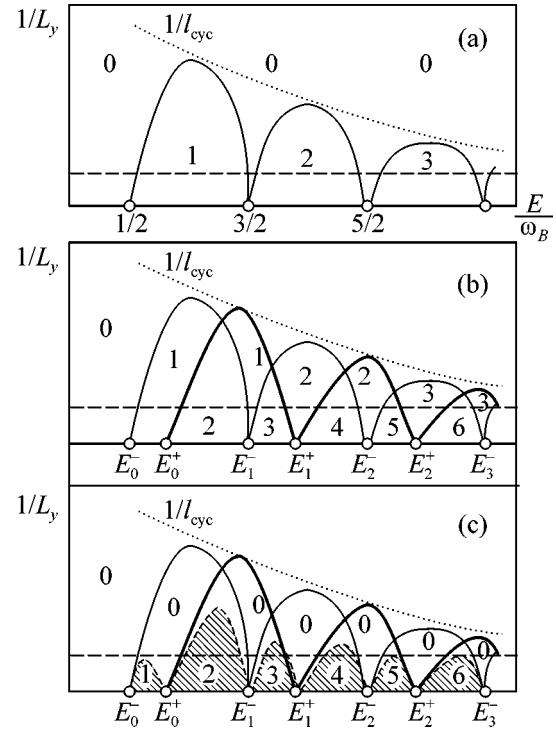

Fig. 3. Schematic phase diagram of a quantum Hall wire for $L \gg L_y$. The full lines indicate jumps between integer plateau values of conductance G, in units of e^2/h, as denoted by integers: (a) spinless electrons, (b) electrons with spin and Zeeman-splitting $(E_n^+ - E_n^-)/\hbar\omega_B = g_Z/2$ without spin flip, and (c) with a strong spin flip rate. Dotted line: inverse cyclotron length, $1/l_{cyc}$. For a particular value of inverse width $1/L_y$ (dashed line), a sequence of conductance plateaus similar to Fig. 1 is obtained. In the limit of $1/L_y \longrightarrow 0$, there are delocalization critical points of bulk states (circles).

edge channels, $G = m^+ + m^-$, when the bulk localization length of electrons ξ^σ does not exceed the wire width, $\xi^\sigma < L_y$, for either spin $\sigma = \pm$. When $\xi^\sigma > L_y$ for one spin σ only, the conductance is carried by the number of edge states with opposite spin, $G = m^{-\sigma}$ only. If $\xi^\sigma < L_y$ for both $\sigma = \pm$, the conductance vanishes, $G = 0$. With strong spin flip scattering, all edge states mix with bulk states for $\xi^\sigma > L_y$, yielding $G = 0$. There are conductance plateaus equal to the total number of edge states, $G = m^+ + m^-$, only if $\xi^\sigma < L_y$ is fulfilled for both spins, $\sigma = \pm$ (Fig. 3c). Thus, both the sequence and width of conductance plateaus are sensitive measures of the spin flip scattering rate $1/\tau_s$, due to electron–electron interaction, spin–orbit interaction, or scattering from nuclear spins [36]. Furthermore, the enhancement of the g_Z-factor above its bulk value due to the exchange interaction depends on the Fermi energy [38]. Accordingly, the width of the conductance plateaus changes with energy. In a real sample, there exists a slowly varying potential disorder, which can stabilize edge states against mixing

with bulk states [14]. When the confinement potential is varying slowly on the magnetic length scale l_B, the energies $E_{m,p}$ are expected to split into m energies, at which edge states mix one by one with bulk states, accompanied by steps of heights 1 in conductance G. Both potentials can be effectively modified by the Coulomb interaction as obtained by self-consistent solution of the Poisson equation.

In the presence of long-range interactions, interacting edge states form a correlated Luttinger liquid. Renormalization due to edge plasmon excitations enhances the interedge scattering amplitude [39]. This results in a decrease of the localization length of the edge states. Accordingly, the width of the plateaus of lower Landau bands is expected to be reduced due to the Luttinger liquid correlations. Similarly, in the fractional quantum Hall regime, where the edge state excitations are strongly correlated even without long-range interactions [39], a reduction of the localization length of edge states is expected as function of the filling factor v.

In 3D layered systems in a perpendicular magnetic field, surface states form 2D chiral metals in plateau regions where bulk states are localized [18]. There are transitions between these 2D chiral metals and insulating states in long quasi-1D wires of layered electron systems.

We conclude that, in quantum Hall bars of finite width $L_y \ll \xi_n$ at low temperatures, quantum phase transitions occur between extended chiral edge states and a quasi-1D insulator. These are driven by a crossover from 2D to 1D localization of bulk states. These metal–insulator transitions *resemble* first-order phase transitions in the sense that the localization length abruptly jumps between exponentially large and finite values. In the thermodynamic limit, *fixing the aspect ratio $c = L/L_y$, when sending $L \longrightarrow \infty$ and, then, $c \longrightarrow \infty$, the two-terminal conductance jumps between exactly integer values and zero*. The transitions occur at energies where the localization length of bulk states is equal to the geometrical wire width. Then, m edge states mix and electrons are free to diffuse between the wire boundaries but become Andersen localized along the wire. At a finite temperature, this phenomenon can be observed when the phase coherence length exceeds the quasi-1D localization length in centers of Landau bands, $L_\varphi > \xi_n$. It may accordingly be called the *mesoscopic chiral metal–insulator transition*. In Hall bars of large aspect ratios at low temperatures, one should observe transitions of the two-terminal resistance from integer quantized plateaus, $R_n = h/ne^2$, to a Mott variable-range hopping regime of exponentially diverging resistance. Such experiments would yield new information about edge states in quantum Hall bars. At a higher temperature, when $L_\varphi < \xi_n$, the conventional form of the integer quantum Hall effect is recovered [1].

REFERENCES

1. K. von Klitzing, G. Dorda, and M. Pepper, Phys. Rev. Lett. **45**, 494 (1980).
2. R. B. Laughlin, Phys. Rev. B **23**, 5632 (1981).
3. T. Ando and H. Aoki, Solid State Commun. **38**, 1079 (1981); R. B. Laughlin, Phys. Rev. Lett. **50**, 1395 (1983).
4. B. I. Halperin, Phys. Rev. B **25**, 2185 (1982).
5. J. T. Chalker and G. J. Daniell, Phys. Rev. Lett. **61**, 593 (1988); B. Huckestein and B. Kramer, Phys. Rev. Lett. **64**, 1437 (1990).
6. B. Huckestein, Rev. Mod. Phys. **67**, 357 (1995).
7. A. G. Galstyan and M. E. Raikh, Phys. Rev. B **56**, 1422 (1997); D. P. Arovas, M. Janssen, and B. Shapiro, Phys. Rev. B **56**, 4751 (1997).
8. H. P. Wei *et al.*, Phys. Rev. Lett. **61**, 1294 (1988); S. Koch *et al.*, Phys. Rev. Lett. **67**, 883 (1991); L. W. Engel *et al.*, Phys. Rev. Lett. **71**, 2638 (1993); M. Furlan, Phys. Rev. B **57**, 14818 (1998); F. Hohls *et al.*, Phys. Rev. Lett. **88**, 036802 (2002).
9. R. J. Haug and K. von Klitzing, Europhys. Lett. **10**, 489 (1989).
10. G. Timp *et al.*, Phys. Rev. Lett. **59**, 732 (1987); Phys. Rev. Lett. **63**, 2268 (1989).
11. T. Ando, Phys. Rev. B **49**, 4679 (1994).
12. B. J. van Wees, L. P. Kouwenhoven, E. M. M. Willems, *et al.*, Phys. Rev. B **43**, 12431 (1991).
13. B. I. Shklovskii, Pis'ma Zh. Éksp. Teor. Fiz. **36**, 43 (1982) [JETP Lett. **36**, 51 (1982)]; A. V. Khaetskii and B. I. Shklovskii, Zh. Éksp. Teor. Fiz. **85**, 721 (1983) [Sov. Phys. JETP **58**, 421 (1983)]; M. E. Raikh and T. V. Shahbazyan, Phys. Rev. B **51**, 9682 (1995).
14. T. Ohtsuki and Y. Ono, Solid State Commun. **65**, 403 (1988); Solid State Commun. **68**, 787 (1988); Y. Ono, T. Ohtsuki, and B. Kramer, J. Phys. Soc. Jpn. **58**, 1705 (1989); T. Ohtsuki and Y. Ono, J. Phys. Soc. Jpn. **58**, 956 (1989); T. Ando, Phys. Rev. B **42**, 5626 (1990).
15. R. G. Mani and K. von Klitzing, Phys. Rev. B **46**, 9877 (1992); R. G. Mani, K. von Klitzing, and K. Ploog, Phys. Rev. B **51**, 2584 (1995).
16. P. G. N. de Vegvar, A. M. Chang, G. Timp, *et al.*, Phys. Rev. B **36**, 9366 (1987).
17. M. L. Roukes, A. Scherer, S. J. Allen, *et al.*, Phys. Rev. Lett. **59**, 3011 (1987).
18. J. T. Chalker and A. Dohmen, Phys. Rev. Lett. **75**, 4496 (1995).
19. E. Abrahams, P. W. Anderson, D. C. Licciardello, *et al.*, Phys. Rev. Lett. **42**, 673 (1979).
20. F. Wegner, Z. Phys. B **36**, 1209 (1979); Nucl. Phys. B **316**, 663 (1989).
21. S. Hikami, Prog. Theor. Phys. **64**, 1466 (1980).

22. K. B. Efetov, A. I. Larkin, and D. E. Khmel'nitskii, Zh. Éksp. Teor. Fiz. **79**, 1120 (1980) [Sov. Phys. JETP **52**, 568 (1980)].

23. A. MacKinnon and B. Kramer, Phys. Rev. Lett. **47**, 1546 (1981); Z. Phys. B **53**, 1 (1983).

24. B. Kramer and A. MacKinnon, Rep. Prog. Phys. **56**, 1469 (1993).

25. T. Ando and Y. Uemura, J. Phys. Soc. Jpn. **36**, 959 (1974); T. Ando, J. Phys. Soc. Jpn. **36**, 1521 (1974); J. Phys. Soc. Jpn. **37**, 622 (1974).

26. B. Huckestein, Phys. Rev. Lett. **84**, 3141 (2000).

27. K. B. Efetov, *Supersymmetry in Disorder and Chaos* (Cambridge Univ. Press, Cambridge, 1997).

28. K. B. Efetov and A. I. Larkin, Zh. Éksp. Teor. Fiz. **85**, 764 (1983) [Sov. Phys. JETP **58**, 444 (1983)].

29. O. N. Dorokhov, Pis'ma Zh. Éksp. Teor. Fiz. **36**, 259 (1982) [JETP Lett. **36**, 318 (1982)]; Zh. Éksp. Teor. Fiz. **85**, 1040 (1983) [Sov. Phys. JETP **58**, 606 (1983)]; Solid State Commun. **51**, 381 (1984).

30. S. Kettemann, J. Phys. Soc. Jpn. (Suppl. A) **72**, 197 (2003); Phys. Rev. B **69**, 035339 (2004).

31. V. Kalmeyer, D. Wei, D. P. Arovas, and S.-C. Zhang, Phys. Rev. B **48**, 11095 (1993).

32. S. Kettemann, Phys. Rev. B **62**, R13282 (2000); S. Kettemann and R. Mazzarello, Phys. Rev. B **65**, 085318 (2002).

33. R. M. Corless *et al.*, Adv. Comput. Math. **5**, 329 (1996).

34. A. M. M. Pruisken, in *The Quantum Hall Effect*, Ed. by R. E. Prange and S. M. Girvin (Springer, New York, 1990).

35. J. B. Pendry, A. MacKinnon, and P. J. Roberts, Proc. R. Soc. London, Ser. A **437**, 67 (1992).

36. S. Komiyama, O. Astafiev, and T. Machida, Physica E (Amsterdam) **20**, 43 (2003).

37. K. Takashima *et al.*, Physica E (Amsterdam) **20**, 160 (2003).

38. F. F. Fang and P. J. Stiles, Phys. Rev. **174**, 823 (1968).

39. C. L. Kane and M. P. A. Fisher, in *Perspectives in Quantum Hall Effects*, Ed. by S. Das Sarma and A. Pinczuk (Wiley, New York, 1997).